Time-Domain Simulation of Wave-Induced Ship Motions by a Rankine Panel Method

by

©Junshi Wang

A Thesis submitted to the School of Graduate Studies in partial fulfillment of the requirements for the degree of

Master of Engineering

Faculty of Engineering and Applied Science

Memorial University of Newfoundland

May 2016

St. John's Newfoundland

Abstract

In this thesis, a numerical program has been developed to simulate the wave-induced ship motions in the time domain. Wave-body interactions have been studied for various ships and floating bodies through forced motion and free motion simulations in a wide range of wave frequencies.

A three-dimensional Rankine panel method is applied to solve the boundary value problem for the wave-body interactions. The velocity potentials and normal velocities on the boundaries are obtained in the time domain by solving the mixed boundary integral equations in relation to the source and dipole distributions. The hydrodynamic forces are calculated by the integration of the instantaneous hydrodynamic pressures over the body surface. The equations of ship motion are solved simultaneously with the boundary value problem for each time step.

The wave elevation is computed by applying the linear free surface conditions. A numerical damping zone is adopted to absorb the outgoing waves in order to satisfy the radiation condition for the truncated free surface. A numerical filter is applied on the free surface for the smoothing of the wave elevation.

Good convergence has been reached for both forced motion simulations and free motion simulations. The computed added-mass and damping coefficients, wave exciting forces, and motion responses for ships and floating bodies are in good agreement with the numerical results from other programs and experimental data.

Acknowledgements

I am grateful to everyone who has contributed to this work and helped me during my studies.

First of all, I would like to express my deepest appreciation and give thanks to my supervisor, Dr. Heather Peng, for her invaluable academic guidance, patience and kindness throughout my studies. With her clear guidance and warm encouragement I have developed a great interest in and passion for marine hydrodynamics. Her suggestions were always insightful and my discussions with her were always inspiring. I would like to express my deep gratitude and respect to Dr. Wei Qiu for his advice and support of this work. He has provided an example of professional excellence that I can always follow. I would also like to thank Dr. Wei Qiu for the trust he showed by giving me the opportunity to work with him on several research projects within the Advanced Marine Hydrodynamic Lab (AMHL), which has strengthened my academic background and research expertise. He is my mentor in marine hydrodynamics and I treasure the time we have worked together.

I would like to thank Dr. Shaoyu Ni for his interest in and useful comments on this work. My appreciation is extended to my colleagues, Douglas Smith, Peng Wen, Quan Zhou, Ming Liu, Jie Dai, Wei Meng. My discussions with them were very helpful for the completion of this work. I would also like to thank the others in AMHL for making my time at Memorial University joyful and productive. My colleague, Md.

Shahriar Nizam deserves my special thanks for his help on the geometry generation of this work.

I would like to express my appreciation to the NSERC CREATE Training Program for the financial support during my studies.

Last, I would like to express my profound gratitude to my parents for their love, understanding, and support throughout my studies. Talking with them has always helped me gain great confidence needed to overcome difficulties in study and life.

Table of Contents

List of Tables

List of Figures

Nomenclature

a	Radius of hemisphere and truncated cylinder
A_I	Amplitude of incident monochromatic waves
b_j	One-dimensional basis function
B_j	Two-dimensional basis function
$B(x)$	Full breadth of waterplane at x
c_F	Strength of the filter
C_{jk}, $\boldsymbol{C}$	Restoring coefficient matrix
F_j, $\boldsymbol{F}$	Hydrodynamic force acting on the ship body
g	Gravity of Earth
$G(P;Q)$	Rankine source potential
$\overline{GM}_t$	Transverse metacentric height
h	Water depth
H	Incident wave height
$\vec{i}, \vec{j}, \vec{k}$	Unit vectors in $\vec{x}$
$\vec{i}_0, \vec{j}_0, \vec{k}_0$	Unit vectors in $\vec{x}_0$
I_{44}, I_{55}, I_{66}	Moment of inertia around the x_s, y_s, and z_s axis, respectively
K	Wavenumber
L	Damping zone size
m	Mass of ship

$\vec{m}$	m-terms
M_{jk}, $\boldsymbol{M}$	Inertia matrix
$\vec{n}$	Normal vector on a surface point
N	Total number of panels
p	Pressure field in the fluid domain
p_a	Atmosphere pressure
p^H	Total hydrodynamic pressure on the ship body
p^I	Pressure on the ship body induced by the incident waves
p^R	Pressure on the ship body induced by the radiation wave components
p^D	Pressure on the ship body induced bu the diffraction wave components
P	Field point in fluid domain
Q	Source point on the domain boundaries
$\vec{r}$	Position vector of a point on the ship body surface in $\vec{x}_s$
r_{PQ}	Distance between P and Q
r^D	Radius of points in the damping zone
r_0^D	Radius where the damping zone starts
R_{max}	Computational domain size
S	The collection of boundary surfaces
S_B	Submerged body surface
S_{Bot}	Bottom surface of the computational domain
S_F	Truncated free surface of the computational domain
U	Advancing speed of ship
$V_{x_0}, V_{y_0}, V_{z_0}$	Velocity components in the fluid domain
$\vec{V}$	Velocity field with respect to $\vec{x}_0$

$\vec{x}(x, y, z)$	Steady advancing Cartesian coordinate system
$\vec{x}_0(x_0, y_0, z_0)$	Cartesian coordinate system fixed in space
$\vec{x}_s(x_s, y_s, z_s)$	Ship-fixed Cartesian coordinate system
$\vec{x}_P$	Position vector of P in $\vec{x}$
$\vec{x}_Q$	Position vector of Q in $\vec{x}$
$(\hat{x}, \hat{y})$	Local coordinate system
$(x_s^G, 0, z_s^G)$	Coordinates of the center of gravity of ship in $\vec{x}_s$
$\vec{\delta}$	Displacement of the ship about its equilibrium position in $\vec{x}$
$\Delta\hat{x}$	Size of panel in $(\hat{x}, \hat{y})$
Δt	Time step length
∇	Displacement of ship
ν	Damping strength
ν_0	Damping strength constant
ϕ	Velocity potential with respect to $\vec{x}$
ϕ^B	Double body basis flow velocity potential
ϕ^d	Disturbed wave velocity potential in $\vec{x}$
ϕ^D	Diffraction wave velocity potential in $\vec{x}$
ϕ^I	Incident wave velocity potential in $\vec{x}$
ϕ^k	Velocity potential for the k-th problem in $\vec{x}$
ϕ^R	Radiation wave velocity potential in $\vec{x}$
Φ	Total velocity potential with respect to $\vec{x}_0$
ψ	global unknowns on the panel
ψ_j	Spline coefficients
ρ	Density of fluid
ξ_0	Amplitude of forced motion
ξ_k	Vector of ship displacement in $\vec{x}$

$\vec{\xi}_R$	Rotational displacement of $\vec{x}_s$ with respect to $\vec{x}$
$\vec{\xi}_T$	Translational displacement of $\vec{x}_s$ with respect to $\vec{x}$
ζ	Wave elevation in $\vec{x}$
ζ_0	Wave elevation in $\vec{x}_0$
ζ^d	Disturbed wave elevation in $\vec{x}$
ζ^D	Diffraction wave elevation in $\vec{x}$
ζ^I	Incident wave elevation in $\vec{x}$
ζ^k	Wave elevation for the k-th problem in $\vec{x}$
ζ^R	Radiation wave elevation in $\vec{x}$

Chapter 1

Introduction

1.1 Background

It is important to predict the wave-induced motions and hydrodynamic loads on ships and floating structures to provide guidance for the design. Compared with approaches using semi-empirical rules or model test, computational hydrodynamics has the advantages of greater accuracy and less cost, for which it has become a powerful numerical tool for designers in naval architecture and ocean engineering to evaluate the seakeeping performance of ships and floating structures.

In marine hydrodynamics, the physical problem of a floating body in waves can be mathematically described as the boundary value problem with the assumption of potential flow, in which the fluid domain is governed by Laplace's equation with boundary conditions enforced on the free surface, body surface, bottom, and far field. The boundary value problem can be solved numerically by solving the corresponding boundary integral equations derived from Green's theorem.

1.1.1 Early Approaches

Early studies on ship motions from hydrodynamic aspects began in the late 19th century with the works of Froude (1861) and Krylov (1896), in which only mass, restoring forces and the Froude-Krylov force were considered in attempting to solve the equation of motion. In their work, the disturbance of the wave flow due to the presence of the ship was not considered. The thin ship theory developed by Michell (1898) first accounted for the hydrodynamic effects to solve for the steady wave resistance problem. Peters and Stoker (1957) extended this theory to compute unsteady ship motions followed by improvements by Newman (1960). Lewis (1929) also included the hydrodynamic effects by deriving a strip theory for slender ships at higher wave frequencies, which was further developed by Korvin-Kroukovsky and Jacobs (1957) to compute the motions for realistic ships and by Ogilvie and Tuck (1969) to include the effects of forward speed on the solutions at small Froude number. The slender body theory was adopted to study ship motions at lower wave frequencies in the work of Ursell (1962), Newman and Tuck (1964), and Maruo (1970). A unified theory was then developed by Newman (1978) and Sclavounos (1985) to combine the slender body theory and strip theory.

These early approaches were limited to solving two-dimensional boundary value problems at each cross section and were only valid for simple and slender hull forms at low speed. The three-dimensional boundary value problem needs to be solved for wider ranges of frequency and speed and general form ship hulls.

1.1.2 Panel Method

Originated from the work of Hess and Smith (1967), the panel method has become a popular approach for solving the three-dimensional flows around the ship in both fre-

quency domain and time domain due to its accurate prediction of hydrodynamic pressure on the hull surface and flexibility in the computations for general body shapes. In the panel method, the body surface was discretized into panels with the body boundary conditions enforced at the center of each panel. The source strengths were distributed over each panel as unknowns which were solved numerically from the boundary integral equations.

Two major approaches have been widely used to solve the free surface flows around the ship in terms of the type of singularity for the boundary integral equation. The first one employs the free surface Green function as the singularity to distribute on the body surface, which satisfies the free surface conditions and far field conditions by itself. Three-dimensional problems have been solved by many researchers using the free surface Green function. For zero forward speed, commercial programs have been developed to solve the hydrodynamic forces and wave-induced motions by Taylor and Jefferys (1986), Korsmeyer et al. (1988), and Newman and Sclavounos (1988). Computations with forward speed have been carried out by Chang (1977), Inglis and Price (1981), and Guevel and Bougis (1982) using the zero-speed Green function with corrections to include the effect of forward speed. The forward-speed Green function has been computed by Hoff (1990), Iwashita and Ohkusu (1992), Chen and Noblesse (1998), and Chen et al. (2001). Recently, Peng and Qiu (2014) investigated the effects of zero/forward-speed Green functions on the solutions of ship motion for two Wigley hulls with the panel-free method in the frequency domain.

Instead of using the free surface Green function as the singularity, the other major approach uses the Rankine source as the singularity to distribute on both the body boundary and truncated free surface around the body to solve the boundary value problem for seakeeping analysis. In this approach, both body surface and truncated free surface are discretized into panels over which the source and dipole strengths are

distributed as unknowns. The collocation points of the boundary integral equations are coincident with the centroids of the panel where the body boundary conditions and free surface boundary conditions are satisfied. The unknowns are obtained by solving a system of linear equations derived from the boundary integral equations. Since the free surface is truncated, special numerical treatment has to be adopted to satisfy the radiation condition in the far field for the free surface. This approach is also referred to as the Rankine panel method. Significant work has been done by Nakos (1990) in the frequency domain, and Kring (1994), Huang (1997), and Kim (1999) in the time domain and so forth. The development of the Rankine panel method will be discussed in detail in the following section.

1.1.3 Time-Domain Simulation

The time-domain approach has been used in the work of Finkelstein (1957), Stoker (1957), and Wehausen and Laitone (1960) to obtain direct solutions of the wave flow. Cummins (1962) studied unsteady ship motions using the impulse response function to take into account the "memory effect" by convolution integrals over the previous time steps. Further studies have been carried out by Ogilvie (1964) and Wehausen (1967).

Since the computation of forward speed Green function is easier and faster in the time domain than it is in the frequency domain, time-domain simulations became popular and have been carried out by many researchers to solve three-dimensional ship motions with advance speed. Significant work has been done by Liapis (1986), Beck and Liapis (1987), King (1987), King et al. (1988), Beck and King (1989), Korsmeyer (1991), and Bingham (1994) based on Neunman-Kelvin linearization.

The linear problem can be solved using the frequency-domain approach because it can be described as a linear system with a body boundary condition enforced on the

mean position of the exact body surface and the application of linearized free surface boundary conditions. However, the linear system is no longer valid when nonlinearity is introduced by, for example, the evaluation of nonlinear Froude-Krylov force, the use of an instantaneous wetted body surface, and/or a nonlinear free surface. For such cases, only the time-domain approach can be used.

Different levels of nonlinearity have been included in the computation of seakeeping problems in the time domain. The nonlinear effect of incident waves was studied in the work of Cong et al. (1998) and Qiu et al. (2001) with the Froude-Krylov and restoring forces calculated on the instantaneous wetted body surface, while the radiation and diffraction forces were still calculated on the mean wetted body surface.

A further step was to solve the so-called body-exact problem for large amplitude ship motions which considers the nonlinear effect introduced by the instantaneous wetted body surface on the solutions. The body-exact problem has been solved by Beck and Magee (1990), Lin and Yue (1990), and Danmeier (1999) using the free surface Green function. Recently, Qiu and Peng (2013) solved the body-exact problem for floating bodies with the panel-free method in the time domain. For the body-exact problem, the free surface boundary condition is still linear; therefore, the use of the free surface Green function is still valid.

The fully nonlinear problem considers the nonlinearity introduced by the instantaneous free surface. Computations have been performed by Raven (1996) and Scullen (1998) for steady ship wave problems and by Cao et al. (1991), Scorpio (1997), and Subramani (2000) for unsteady problems of wave-induced ship motions.

1.1.4 Rankine Panel Method

The Rankine panel method was first introduced by Gadd (1976) and Dawson (1977) to solve the wave patterns around a steadily advancing ship in calm water. In their

work, an image body was employed along with the original body to calculate the steady wave flow, based on which the free surface boundary condition was linearized. This linearization is also referred to as Double-Body linearization or Dawson linearization. Unlike the Neumann-Kelvin flow which is uniform, the Double-Body flow is determined by the shape of the geometry, which cannot be solved by only one free surface Green function (Beck, 1994). Thus, the distribution of the Rankine source on the free surface is required to solve the corresponding boundary value problem. In Gadd and Dawson's work, flat quadrilateral panels were used with constant distributions of source and dipole strengths over each panel. The Double-Body flow gives a more realistic description of the wave flow around the hull than the Neumann-Kelvin flow.

The employment of the Rankine panel method in solutions of seakeeping problems was not popular until Sclavounos and Nakos (1988) and Nakos and Sclavounos (1990a) studied the wave propagation on a discrete free surface and introduced a new discretization scheme for the free surface based on a B-spline representation, which brings no numerical damping and small numerical dispersion. In this scheme, the flat quadrilateral panels were retained; however, instead of being constant, the distributions of source and dipole strengths over the panels followed a bi-quadratic basis function based on the B-spline. Good representations of the unsteady wave flows and hydrodynamic forces were achieved. The B-spline Rankine panel method has been applied to solve ship motions in waves with forward speed in the frequency domain by Nakos and Sclavounos (1990b) and Sclavounos et al. (1994). In their work, the body boundary condition was enforced on the mean position of the wetted body surface and the free surface boundary conditions were linearized on the basis of Double-Body flow. Nakos et al. (1993) successfully extended the frequency domain formulation into the time domain. In their work, fully linear free surface and body boundary conditions

were used. The hydrodynamic forces were calculated directly by the integration of pressures over the hull surface. The equation of motions was solved simultaneously with the wave flow at each time step. Validity has been demonstrated for various ship hulls, Froude numbers, and wave frequencies. By using the same method, the second-order hydrodynamic forces for floating structures were calculated in the time domain by Kim et al. (1997).

The use of a simple Rankine source on the free surface allows a flexible choice in the linearization of the free surface boundary conditions. Based on the work of Nakos et al. (1993), Kring (1994) proposed a generalized linearization that can include Neumann-Kelvin, Double-Body, or displacement thickness boundary layer models. Kutta conditions were also proposed for ships with transom sterns. Based on the Weak-Scatterer hypothesis proposed by Pawlowski (1992), Huang (1997) studied the nonlinear ship motions with the free surface boundary condition linearized on the incident wave profile and the body boundary condition on the instantaneous wetted surface. The panels were regenerated at each time step on the submerged hull surface under the instantaneous incident wave profile. A predictor-corrector scheme was employed to solve the equations of motion. Recently, based on the Weak-Scatterer formulation, Kim et al. (2011) developed a program suite, WISH, to predict the motion responses and structural loads with different levels of nonlinearity. The use of the B-spline based Rankine panel method allows the continuity of the potential and its derivatives across panels and enables the analytical evaluation of first/second-order derivatives of potential over the free surface and body boundaries.

Different from the constant or the B-spline Rankine panel method, the higher-order boundary element method (HOBEM) uses higher-order elements as the panels. The panel geometry and the distributions of physical variables are described through shape functions. It is flexible to use the HOBEM for problems with complex geometries and

multiple bodies. Compared to the constant Rankine panel method, a smaller number of panels can be used in the HOBEM to reach the same level of accuracy for the results. The time-domain HOBEM has been applied in Kim and Kim (1997) to solve the problems of wave-body interactions, in Bai and Taylor (2006) to calculate the radiation problem of vertical cylinders, and in Kim and Kim (2011), Shao and Faltinsen (2012), and He and Kashiwagi (2014) to calculate the problems of seakeeping and added resistance.

In the Rankine panel method, the finite depth problem can be solved by the distribution of the Rankine sources on the bottom of the computational domain. Kim (1999) calculated the first/second-order hydrodynamic forces on a bottom-mounted cylinder with the B-spline Rankine panel method in the time domain. Kim and Kim (2013) computed the floating body motions in arbitrary bathymetry. In their work, the numerical wave tank approach was applied for the generation of the incident waves.

One common feature involved in the Rankine panel method is the use of the truncated free surface instead of the infinite one. Once the free surface is truncated, the radiation condition for infinite free surface cannot be satisfied. A numerical treatment originated from Israeli and Orszag (1981) was performed to absorb the outgoing waves through the absorption zone, so that the radiation condition in the far field can be satisfied. This treatment is widely used in zero forward speed cases.

Spatial filtering has been widely used as a smoothing technique in the time-domain simulation of free surface waves to suppress the growth of saw-tooth waves (Longuet-Higgins and Cokelet, 1976). For the Rankine panel method, the growth of saw-tooth waves on the truncated free surface brings instability into the solution. It is important to use low-pass filters to eliminate these very short waves. Since the wavelengths are very short, the energy loss caused by the filtering can be neglected. Different types of numerical filters were used in the work of Nakos et al. (1993), Kim et al. (1997),

Shao and Faltinsen (2012) and so forth.

1.1.5 Fully Nonlinear Free Surface

Besides the fully linear and the Weak-Scatterer formulations, a third alternative is the use of fully nonlinear free surface boundary conditions. Longuet-Higgins and Cokelet (1976) first proposed the so-called Mixed-Eulerian-Lagrangian (MEL) method to simulate the two-dimensional fully nonlinear free surface wave in the time domain. For each time step, the boundary value problem is first solved in an Eulerian frame. Then, in the Lagrangian phase, the wave elevations and potentials on the free surface are updated by the integration of fully nonlinear free surface boundary conditions. The equations of motion are then solved to update the position of the body and the normal velocity on the body surface. By applying this method, the calculation of wave-body interactions has been carried out by Faltinsen (1977). Cao et al. (1991) proposed a desingularized source method to solve the boundary integral equation for the three-dimensional unsteady ship wave problem. The isolated Rankine sources were distributed on the truncated free surface through a desingularized approach, which involves raising the sources above the collocation point, rather than the use of flat quadrilateral panels. Beck (1994) and Beck et al. (2001) gave detailed reviews on the use of fully nonlinear free surface for wave-body interaction problems using MEL methods in the time domain. Significant work has been done by Scorpio (1997), Finn (2003), Bandyk (2009), Yan (2010) and so forth. Kara et al. (2007) studied the steady ship-wave problem using fully nonlinear free surface boundary conditions with isolated Rankine sources. The large-amplitude two-dimensional body motions and three-dimensional seakeeping problem have been solved by Zhang et al. (2007), Zhang and Beck (2008), and Zhang et al. (2010) using the desingularized source method. Feng et al. (2015) solved the two-dimensional nonlinear wave-body interac-

tion problem using a continuous desingularized source distribution method with free surface Rankine sources placed on continuous panels rather than isolated points.

1.2 Overview

The objective of this thesis is to conduct three-dimensional time-domain simulations of wave-induced motions of ships and floating bodies. A numerical program has been developed to simulate the ship and floating body motions at zero forward speed. The time-domain Rankine panel method with constant distributions of source/dipole strengths has been applied to solve the boundary value problem with linear free surface and body boundary conditions. Simulations have been performed in both deep water and finite water depths.

Chapter 2 derives the mathematical formulations for the boundary value problem associated with wave-induced ship motions. A fully nonlinear formulation with a steady forward speed is first derived. Linearizations of the free surface and body boundary conditions are performed at different levels to obtain the Weak-Scatterer formulation and the linear formulation. The boundary integral equations is derived from Green's theorem. The equations of ship motion are also presented.

Chapter 3 presents the numerical method to solve the boundary value problem. The B-spline Rankine panel method is described in detail. The constant Rankine panel method used in this thesis is a degradation of the B-spline Rankine panel method. The typical computational domain is presented as well as the spatial and temporal discretization of the boundary integral equation. The numerical scheme for the wave absorbing beach and the numerical filter are presented. The explicit Euler scheme is applied for the time integration of the equations of motion. The numerical implementation for the program is described and a flow chart for the program is presented.

Chapter 4 presents the time-domain simulation results for various geometries, including a hemisphere, a truncated cylinder, the Wigley I hull, a Series 60 ship, and a two-body side-by-side moored scenario. The hydrodynamic forces and ship motions are studied through forced motion simulations and free motion simulations. For the forced motion simulations, the wave absorbing beach is verified at first. The added mass and damping coefficients of ships and floating bodies are calculated through forced periodical oscillations. The wave exciting forces are calculated on fixed bodies with the presence of incident monochromatic waves at head sea condition. For the free motion simulations, the total hydrodynamic forces and equations of ship motion are solved simultaneously at each time step. The motion response amplitude operators (RAOs) are obtained from the time series of ship motions. The numerical results from the present method are compared with the numerical results from MASP0 and WAMIT as well as experimental data.

Chapter 5 concludes the applications of the current work and provides promising future topics based on the present method.

Chapter 2

Mathematical Formulation

2.1 Boundary Value Problem

2.1.1 The Coordinate Systems

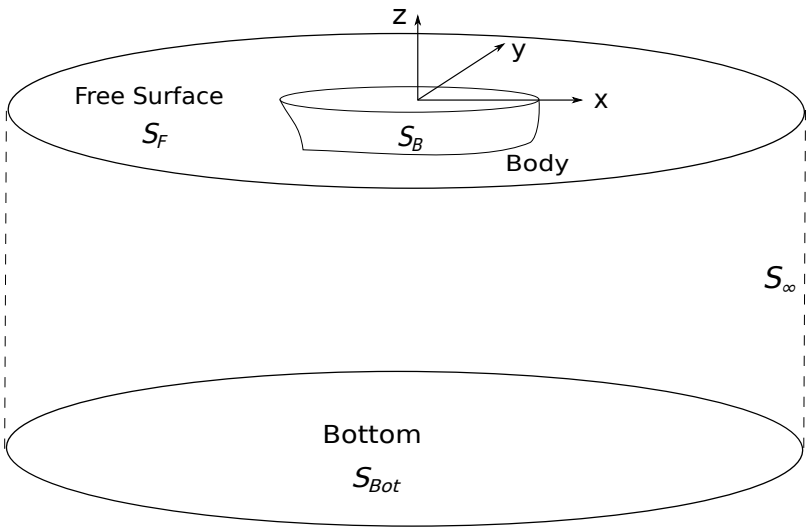

Figure 2.1: Coordinate system.

Figure 2.1 considers a freely floating ship in the presence of water waves with a steady advance speed U in a finite water depth.

Three Cartesian systems, $\vec{x}_0 = (x_0, y_0, z_0)$, $\vec{x} = (x, y, z)$, and $\vec{x}_s = (x_s, y_s, z_s)$ are used

as the reference systems to describe the problem of wave-body interactions. Frame $\vec{x}_0$ is fixed in space, while frame $\vec{x}$ travels along with the ship at a steady advance speed U. Frame $\vec{x}_s$ is fixed on the ship. The unsteady motion of the ship is defined as the oscillation of frame $\vec{x}_s$ in the frame $\vec{x}$. The positive x-axis of all frames are pointing upstream and the positive z-axis are pointing upwards. The boundary value problem are formulated in frame $\vec{x}$ and the equations of ship motion are solved in frame $\vec{x}_s$.

2.1.2 The Fully Nonlinear Formulation

Assuming the fluid is ideal and irrotational, which means the fluid is inviscid and incompressable and there is no fluid separation or lifting effect, a total velocity potential $\Phi(\vec{x}_0, t)$ in the space-fixed reference system satisfies the mass conservation principle,

$$\nabla^2\Phi(\vec{x}_0, t) = 0 \quad \text{in the fluid domain} \tag{2.1}$$

As a result, the velocity field $\vec{V}(\vec{x}_0, t)$ in the fluid domain is obtained by taking the gradient of the velocity potential $\Phi(\vec{x}_0, t)$. $\Phi(\vec{x}_0, t)$ and $\vec{V}(\vec{x}_0, t)$ are expressed as Φ and $\vec{V}$ hereinafter.

$$\vec{V} = \nabla\Phi = \frac{\partial\Phi}{\partial x_0}\vec{i}_0 + \frac{\partial\Phi}{\partial y_0}\vec{j}_0 + \frac{\partial\Phi}{\partial z_0}\vec{k}_0 = V_{x_0}\vec{i}_0 + V_{y_0}\vec{j}_0 + V_{z_0}\vec{k}_0, \tag{2.2}$$

where $\vec{i}_0$, $\vec{j}_0$, and $\vec{k}_0$ are the unit vectors in the fixed reference system $\vec{x}_0$. V_{x_0}, V_{y_0}, and V_{z_0} are the velocity components in the fluid domain.

The pressure field $p(\vec{x}_0, t)$ is defined through Bernoulli's equation by applying the principle of conservation of momentum in the space-fixed reference system as follows,

$$p(\vec{x}_0, t) - p_a = -\rho(\frac{\partial\Phi}{\partial t} + \frac{1}{2}\nabla\Phi\cdot\nabla\Phi + gz_0), \tag{2.3}$$

where p_a is the atmospheric pressure, ρ is the density of the fluid, z_0 is the coordinate of the water particle in the z_0 direction of the space-fixed reference system, and g is the acceleration of gravity.

The no-flux boundary conditions are applied on the submerged body surface S_B and bottom surface S_{Bot}.

The velocity component of the fluid which is normal to the submerged body surface S_B is equal to the normal velocity of the body.

$$\frac{\partial \Phi}{\partial n_B} = \vec{V}_{S_B} \cdot \vec{n}_B \quad \text{on} \quad S_B, \tag{2.4}$$

where $\vec{n}_B$ is the normal vector on the body surface pointing out from the fluid domain and into the body, and $\vec{V}_{S_B}$ is the instantaneous velocity of the body surface S_B in the space-fixed reference system.

For the bottom surface S_{Bot}, the velocity component of the fluid in the normal direction of the surface is equal to zero.

$$\frac{\partial \Phi}{\partial n_{Bot}} = 0 \quad \text{on} \quad S_{Bot}, \tag{2.5}$$

where $\vec{n}_{Bot}$ is the normal vector on the bottom surface pointing out from the fluid domain and into the sea floor.

The free surface boundary satisfies both the kinematic boundary condition and dynamic boundary condition in the space-fixed reference system $\vec{x_0}$.

The free surface is defined as $z_0 - \zeta_0(x_0, y_0, t) = 0$, $\zeta_0(x_0, y_0, t)$ being the instantaneous total wave elevation with respect to the space-fixed reference system $\vec{x}_0$. With the assumption that the fluid particle will remain on the free surface at all times, a

kinematic boundary condition is imposed on the free surface,

$$\frac{D}{Dt}[z_0 - \zeta_0(x_0, y_0, t)] = 0, \tag{2.6}$$

or,

$$(\frac{\partial}{\partial t} + \nabla\Phi \cdot \nabla)[z_0 - \zeta_0(x_0, y_0, t)] = 0. \tag{2.7}$$

The dynamic free surface boundary condition is that the fluid pressure $p(\vec{x}_0, t)$ is equal to the atmospheric pressure p_a on free surface $z_0 - \zeta_0(x_0, y_0, t) = 0$. From equation (2.3), the condition is as follows,

$$\frac{\partial\Phi}{\partial t} + \frac{1}{2}\nabla\Phi \cdot \nabla\Phi + gz_0 = 0. \tag{2.8}$$

On $z_0 = \zeta_0(x_0, y_0, t)$, equation (2.8) has the form as follows,

$$\zeta_0(x_0, y_0, t) = -\frac{1}{g}(\frac{\partial\Phi}{\partial t} + \frac{1}{2}\nabla\Phi \cdot \nabla\Phi). \tag{2.9}$$

Substituting equation (2.9) into equation (2.7), one can find,

$$(\frac{\partial}{\partial t} + \nabla\Phi \cdot \nabla)[z_0 + \frac{1}{g}(\frac{\partial\Phi}{\partial t} + \frac{1}{2}\nabla\Phi \cdot \nabla\Phi)] = 0 \quad \text{on} \quad z_0 = \zeta_0, \tag{2.10}$$

or,

$$\frac{\partial^2\Phi}{\partial t^2} + 2\nabla\Phi \cdot \nabla(\frac{\partial\Phi}{\partial t}) + \frac{1}{2}\nabla\Phi \cdot \nabla(\nabla\Phi \cdot \nabla\Phi) + g\frac{\partial\Phi}{\partial t} = 0 \quad \text{on} \quad z_0 = \zeta_0. \tag{2.11}$$

In the far field, a radiation condition is imposed so that the outgoing waves do not

reflect back into the fluid domain.

$$\nabla\Phi \to 0 \quad \text{at spatial infinity.} \tag{2.12}$$

The initial condition in the time domain for this boundary value problem is given that at the starting time t_0 the fluid is at rest.

$$\Phi = 0 \quad \text{in fluid domain,} \tag{2.13}$$

$$\frac{\partial\Phi}{\partial t} = 0 \quad \text{on} \quad z_0 = 0. \tag{2.14}$$

More detailed derivations of the fully nonlinear formulation of boundary problem above can be found in Nakos (1990) and Huang (1997).

2.1.3 The Coordinate System Transformation

The formulations of the fully nonlinear boundary value problem in section 2.1.2 are defined in the space-fixed reference system $\vec{x}_0$. In this frame, the fluid flow is unsteady and the body surface boundary and free surface boundary are moving. A transformation from the space-fixed reference system to the steadily advancing reference system $\vec{x}$ will facilitate the solution since the unsteady motion of the ship can be solved based on a steady flow after the transformation. The velocity potential is redefined in frame $\vec{x}$ as follows,

$$\Phi(\vec{x}_0, t) = \Phi(\vec{x} + \vec{U}t, t) \equiv \phi(\vec{x}, t), \tag{2.15}$$

where $\vec{U} = U\vec{i} + 0 \cdot \vec{j} + 0 \cdot \vec{k}$ is the velocity of the steadily advancing reference system $\vec{x}$ with $\vec{i}$, $\vec{j}$, and $\vec{k}$ being the unit vectors in frame $\vec{x}$, and $\phi(\vec{x}, t)$ is the redefined total velocity potential in frame $\vec{x}$.

As a result, the partial time derivative of $\Phi(\vec{x}_0, t)$ taken in frame $\vec{x}_0$ will be transformed

as follows,

$$\frac{\partial \Phi(\vec{x}_0, t)}{\partial t} = (\frac{\partial}{\partial t} - \vec{U} \cdot \nabla)\phi(\vec{x}, t) \tag{2.16}$$

via a Galilean transformation. Thus, the kinematic and dynamic free surface boundary conditions equation (2.6) and (2.8) are transformed to frame $\vec{x}$ as follows,

$$[\frac{\partial}{\partial t} - (\vec{U} - \nabla\phi) \cdot \nabla]\zeta = \frac{\partial \phi}{\partial z} \quad \text{on} \quad z = \zeta, \tag{2.17}$$

$$[\frac{\partial}{\partial t} - (\vec{U} - \nabla\phi) \cdot \nabla]\phi = \frac{1}{2}\nabla\phi \cdot \nabla\phi - g\zeta \quad \text{on} \quad z = \zeta, \tag{2.18}$$

where ζ is the total wave elevation in frame $\vec{x}$. Both conditions are imposed on $z = \zeta$. After the coordinate system transformation, the physical problem is formulated in frame $\vec{x}$.

2.1.4 The Weak-Scatterer Formulation

In the fully nonlinear formulation derived in the previous section, the free surface conditions are highly nonlinear. Furthermore, they are enforced on a surface which is not known in advance. As a linearization scheme of the fully nonlinear problem, the Weak-Scatterer formulation, which was first proposed by Pawlowski (1992), allows the free surface boundary conditions to be linearized on the instantaneous incident wave surface ζ^I under the assumption that the radiation and diffraction wave are much smaller than the incident wave. The decomposition of velocity potential and wave elevation for Weak-Scatterer formulation is as follows,

$$\phi = \phi^B + \phi^I + \phi^d, \tag{2.19}$$

$$\zeta = \zeta^I + \zeta^d, \tag{2.20}$$

where ϕ^d and ζ^d are the disturbance wave velocity potential and elevation, respectively, containing both the radiation wave induced by the unsteady ship motion and the diffraction of incoming waves due to the presence of the ship hull. Among the velocity potential and wave elevation components, the basis flow ϕ^B and the incident wave (ϕ^I, ζ^I) are assumed to be much larger than the disturbance wave (ϕ^d, ζ^d). Thus, the order of the basis, incident, and disturbed wave components are as follows,

$$\phi^B \sim \mathcal{O}(1); \quad \phi^I \sim \mathcal{O}(1); \quad \phi^d \sim \mathcal{O}(\epsilon), \tag{2.21}$$

$$\zeta^I \sim \mathcal{O}(1); \quad \zeta^d \sim \mathcal{O}(\epsilon). \tag{2.22}$$

where $\epsilon \ll 1$. Substituting the decompositions (2.19,2.20) into the free surface conditions (2.17,2.18), and applying Taylor's expansion about the incident wave surface, one will find the kinematic and dynamic Weak-Scatterer free surface boundary con-

ditions as follows,

$$
\begin{aligned}
[\frac{\partial}{\partial t} - (\vec{U} - \nabla\phi^B - \nabla\phi^I)\cdot\nabla]\zeta^d = & \\
& -[\frac{\partial}{\partial t} - (\vec{U} - \nabla\phi^B - \nabla\phi^I - \nabla\phi^d)\cdot\nabla]\zeta^I \\
& + \frac{\partial\phi^B}{\partial z} + \frac{\partial\phi^I}{\partial z} + \frac{\partial\phi^d}{\partial z} \\
& + \zeta^d[\frac{\partial^2\phi^B}{\partial z^2} - \nabla(\frac{\partial\phi^B}{\partial z} + \frac{\partial\phi^I}{\partial z})\cdot\nabla\zeta^I] \\
& \text{on} \quad z = \zeta^I, \\
[\frac{\partial}{\partial t} - (\vec{U} - \nabla\phi^B - \nabla\phi^I)\cdot\nabla]\phi^d = & \\
& -[\frac{\partial}{\partial t} - (\vec{U} - \nabla\phi^B - \nabla\phi^I)\cdot\nabla]\phi^I + \frac{1}{2}\nabla\phi^I\cdot\phi^I \\
& -[\frac{\partial}{\partial t} - (\vec{U} - \nabla\phi^B)\cdot\nabla]\phi^B + \frac{1}{2}\nabla\phi^B\cdot\phi^B \\
& - g(\zeta^I + \zeta^d) \\
& - \zeta^d[\frac{\partial}{\partial t} - (\vec{U} - \nabla\phi^B - \nabla\phi^I]\frac{\partial\phi^I}{\partial z} \\
& - \zeta^d[\frac{\partial}{\partial t} - (\vec{U} - \nabla\phi^B - \nabla\phi^I]\frac{\partial\phi^B}{\partial z} \\
& \text{on} \quad z = \zeta^I.
\end{aligned}
\tag{2.23, 2.24}
$$

The body boundary conditions in the Weak-Scatterer formulation are imposed on the exact body surface S_B. S_B is the actual submerged part of the ship body under the instantaneous incident wave profile. With the fluid velocity equal to the velocity of the body at the same location, the body boundary condition is written as follows,

$$
\frac{\partial\phi}{\partial n} = \vec{U}\cdot\vec{n} + \frac{\partial\vec{\delta}}{\partial t}\cdot\vec{n} \quad \text{on} \quad S_B, \tag{2.25}
$$

where $\vec{\delta}$ is the displacement of the ship about its equilibrium position in the steadily advancing reference system $\vec{x}$ and is defined as follows,

$$\vec{\delta} = \vec{\xi}_T + \vec{\xi}_R \times \vec{r}, \tag{2.26}$$

where $\vec{\xi}_T$ and $\vec{\xi}_R$ are the translational and rotational displacement of the ship-fixed frame with respect to the steadily advancing frame $\vec{x}$. $\vec{r}$ is the position of a point on the body surface in the ship-fixed frame $\vec{x}_s$.

The conditions for each components of the total velocity potential are defined as follows,

$$\frac{\partial \phi^B}{\partial n} = \vec{U} \cdot \vec{n} \quad \text{on} \quad S_B, \tag{2.27}$$

$$\frac{\partial \phi^d}{\partial n} = \frac{\partial \vec{\delta}}{\partial t} \cdot \vec{n} - \frac{\partial \phi^I}{\partial n} \quad \text{on} \quad S_B. \tag{2.28}$$

There is no need to include the so-called m-terms, which accounts for the interaction effect between the steady and the unsteady flows, in the body boundary of the Weak-Scatterer formulation, because the interaction effect is already included by applying the exact body surface boundary condition.

More detailed derivations of the Weak-Scatterer formulation can be found in Huang (1997) and Kim et al. (2011).

2.1.5 The Linear Formulation

In the linear formulation, the free surface boundary conditions are linearized on the undisturbed surface $z = 0$. Both the incoming wave (ϕ^I,ζ^I) and the disturbance wave (ϕ^d,ζ^d) are assumed to be much smaller than the basis flow ϕ^B. Thus, the order of the

basis, incident, and disturbed wave components for the linear problem are as follows,

$$\phi^B \sim \mathcal{O}(1); \quad \phi^I \sim \mathcal{O}(\epsilon); \quad \phi^d \sim \mathcal{O}(\epsilon), \tag{2.29}$$

$$\zeta^I \sim \mathcal{O}(\epsilon); \quad \zeta^d \sim \mathcal{O}(\epsilon). \tag{2.30}$$

where $\epsilon \ll 1$. The linear kinematic and dynamic free surface boundary conditions are degraded from equation (2.23,2.24) by transferring the condition from $z = \zeta^I$ to $z = 0$ and omitting the higher order term $\mathcal{O}(\epsilon^2)$.

$$\begin{aligned}
[\frac{\partial}{\partial t} - (\vec{U} - \nabla\phi^B) \cdot \nabla]\zeta^d = & \\
& + (\vec{U} - \nabla\phi^B) \cdot \nabla\zeta^I \\
& + \frac{\partial\phi^d}{\partial z} \\
& + \zeta^d \frac{\partial^2\phi^B}{\partial z^2} \\
& \text{on} \quad z = 0,
\end{aligned} \tag{2.31}$$

$$\begin{aligned}
[\frac{\partial}{\partial t} - (\vec{U} - \nabla\phi^B) \cdot \nabla]\phi^d = & \\
& + (\vec{U} - \nabla\phi^B) \cdot \nabla\phi^I \\
& - [\frac{\partial}{\partial t} - (\vec{U} - \nabla\phi^B) \cdot \nabla]\phi^B + \frac{1}{2}\nabla\phi^B \cdot \phi^B \\
& - g\zeta^d \\
& \text{on} \quad z = 0.
\end{aligned} \tag{2.32}$$

The body boundary conditions in the linear formulation are imposed on the mean surface of the submerged ship body $\bar{S}_B$. Therefore, the m-terms have to be included in the body boundary condition to account for the interaction effect between the

steady and unsteady waves.

$$\frac{\partial \phi}{\partial n} = \vec{U} \cdot \vec{n} + \frac{\partial \vec{\delta}}{\partial t} \cdot \vec{n} + \vec{\delta} \cdot \vec{m} \quad \text{on} \quad \bar{S}_B, \tag{2.33}$$

The ship displacement $\vec{\delta}$ is defined in equation (2.26). The translational and rotational displacement $\vec{\xi}_T$ and $\vec{\xi}_R$, the normal vector $\vec{n}$, and the m-terms are as follows,

$$(\xi_1, \xi_2, \xi_3) = \vec{\xi}_T, \quad (\xi_4, \xi_5, \xi_6) = \vec{\xi}_R, \tag{2.34}$$

$$(n_1, n_2, n_3) = \vec{n}, \quad (n_4, n_5, n_6) = \vec{r} \times \vec{n}, \tag{2.35}$$

$$\begin{aligned} (m_1, m_2, m_3) &= (\vec{n} \cdot \nabla)(\vec{U} - \nabla \phi^B), \\ (m_4, m_5, m_6) &= (\vec{n} \cdot \nabla)[\vec{r} \times (\vec{U} - \nabla \phi^B)]. \end{aligned} \tag{2.36}$$

The conditions for each component of the total velocity potential are defined as follows,

$$\frac{\partial \phi^B}{\partial n} = \vec{U} \cdot \vec{n} \quad \text{on} \quad \bar{S}_B, \tag{2.37}$$

$$\frac{\partial \phi^d}{\partial n} = \frac{\partial \vec{\delta}}{\partial t} \cdot \vec{n} + \vec{\delta} \cdot \vec{m} - \frac{\partial \phi^I}{\partial n} \quad \text{on} \quad \bar{S}_B. \tag{2.38}$$

The linear formulation for the zero speed scenario is degraded from the non-zero speed formulation by setting $\vec{U} = 0$ and $\phi^B = 0$ as follows,

-Linear Formulation (zero speed)

In the fluid domain,

$$\nabla^2 \phi = 0. \tag{2.39}$$

On the free surface, $z = 0$,

$$\frac{\partial \zeta^d}{\partial t} = \frac{\partial \phi^d}{\partial z}, \tag{2.40}$$

$$\frac{\partial \phi^d}{\partial t} = -g\zeta^d. \tag{2.41}$$

On the body surface, $\bar{S}_B$,

$$\frac{\partial \phi^d}{\partial n} = \frac{\partial \vec{\delta}}{\partial t} \cdot \vec{n} - \frac{\partial \phi^I}{\partial n}. \tag{2.42}$$

On the bottom surface, $S_{Bot}(z = -h)$,

$$\frac{\partial \phi^d}{\partial z} = 0. \tag{2.43}$$

where $\vec{\delta}$ is the vector of ship displacement with respect to frame $\vec{x}$. h is the water depth.

The disturbance velocity potential ϕ^d and wave elevation ξ^d are further decomposed into radiation and diffraction velocity potentials and wave elevations based on the superposition principle as follows,

$$\phi^d = \phi^R + \phi^D, \tag{2.44}$$

$$\zeta^d = \zeta^R + \zeta^D. \tag{2.45}$$

The formulation for radiation and diffraction problems are as follows,

-Radiation Problem

In the fluid domain,

$$\nabla^2 \phi = 0. \tag{2.46}$$

On the free surface, $z = 0$,

$$\frac{\partial \zeta^R}{\partial t} = \frac{\partial \phi^R}{\partial z}, \tag{2.47}$$

$$\frac{\partial \phi^R}{\partial t} = -g\zeta^R. \tag{2.48}$$

On the body surface, $\bar{S}_B$,

$$\frac{\partial \phi^R}{\partial n} = \frac{\partial \vec{\delta}}{\partial t} \cdot \vec{n}. \tag{2.49}$$

On the bottom surface, $S_{Bot}(z = -h)$,

$$\frac{\partial \phi^R}{\partial z} = 0. \tag{2.50}$$

-Diffraction Problem

In the fluid domain,

$$\nabla^2 \phi = 0. \tag{2.51}$$

On the free surface, $z = 0$,

$$\frac{\partial \zeta^D}{\partial t} = \frac{\partial \phi^D}{\partial z}, \tag{2.52}$$

$$\frac{\partial \phi^D}{\partial t} = -g\zeta^D. \tag{2.53}$$

On the body surface, $\bar{S}_B$,

$$\frac{\partial \phi^D}{\partial n} = -\frac{\partial \phi^I}{\partial n}. \tag{2.54}$$

On the bottom surface, $S_{Bot}(z = -h)$,

$$\frac{\partial \phi^D}{\partial z} = 0. \tag{2.55}$$

For the diffraction problem, a small-amplitude water wave is imposed as the incident wave as follows,

$$\phi^I = -\frac{H}{2}\frac{g}{\omega}\frac{\cosh k(h+z)}{\cosh kh}\sin(kx - \omega t). \tag{2.56}$$

The hydrodynamic pressure p can be decomposed into three parts as follows,

$$p = p^I + p^R + p^D, \tag{2.57}$$

where p^I , p^R, and p^D are the pressure induced by incident, radiation, and diffraction

wave components, respectively. The pressures are computed as follows,

$$p^I = -\rho \frac{\partial \phi^I}{\partial t}, \tag{2.58}$$

$$p^R = -\rho \frac{\partial \phi^R}{\partial t}, \tag{2.59}$$

$$p^D = -\rho \frac{\partial \phi^D}{\partial t}. \tag{2.60}$$

The hydrodynamic force F_j, including three force components , F_1, F_2, F_3 along (x, y, z) axis and three moment components, F_4, F_5, F_6 about (x, y, z) axis, acting on the body is obtained by the integration of the hydrodynamic pressure p over the submerged body surface.

$$F_j = \rho \iint_{S_B} p \cdot n_j ds \quad \text{for} \quad j = 1, 2, ..., 6, \tag{2.61}$$

with the generalized normal, n_j defined in equation (2.35).

2.2 Boundary Integral Equation

The boundary value problems above can be transformed into boundary integral equations by adopting Green's Theorem.

2.2.1 Green's Theorem

In applying the divergence theorem to a continuously differentiable vector field $\vec{A} = (A_1, A_2, A_3)$ in a fluid domain, v, bounded by a closed surface, s, one can find,

$$\iiint_v (\nabla \cdot \vec{A}) dv = \iint_s (\vec{A} \cdot \vec{n}) ds, \tag{2.62}$$

where $\vec{n}$ is the normal vector of points on s pointing to the exterior of fluid domain v. Let $\vec{A} = \phi\nabla\varphi$,

$$\iiint_v (\phi\nabla^2\varphi + \nabla\phi \cdot \nabla\varphi)dv = \iint_s \phi\frac{\partial\varphi}{\partial n}ds, \tag{2.63}$$

where both ϕ and φ satisfy the Laplace equation. Again, let $\vec{A} = \varphi\nabla\phi$,

$$\iiint_v (\varphi\nabla^2\phi + \nabla\varphi \cdot \nabla\phi)dv = \iint_s \varphi\frac{\partial\phi}{\partial n}ds. \tag{2.64}$$

From equation (2.63,2.64), one can find,

$$\iint_s (\phi\frac{\partial\varphi}{\partial n} - \varphi\frac{\partial\phi}{\partial n})ds = \iiint_v (\phi\nabla^2\varphi + \nabla\phi \cdot \nabla\varphi - \varphi\nabla^2\phi - \nabla\varphi \cdot \nabla\phi)dv = 0. \tag{2.65}$$

2.2.2 Distribution of Singularities

Since the shape of a body surface in the fluid domain can be represented by distributing source and sink or dipoles on the geometry of the body surface, φ is replaced by the velocity potential created by a source as follows,

$$\varphi = \frac{1}{4\pi}\frac{1}{\|\vec{x}_P - \vec{x}_Q\|} = \frac{1}{4\pi}\frac{1}{r_{PQ}}, \tag{2.66}$$

where P is the field point in fluid domain, Q is the source point on the domain boundaries, $\vec{x}_P$ and $\vec{x}_Q$ are the coordinates where P and Q are located, and r_{PQ} is the distance between P and Q.

Since φ does not satisfy the Laplace equation at the singular point $r_{PQ} = 0$ when the source point is located in the fluid domain, a small sphere surface s_ε with radius $r_{PQ} = \varepsilon$ is introduced to surround the source point. Thus, the integral equation (2.65)

is valid in the volume exterior s_ε and interior s with replaced φ as follows,

$$\frac{1}{4\pi}\iint\limits_{s+s_\varepsilon}[\phi\frac{\partial}{\partial n}(\frac{1}{r_{PQ}})-\frac{1}{r_{PQ}}\frac{\partial\phi}{\partial n}]ds=0, \tag{2.67}$$

or,

$$\frac{1}{4\pi}\iint\limits_{s}[\phi\frac{\partial}{\partial n}(\frac{1}{r_{PQ}})-\frac{1}{r_{PQ}}\frac{\partial\phi}{\partial n}]ds=-\frac{1}{4\pi}\iint\limits_{s_\varepsilon}[\phi\frac{\partial}{\partial n}(\frac{1}{r_{PQ}})-\frac{1}{r_{PQ}}\frac{\partial\phi}{\partial n}]ds. \tag{2.68}$$

The area of sphere surface s_ε is $4\pi r_{PQ}^2$. Since the normal vector and the vector of r_{PQ} are in the opposite direction, the normal derivative of $\frac{1}{r_{PQ}}$ is $\frac{\partial}{\partial n}(\frac{1}{r_{PQ}})=-(-\frac{1}{r_{PQ}^2})=\frac{1}{r_{PQ}^2}$, the right hand side of equation (2.68) becomes,

$$\begin{aligned}-\frac{1}{4\pi}\iint\limits_{s_\varepsilon}[\phi\frac{\partial}{\partial n}(\frac{1}{r_{PQ}})-\frac{1}{r_{PQ}}\frac{\partial\phi}{\partial n}]ds&\\ =-\frac{1}{4\pi}[\phi(\frac{1}{r_{PQ}^2})-\frac{1}{r_{PQ}}\frac{\partial\phi}{\partial n}]4\pi r_{PQ}^2&\\ =-\phi+r_{PQ}\frac{\partial\phi}{\partial n}.&\end{aligned} \tag{2.69}$$

As $\varepsilon\to 0$, $r_{PQ}\frac{\partial\phi}{\partial n}\to 0$. The right hand side of equation (2.68) is equal to $-\phi(P)$ which is the velocity potential of field point P. Thus, when the field point is located inside s as follows,

$$\phi(P)=-\frac{1}{4\pi}\iint\limits_{s}[\phi(Q)\frac{\partial}{\partial n}(\frac{1}{r_{PQ}})-\frac{1}{r_{PQ}}\frac{\partial\phi(Q)}{\partial n}]ds. \tag{2.70}$$

If the field point P is located on s, the surface s_ε is chosen to be a hemisphere. Similarly, the potential at P is as follows,

$$\phi(P)=-\frac{1}{2\pi}\iint\limits_{s}[\phi(Q)\frac{\partial}{\partial n}(\frac{1}{r_{PQ}})-\frac{1}{r_{PQ}}\frac{\partial\phi(Q)}{\partial n}]ds. \tag{2.71}$$

If the field point P is located outside s,

$$0 = \iint_s [\phi(Q)\frac{\partial}{\partial n}(\frac{1}{r_{PQ}}) - \frac{1}{r_{PQ}}\frac{\partial \phi(Q)}{\partial n}]ds. \tag{2.72}$$

2.2.3 Boundary Integral Equations for Radiation and Diffraction Problems

The Rankine source is distributed on the body surface S_B, free surface S_F, and bottom surface S_{Bot}. The formulation of the boundary integral equation for radiation and diffraction problems is shown below,

$$2\pi\phi^k(P) + \iint_S \phi^k(Q)\frac{\partial}{\partial n_Q}G(P;Q)dS_Q - \iint_S \frac{\partial \phi^k(Q)}{\partial n_Q}G(P;Q)dS_Q = 0 \tag{2.73}$$

where $G(P;Q)$ is the Rankine source potential,

$$G(P;Q) = \frac{1}{\|\vec{x}_P - \vec{x}_Q\|} \tag{2.74}$$

$S = S_B \cup S_F \cup S_{Bot}$, P is the field point which is approaching the domain boundary, Q is the source point on the domain boundaries. $\vec{x}_P$ and $\vec{x}_Q$ are the coordinates where P and Q are located. n_Q is the normal vector at Q. $\phi^k(P)$ and $\phi^k(Q)$ are potential velocity at P and Q, where $k = 1$ for the radiation problem, $k = 2$ for the diffraction problem, and $k = 3$ for the free motion problem. The integral equation is enforced at P, which relates the velocity potential to its normal derivative over the domain boundaries.

2.3 Equations of Ship Motion

Governed by Newton's second law, the linear equations of ship motion are written as follows,

$$M_{jk}\,\ddot{\xi}_k(t) + C_{jk}\,\xi_k(t) = F_j(t) + F_j^{EX}(t), \tag{2.75}$$

where M_{jk} is the inertia matrix, C_{jk} is the restoring coefficient matrix, $F_j(t)$ is the hydrodynamic forces calculated in equation (2.61), and $\xi_k(k = 1, 2, ..., 6)$ is the vector of ship displacement in 6-DOF. $F_j^{EX}(t)$ accounts for the external forces. For a vessel with port-starboard symmetry, the inertia matrix is written as follows,

$$M_{jk} = \begin{Bmatrix} m & 0 & 0 & 0 & mz_s^G & 0 \\ 0 & m & 0 & -mz_s^G & 0 & mx_s^G \\ 0 & 0 & m & 0 & -mx_s^G & 0 \\ 0 & -mz_s^G & 0 & I_{44} & 0 & -I_{46} \\ mz_s^G & 0 & -mx_s^G & 0 & I_{55} & 0 \\ 0 & mx_s^G & 0 & -I_{64} & 0 & I_{66} \end{Bmatrix}, \tag{2.76}$$

where (x_s^G, 0, z_s^G) are the coordinates of the center of gravity of the ship in the ship-fixed frame $\vec{x}_s$, m is the total mass of the ship, I_{44}, I_{55}, and I_{66} are moments of inertia around the x_s, y_s, and z_s axes, respectively, I_{46} is roll - yaw product of inertia, which equals I_{64}.

There is no distinction between frame $\vec{x} = (x, y, z)$ and frame $\vec{x}_s = (x_s, y_s, z_s)$ for the linearized equations of ship motion. Since the formulation of the boundary value problem is written with respect to frame $\vec{x} = (x, y, z)$, it is more convenient to solve the equations of motion in frame $\vec{x} = (x, y, z)$. Therefore, the equations of ship motion in this thesis are solved in frame $\vec{x} = (x, y, z)$.

The restoring coefficient matrix C_{jk} describes the restoring force/moment in the j-th

direction due to a unit motion in the k-th mode. The restoring coefficients about the origin $\vec{x} = (0, 0, 0)$ include the hydrostatic restoring coefficients due to the change of hydrostatic force/moment and the gravitational restoring coefficients caused by the change of the relative position of center of gravity to the origin $\vec{x} = (0, 0, 0)$. The hydrostatic restoring coefficient matrix C_{jk}^H are calculated following the approach for generalized modes in the work of Newman (1994). The shape function $\vec{S}_k(\vec{x})$ is introduced to describe the displacement of an arbitrary point $\vec{x} = (x, y, z)$ on the body due to motion in the k-th mode. The shape function is defined by $\vec{S}_k(\vec{x}) = (u_k, v_k, w_k)$ for the k-th mode, where,

$$\begin{aligned} &\vec{S}_1 = (1, 0, 0), \quad \vec{S}_2 = (0, 1, 0), \quad \vec{S}_3 = (0, 0, 1), \\ &\vec{S}_4 = \vec{S}_1 \times \vec{x}, \quad \vec{S}_5 = \vec{S}_2 \times \vec{x}, \quad \vec{S}_6 = \vec{S}_3 \times \vec{x}. \end{aligned} \tag{2.77}$$

The component of $\vec{S}_k$ on the normal direction of the body surface S_B is defined as n_k as follows,

$$n_k = \vec{S}_k \cdot \vec{n} = u_k n_x + v_k n_y + w_k n_z. \tag{2.78}$$

The generalized hydrostatic restoring coefficients takes the form,

$$C_{jk}^H = \rho g \iint_{S_B} n_k w_j ds. \tag{2.79}$$

The gravitational restoring matrix C_{jk}^G about the origin $\vec{x} = (0, 0, 0)$ is calculated separately based on the change of the relative position of the center of gravity $\vec{x}_g$. The shape function of the center of gravity $\vec{G}_k(\vec{x}_g)$ for the k-th mode takes the form,

$$\begin{aligned} &\vec{G}_1 = (1, 0, 0), \quad \vec{G}_2 = (0, 1, 0), \quad \vec{G}_3 = (0, 0, 1), \\ &\vec{G}_4 = \vec{G}_1 \times \vec{x}_g, \quad \vec{G}_5 = \vec{G}_2 \times \vec{x}_g, \quad \vec{G}_6 = \vec{G}_3 \times \vec{x}_g. \end{aligned} \tag{2.80}$$

The change of gravitational restoring moments in the j-th direction due to a unit motion in the k-th mode takes the form,

$$\begin{aligned}(C_{1k}^G, C_{2k}^G, C_{3k}^G) &= (0,0,0),\\ (C_{4k}^G, C_{5k}^G, C_{6k}^G) &= \rho g \nabla \vec{G}_k \times \vec{n}_g.\end{aligned} \tag{2.81}$$

where ∇ is the displacement of the ship, $\vec{n}_g = (0,0,-1)$ is the direction of the gravitational force.

The restoring coefficient matrix takes the form,

$$C_{jk} = C_{jk}^H + C_{jk}^G. \tag{2.82}$$

In this thesis, the roll moment F_4^* cause by the viscous roll damping is considered and included in the hydrodynamic force F_4, which takes the form,

$$F_4^*(t) = -\beta\, b_c\, \dot{\xi}_4(t), \tag{2.83}$$

where b_c is the critical roll damping with the expression $b_c = 2\sqrt{C_{44}\, I_{44}}$, β is the ratio of the viscous roll damping to the critical roll damping. In this thesis, the value of β is obtained experimentally from the roll decay test.

Chapter 3

Numerical Method

3.1 Time Domain Rankine Panel Method

In this thesis, the Rankine panel method is applied in the time domain to solve the boundary value problem for seakeeping. The B-spline Rankine panel method developed in Sclavounos and Nakos (1988) and Nakos (1990) is described in detail. The constant Rankine panel method, which is degraded from the B-spline Rankine panel method, is used as the numerical method to solve the boundary value problem. The continuous boundary value problem formulated in Chapter 2 can be solved numerically in the time domain by the discretization of the computational domain spatially and temporally.

3.1.1 Spatial Discretization

Basis Functions

Since the boundary value problem only solves for the unknown physical quantities on the domain boundaries, including the body boundary, the truncated free surface boundary, and the bottom boundary, only these boundary surfaces need to be dis-

cretized. In the B-spline Rankine panel method proposed in Sclavounos and Nakos (1988), the body surface and truncated free surface is discretized into flat quadrilateral panels. The unknowns of the physical quantities $\psi(\hat{x},\hat{y})$ on the panels are represented by B-spline basis functions $B_j(\hat{x},\hat{y})$ with a finite number of spline coefficients ψ_j with respect to the local coordinate system $(\hat{x},\hat{y})$, as follows,

$$\psi(\hat{x},\hat{y}) \simeq \sum_{j=-\infty}^{+\infty} \psi_j B_j^{(m,n)}(\hat{x},\hat{y}) = \sum_{j=-\infty}^{+\infty} \psi_j b_j^{(m)}(\hat{x}) b_j^{(n)}(\hat{y}), \tag{3.1}$$

where $B_j^{(m,n)}$ is the two-dimensional basis function of the (m,n)-th order, which is the product of the one-dimensional basis functions of the m-th order $b_j^{(m)}(\hat{x})$ in $\hat{x}$-direction, and of the n-th order $b_j^{(n)}(\hat{y})$ in $\hat{y}$-direction, ψ_j is the corresponding degrees of freedom. The zero order basis function $b^{(0)}(\hat{x})$ is written as follows,

$$b^{(0)}(\hat{x}) = \begin{cases} 1, & \|\hat{x}\| \le \Delta\hat{x}/2 \\ 0, & \|\hat{x}\| > \Delta\hat{x}/2 \end{cases}, \tag{3.2}$$

where $\Delta\hat{x}$ is the size of panel in the local coordinate system. The basis function with higher order $b^{(m)}(\hat{x})$ can be obtained by convolution as follows,

$$b^{(m)}(\hat{x}) = \frac{1}{\Delta\hat{x}} \int_{-\infty}^{\infty} b^{(m-1)}(\xi) b^{(0)}(\hat{x}-\xi), \text{ for } m > 1. \tag{3.3}$$

The advantage of using a basis function to represent the unknowns $\psi(\hat{x},\hat{y})$ is that the derivatives of the unknowns can be calculated with much convenience and accuracy by analytical differentiation rather than numerical interpolation. The basis function can be differentiated in the $\hat{x}$-direction and $\hat{y}$-direction. The higher the order of the basis function, the higher the order of derivatives can be calculated. Since the second order derivatives are important for seakeeping problems, the bi-quadratic basis function

$B^{(2,2)}(\hat{x},\hat{y})(m=2,n=2)$ is chosen as the approximation of unknowns in Sclavounos and Nakos (1988), Nakos (1990), Kring (1994), Huang (1997), Kim (1999), and so forth with the quadratic basis function $b^{(2)}(\hat{x})$ written as follows,

$$b^{(2)}(\hat{x}) = \begin{cases} \frac{1}{2\Delta\hat{x}^2}(\hat{x}+\frac{3\Delta\hat{x}}{2})^2, & -\frac{3\Delta\hat{x}}{2} < \hat{x} \leq -\frac{\Delta\hat{x}}{2} \\ \frac{1}{\Delta\hat{x}^2}(-\hat{x}^2+\frac{3\Delta\hat{x}^2}{4}), & -\frac{-\Delta\hat{x}}{2} < \hat{x} \leq \frac{\Delta\hat{x}}{2} \\ \frac{1}{2\Delta\hat{x}^2}(-\hat{x}+\frac{3\Delta\hat{x}}{2})^2, & \frac{\Delta\hat{x}}{2} < \hat{x} \leq \frac{3\Delta\hat{x}}{2} \end{cases} . \tag{3.4}$$

In their work, the unknowns of velocity potential ϕ, normal velocity $\frac{\partial\phi}{\partial n}$, and the free surface wave elevation ζ are approximated at the centroid of each panel as follows,

$$\phi(\vec{x},t) \simeq \sum_{j=1}^{9}(\phi)_j(t)B_j^{(2,2)}(\vec{x}), \tag{3.5}$$

$$\frac{\partial\phi}{\partial n} \simeq \sum_{j=1}^{9}(\frac{\partial\phi}{\partial n})_j(t)B_j^{(2,2)}(\vec{x}), \tag{3.6}$$

$$\zeta(\vec{x},t) \simeq \sum_{j=1}^{9}(\zeta)_j(t)B_j^{(2,2)}(\vec{x}), \tag{3.7}$$

where $(\phi)_j(t)$, $(\frac{\partial\phi}{\partial n})_j(t)$, and $(\zeta)_j(t)$ are the time-dependent spline coefficients, $B_j^{(2,2)}(\vec{x})$ is the bi-quadratic B-spline basis function, and j is the summation index and $j = 1,2,...,9$. $\vec{x}$ is the position vector of the centroid of each panel in the global coordinate system. The velocity potential ϕ and normal velocity $\frac{\partial\phi}{\partial n}$ are distributed on the free surface, body surface, and the bottom surface; while the free surface wave elevation ζ is only for the free surface.

In the bi-quadratic B-spline Rankine panel method, the unknown on each panel supports nine panels including the panel itself and the eight panels surrounding it, which is the area across $-\frac{3\Delta\hat{x}}{2} \rightarrow \frac{3\Delta\hat{x}}{2}$ and $-\frac{3\Delta\hat{y}}{2} \rightarrow \frac{3\Delta\hat{y}}{2}$. For example, the velocity potential ϕ on one panel centroid contributes to the velocity potential not only on the panel

itself, but also the velocity potential on the other eight panels surrounding it. In the other way, the velocity potential on an arbitrary point of a panel (except the centroid) is the summation of the velocity potential contributed by the panel itself and the surrounding eight panels. The overlapping of the supporting area of bi-quadratic basis functions maintains the continuity of the unknowns and the first derivatives of the unknowns on the panel.

In this thesis, since the linear formulation is applied at zero speed and the second order terms are neglected, the zero-order basis function is accurate enough for the simulation of the present problem and therefore used to approximate the unknowns of $(\phi)_j(t)$, $(\frac{\partial \phi}{\partial n})_j(t)$, and $(\zeta)_j(t)$. In this case, the distribution of unknown physical quantities of the constant over the quadrilateral panels and the supporting area of each panel is within itself.

Computational Domain

The computational domain consists of the computational grids on boundary surfaces that represent the geometries of free surface, body surface, and bottom surface. Each grid is discretizd into flat quadrilateral panels with the normal direction pointing out of the fluid. The free surface radiation condition is satisfied by applying an artificial damping zone on the outer rim of the truncated free surface grid, which will be discussed in the following section.

A typical oval-type computational domain setup for the Series 60, Cb=0.7 hull is shown in Figure 3.1. The submerged body surface, the truncated free surface, and the bottom surface are discretized into quadrilateral panels. The size of the truncated free surface is mainly determined by the wavelength of incident waves. The spacing of the panels on the free surface and bottom surface are exponentially varied so that the panel density near the ship is higher than that in the far field. The border of the

artificial damping zone is shown in Figure 3.1 to specify the damped and undamped region. The convergence studies on panel number and domain size will be presented in the following chapter.

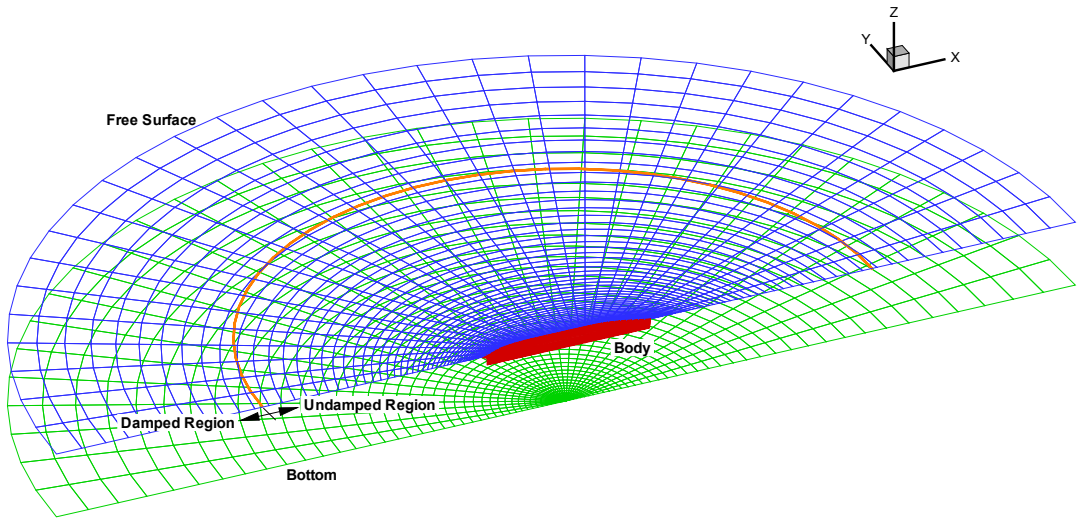

Figure 3.1: Typical oval-type computational domain for Series 60, Cb=0.7 (half).

Spatial Discretization of the Boundary Integral Equation

With the discretization of the computational domain and the approximation of unknowns using basis functions, the continuous boundary integral equation (2.70) for this boundary value problem is discretized at time t as follows,

$$2\pi(\phi^k)_j(t)B_{Pj}+(\phi^k)_j(t)\iint_S B_{Qj}\frac{\partial}{\partial n_Q}G(P;Q)dS_Q-(\frac{\partial\phi^k}{\partial n_Q})_j(t)\iint_S B_{Qj}G(P;Q)dS_Q=0, \tag{3.8}$$

where $P = 1, 2, ..., N$ is the field point located at the centroid of the panel with a total number of N, $B_{Pj} = B_j(P) = B_j(\vec{x}_P)$ and $B_{Qj} = B_j(Q) = B_j(\vec{x}_Q)$ are the j-th basis functions of vector $\vec{x}_P$ and $\vec{x}_Q$, respectively, j is the index for Einstein notation, which means a summation of the value of basis functions is made at each P and Q

over index j. The number of j varies with the order of basis functions. For the bi-quadratic basis function $B_j^{(2,2)}(\vec{x})$, $j = 1, 2, ..., 9$, while for the basis function with the lowest order $B_j^{(0,0)}(\vec{x})$, $j = 1$. ϕ^k denotes the velocity potential, where $k = 1$ for the radiation problem, $k = 2$ for the diffraction problem, and $k = 3$ for the free motion problem.

The free surface boundary conditions are also discretized spatially at time t as follows,

$$\frac{\partial(\zeta^k)_j(t)}{\partial t} B_{Pj} = (\frac{\partial \phi^k}{\partial z})_j(t) B_{Pj}, \tag{3.9}$$

$$\frac{\partial(\phi^k)_j(t)}{\partial t} B_{Pj} = -g(\zeta^k)_j(t) B_{Pj}, \tag{3.10}$$

where P is the field point on the free surface.

3.1.2 Temporal Discretization

The kinematic and dynamic free surface boundary conditions are discretized in time with the explicit Euler scheme at time $t = t_{n+1}$ respectively as follows,

$$\frac{(\zeta^k)_j^{n+1} - (\zeta^k)_j^n}{\Delta t} B_{Pj} = (\frac{\partial \phi^k}{\partial z})_j^n B_{Pj}, \tag{3.11}$$

$$\frac{(\phi^k)_j^{n+1} - (\phi^k)_j^n}{\Delta t} B_{Pj} = -g(\zeta^k)_j^{n+1} B_{Pj}. \tag{3.12}$$

The boundary integral equation is also discretized in time as follows,

$$2\pi(\phi^k)_j^{n+1} B_{Pj} + (\phi^k)_j^{n+1} \iint_S B_{Qj} \frac{\partial}{\partial n_Q} G(P;Q) dS_Q - (\frac{\partial \phi^k}{\partial n_Q})_j^{n+1} \iint_S B_{Qj} G(P;Q) dS_Q = 0, \tag{3.13}$$

where the superscript $n+1$ denotes the value of the unknowns at $(n+1)$-th time step, Δt is the time step. The kinematic free surface condition relates the wave elevation

at the $(n+1)$-th time step with the wave elevation and the normal velocity on the free surface at the n-th time step explicitly, through which the wave elevation at the $(n+1)$-th time step is integrated over Δt using the solution of normal velocity and wave elevation at the n-th time step. With the wave elevation updated at the $(n+1)$-th time step, the velocity potential on the free surface is then updated at the $(n+1)$-th time step through the dynamic free surface condition, which relates the velocity potential and wave elevation at the $(n+1)$-th time step with the wave potential at the n-th time step explicit. Then, at the $(n+1)$-th time step, the velocity potential ϕ^k on the free surface is known and the normal velocity $\frac{\partial \phi^k}{\partial z}$ is unknown; while on the submerged body surface, the normal velocity $\frac{\partial \phi^k}{\partial n}$ is known and the velocity potential ϕ^k is unknown. The discrete form of the boundary integral equation is a system of linear equations which relate the velocity potential ϕ^k and normal velocity $\frac{\partial \phi^k}{\partial n}$ (or $\frac{\partial \phi^k}{\partial z}$) on the free submerged body surface with those on the free surface at the $(n+1)$-th time step. The unknown velocity potential ϕ^k and the normal velocity $\frac{\partial \phi^k}{\partial z}$ are then solved simultaneously as the solution of the system of linear equations at the $(n+1)$-th time step. The collocation points for the system of linear equations are chosen to be at $P = 1, 2, ..., N$, which are the centroids of the panels.

Since the zero-order basis function is applied in this thesis, the discrete form of free surface boundary equations and boundary integral equations are degraded into,

$$\frac{(\zeta^k)^{n+1}(P) - (\zeta^k)^n(P)}{\Delta t} = (\frac{\partial \phi^k}{\partial z})^n(P), \tag{3.14}$$

$$\frac{(\phi^k)^{n+1}(P) - (\phi^k)^n(P)}{\Delta t} = -g(\zeta^k)^{n+1}(P), \tag{3.15}$$

$$2\pi(\phi^k)^{n+1}(P) + (\phi^k)^{n+1}(Q) \iint\limits_S \frac{\partial}{\partial n_Q} G(P;Q) dS_Q - (\frac{\partial \phi^k}{\partial n_Q})^{n+1}(Q) \iint\limits_S G(P;Q) dS_Q = 0, \tag{3.16}$$

where $S = S_B \cup S_F \cup S_{Bot}$, $P = 1, 2, ..., N$, $Q = 1, 2, ..., N$, $\iint_S G(P;Q)dS_Q(Q \neq P)$ and $\iint_S \frac{\partial}{\partial n_Q} G(P;Q)dS_Q(Q \neq P)$ are the influence coefficients from the integration of source and dipole over the boundaries, respectively. The calculation of the influence coefficients follows the analytical method in Newman (1986). When Q is coincident with $P(Q = P)$, $\iint_S G(P;Q)dS_Q = 2\pi$. For a computational domain with infinite depth, only the submerged body boundary S_B and free surface boundary S_F should be included in the boundary integral equation.

3.1.3 Radiation Condition on a Truncated Free Surface

For the boundary value problem with an infinite free surface, the radiation condition in the far field is automatically satisfied because the outgoing waves generated by the ship will not reflect back into the computational domain. However, in the Rankine panel method, the computational domain for the free surface has to be truncated. The truncated part of the free surface is acting as a rigid lid covering on the $z = 0$ plane, resulting in a reflection of the outgoing waves back to the computational domain at the domain edge (Sclavounos and Nakos, 1988). Since the radiation condition has to be satisfied, a numerical damping zone is used near the boundary of the truncated free surface to absorb the outgoing wave components to minimize the reflection. The concept of numerical beach was first proposed by Israeli and Orszag (1981). It functions like a physical wave absorbing beach in a wave basin or towing tank that absorbs the outgoing wave. The numerical scheme of the wave absorbing beach involves the use of Newtonian cooling term and the Rayleigh viscosity term, which are applied to the kinematic free surface condition within the damping zone. The linear kinematic free surface condition is modified as follows,

$$\frac{\partial \zeta^k}{\partial t} = \frac{\partial \phi^k}{\partial z} - 2\nu\zeta^k + \frac{\nu^2}{g}\phi^k, \tag{3.17}$$

where $-2\nu\zeta^k$ is the Newtonian cooling term that is proportional to the wave elevation with the damping strength $\nu > 0$, and $\frac{\nu^2}{g}\phi^k$ is the Rayleigh viscosity term. The damping is added through the cooling term which introduces an artificial mass flux through the free surface. However, the cooling term also changes the dispersion relation which causes a shift in wave frequency. The Rayleigh viscosity term is therefore introduced to eliminate this effect. The wave absorbing zone is distributed at the outer rim of the free surface. The distribution of cooling strength, ν, is an important issue for the numerical damping zone. If the cooling strength is constantly distributed over the damping zone, there will be an abrupt change of the free surface boundary condition at the inner edge of the zone, which may cause a wave reflection. Therefore, it is necessary for the cooling strength to vary along the radial distance over the damping zone to minimize the wave reflection. A quadratic tamper is applied to the cooling strength following the work of Israeli and Orszag (1981), with zero strength at the inner edge of the zone and the strength gradually increasing to the outer edge,

$$\nu(r^D) = 3\nu_0 \frac{(r^D - r_0^D)^2}{L^3}, \quad 0 \leq r^D - r_0^D \leq L, \tag{3.18}$$

where ν_0 is a constant, r^D is the radius of points in the damping zone on the truncated free surface, r_0^D is the radius where the damping zone starts, and L is the zone size.

3.1.4 Spatial Filtering for the Free Surface

In the present time-domain simulation, saw-tooth waves are found to emerge and grow on the free surface as time goes on and eventually spoil the entire solution. It is important to smooth the free surface by eliminating the saw-tooth waves to improve the stability of the simulation. In this thesis, the three-point low-pass filter proposed by Shao and Faltinsen (2012) is adopted to retain the growth of the saw-tooth waves

on the free surface with the form below,

$$\bar{\zeta}_j^k = c_F\zeta_{j-1}^k + (1-2c_F)\zeta_j^k + c_F\zeta_{j+1}^k \tag{3.19}$$

where ζ_j^k and $\bar{\zeta}_j^k$ are the wave elevations before and after smoothing, j is the numbering of the collocation points locally, and c_F is the strength of the filter. The filter is applied in the azimuth direction of the collocation points on the free surface every time step.

3.1.5 Time Integration of the Equations of Motion

The explicit Euler method is applied to the time integration of the equations of ship motion. The second order ordinary differential equation (ODE) (2.72) is decomposed into a system of linear equations.

$$\frac{d\vec{y}}{dt} = \vec{f}(t), \tag{3.20}$$

where

$$\vec{y}(t) = \begin{Bmatrix} \vec{y_1}(t) \\ \vec{y_2}(t) \end{Bmatrix} = \begin{Bmatrix} \dot{\vec{\xi}}(t) \\ \vec{\xi}(t) \end{Bmatrix}, \tag{3.21}$$

and

$$\vec{f}(t) = \begin{Bmatrix} \vec{f_1}(t) \\ \vec{f_2}(t) \end{Bmatrix} = \begin{Bmatrix} [\boldsymbol{M}]^{-1}(\boldsymbol{F}(t) - \boldsymbol{C}\vec{y_2}(t)) \\ \vec{y_1}(t) \end{Bmatrix}, \tag{3.22}$$

$\vec{\xi}$ is the vector of ship displacement in 6-DOF, $\boldsymbol{M}$ is the inertia matrix, $\boldsymbol{C}$ is the restoring coefficient matrix, and $\boldsymbol{F}(t)$ is the hydrodynamic force matrix at time t. The explicit Euler method is defined as follows,

$$\vec{y}_{n+1} = \vec{y}_n + h\vec{f}(t_n, \vec{y}_n), \tag{3.23}$$

where h is denotes the time step size Δt, the subscripts n and $n+1$ denote the value of variables at n-th and $(n+1)$-th time steps respectively.

3.2 Numerical Implementation

A time-domain program based on the numerical method above was written in Fortran, which is referred to as the present method. This version solves the linear time-domain ship motions with the ship freely floating in a finite water depth at zero speed undergoing incoming waves, in which case, the radiation and diffraction problems are solved simultaneously. It can also solve the forced motion of the ship, which corresponds to the radiation problem, and a fixed ship with the presence of incoming waves, which corresponds to the diffraction problem, separately.

Figure 3.2 shows the detailed work process of the program. The geometry of the ship (S_B) is read in from a geometry file. Then, the computational grids for the free surface (S_F) and bottom (S_{Bot}) are generated. For the linear problem, the incoming wave amplitude and the ship motion are assumed to be small. There will be no significant change in the value of influence coefficients. Therefore, for efficiency, the influence coefficients are calculated only once for the entire simulation. For each time step, the free surface boundary condition is solved explicitly to obtain the updated velocity potential and wave elevation on the free surface. Then, a mixed boundary integral equation is solved for the velocity potential on the body and bottom and the normal velocity on the free surface. The equations of ship motion are then solved after the calculation of the total forces acting on the body.

The solution of the mixed boundary integral equation involves the process of solving a dense system of linear equations $\boldsymbol{A}\boldsymbol{x}=\boldsymbol{b}$, where $\boldsymbol{A}$ is an N by N matrix consisting of influence coefficients with N being the total number of the panels on the boundaries,

$\boldsymbol{x}$ is the matrix of unknowns, and $\boldsymbol{b}$ is the known values from the previous time step. Since the influence coefficients will not change from time step to time step, the matrix $\boldsymbol{A}$ will also stay unchanged. The LU decomposition method is applied to obtain the inverse matrix $\boldsymbol{A^{-1}}$ of $\boldsymbol{A}$. Then, the inverse matrix is stored and used for each time step to solve for $\boldsymbol{x}$ with the updated $\boldsymbol{b}$ by simple multiplication $\boldsymbol{x}=\boldsymbol{A^{-1}b}$.

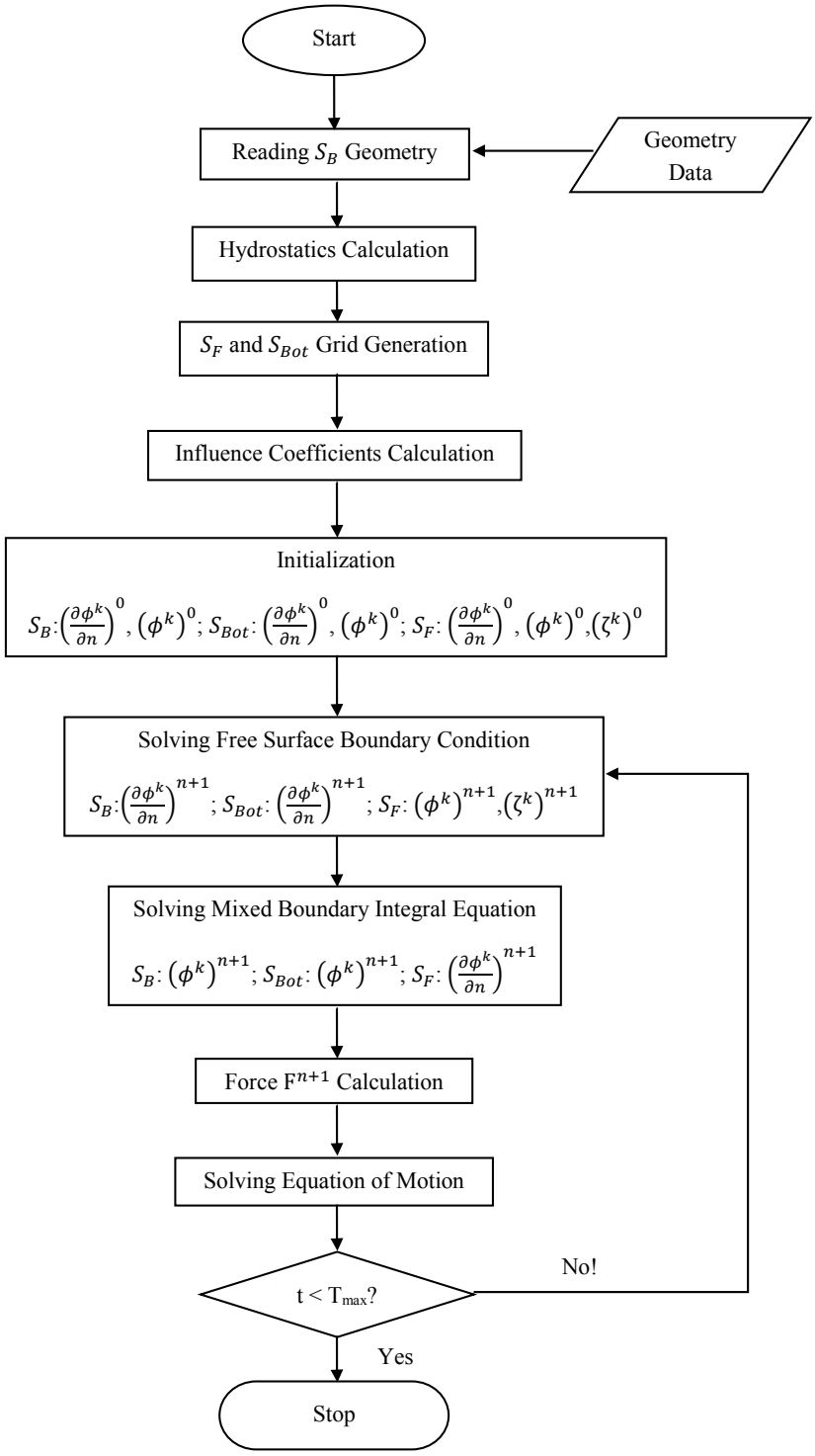

Figure 3.2: Flow chart for the present method program.

Chapter 4

Numerical Results

4.1 Solution Grids

The numerical method has been applied to various floating bodies including a truncated cylinder, a hemisphere, the Wigley I hull, a Series 60 ship, and the two-body side-by-side moored scenario.

It is important to chose a proper solution grid for the numerical computation since it may influence the computational result significantly. For the seakeeping problem at zero speed with incident waves, the disturbance waves due to the presence of the body and the body motion propagate circularly from the center of the fluid field to the far field. Thus, a circular computational domain is ideal for the present numerical computation and is adopted in all the computational cases.

Since the energy of the disturbed waves is more concentrated near the body than in the far field, a finer mesh is generated near the body on the free surface grid for a more accurate representation of the wave flow. The mesh far from the body is generated with less density for computational efficiency.

Only one set of solution grids is used for different wave frequencies for the cases of

the truncated cylinder, hemisphere, Wigley hull, and Series 60 ship. The size of the truncated free surface is determined by the longest wave length of the incident wave. The domain size should cover the longest wave length, which allows the longest wave to propagate and to be absorbed by the wave absorbing zone. The spacing size of the grid is determined by the shortest wave length. The spacing size near the body should be fine enough to allow the shortest wave to propagate. For the two-body side-by-side moored scenario, a number of computational grids with different domain sizes are used for different wave frequencies to improve the accuracy.

For a floating body which is symmetric along the $x - axis$ in head sea condition, the fluid field is also symmetric. For such a case, only half of the body and computational domain is needed for the computation, which is more efficient than using the entire domain.

Figure 4.1 shows the perspective view and top view of the oval-type grid for a hemisphere. Only half of the circular computational domain is shown. The spacing size of the grid increases exponentially from the body to the far field. The border of the artificial damping zone is shown in the top view.

Figure 4.2 shows half of the circular computation domain with the oval-type grid for the Wigley I hull in deep water.

Figure 4.3 shows the perspective view and the grid near the body of half of the circular computational domain with an oval-type grid for a Series 60, Cb=0.7 ship in a finite water depth. The bottom grid is generated to include the finite depth effect. The domain size of the bottom grid is the same as the free surface grid.

Figure 4.4 shows the perspective view and the grid near the body of half of the circular computational domain for the two-body side-by-side moored scenario. The rectangular grid is used for the gap portion of the free surface and the oval-type grid is used for the rest of the free surface.

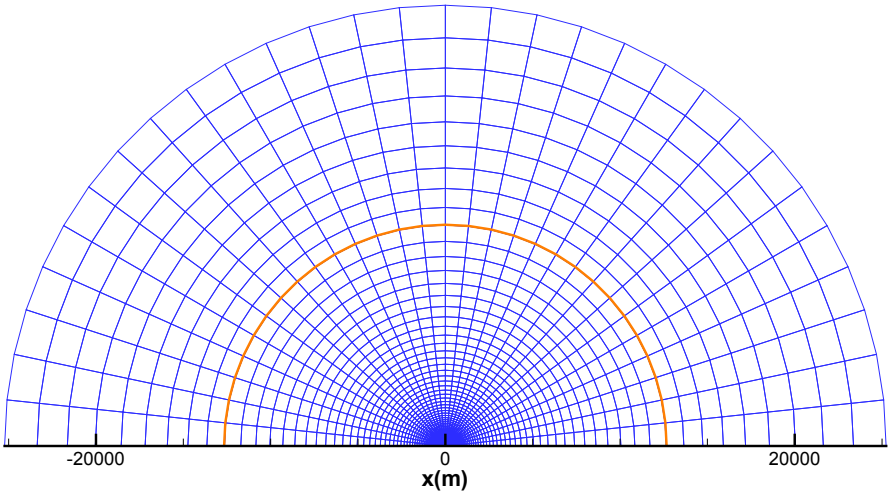

(a) Top view

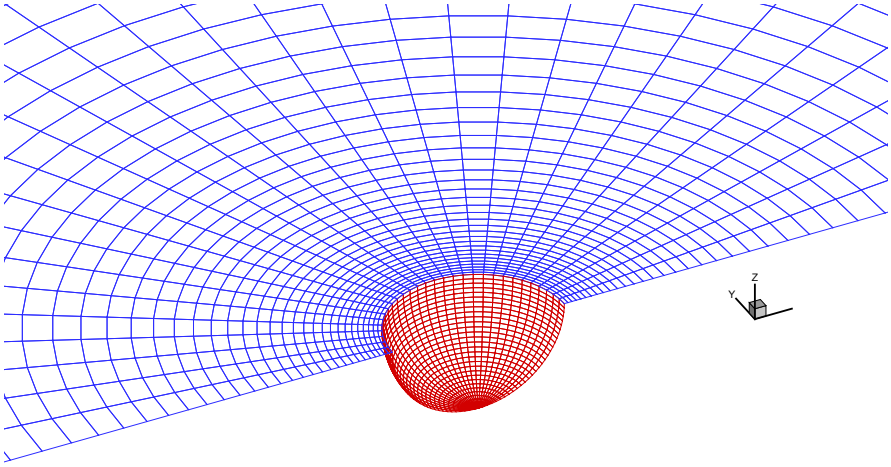

(b) Grid near the body

Figure 4.1: Oval-type grid for a hemisphere (half).

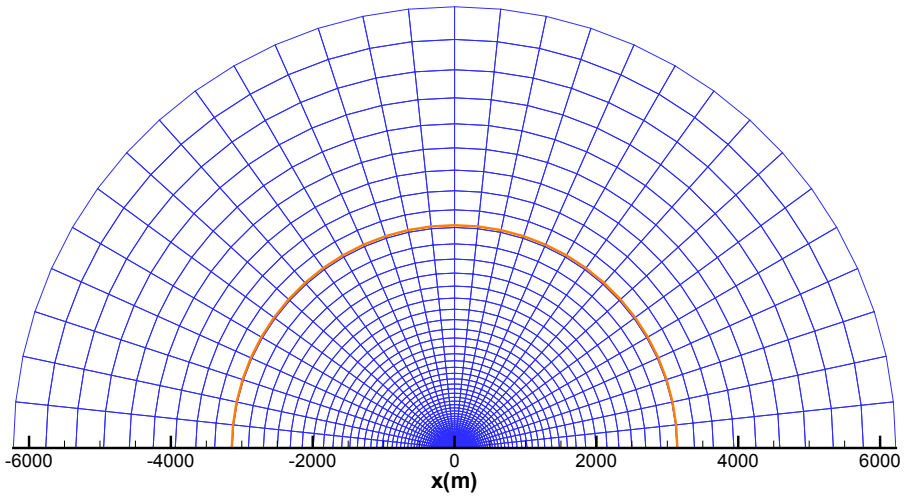

(a) Top view

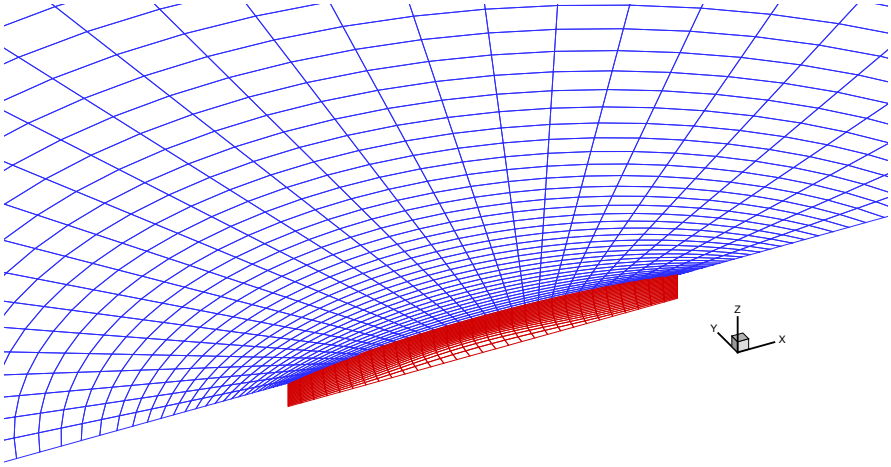

(b) Grid near the body

Figure 4.2: Oval-type grid for the Wigley I hull (half).

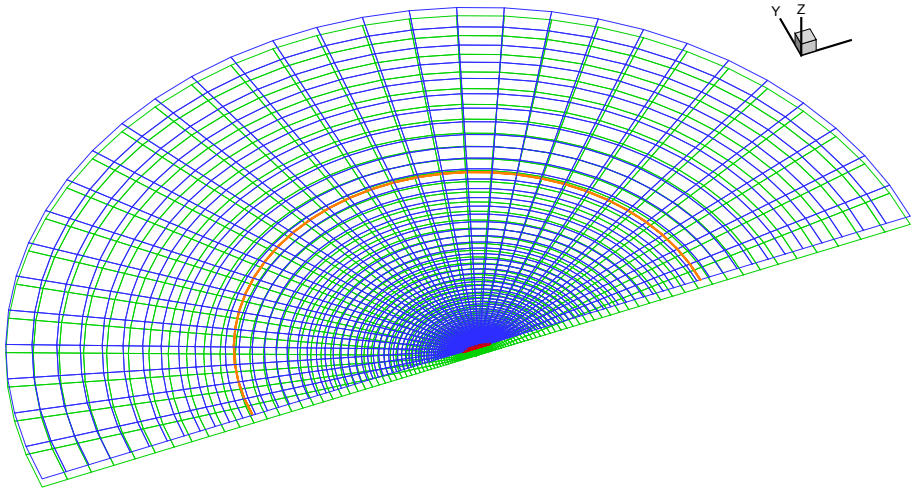

(a) Perspective view

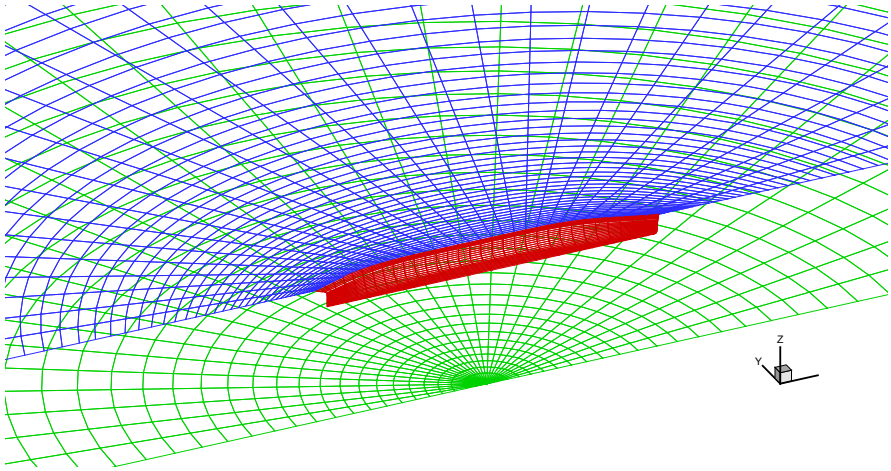

(b) Grid near the body

Figure 4.3: Oval-type grid for a Series 60, Cb=0.7 in finite water depth (half).

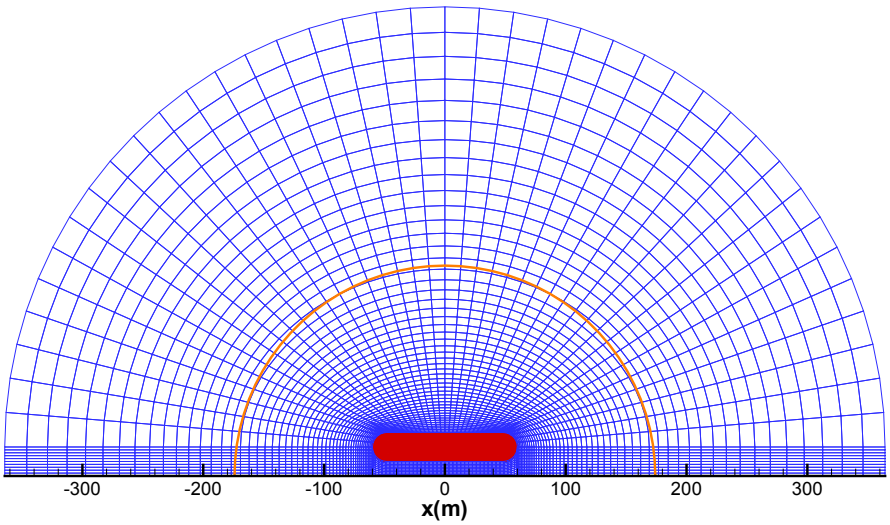

(a) Perspective view

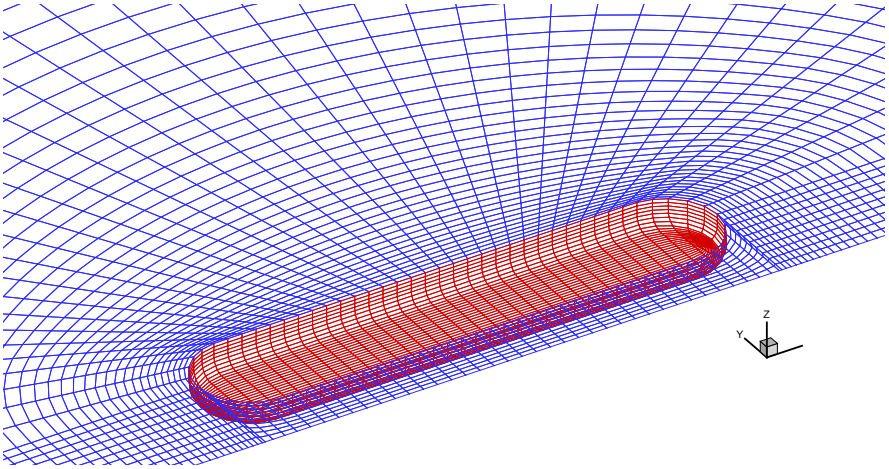

(b) Grid near the body

Figure 4.4: Computational grid for the two-body side-by-side moored scenario (half).

Table 4.1: Principal dimensions for different geometries.

Type of geometry	Length/Diameter(m)	Breadth/Diameter(m)	Draft(m)
Truncated cylinder	200	200	100
Hemisphere	200	200	100
Wigley I hull	120	12	7.5
S60, Cb=0.7 ship	102	14.3	5.72
Two-body side-by-side	120	24	6.0

Table 4.2: List of the number of panels for different geometries.

Type of geometry	Body surface	Free surface	Bottom surface	Total
Truncated cylinder	1,500	3,600	N/A	5,100
Hemisphere	900	2,400	N/A	3,300
Wigley I hull	600	2,400	N/A	3,000
S60, Cb=0.7 ship	682	2,480	1,860	5,022
Two-body side-by-side	1,600	3,400	N/A	5,000

Table 4.1 presents the principal dimensions for the geometries.

Table 4.2 listed the number of panels used for each geometry.

4.2 Forced Motion Simulations

In the forced motion time-domain simulation, the radiation problem, which corresponds to the forced oscillation of the body without incident waves, and the diffraction problem, which corresponds to the fixed body with the presence of only incident waves, are studied separately.

4.2.1 Wave Absorbing Zone

The wave absorbing zone is designed to absorb the outgoing waves in order to satisfy the radiation condition on the free surface. It is essential to examine the size of the damping zone L and the damping strength ν to ensure that the outgoing waves are absorbed properly. A quadratic tamper with damping constant ν_0 is applied to the

distribution of damping strength ν over the damping zone, which starts from r_0^D and ends at the edge of the computational domain r_{max}^D.

The parameters of the damping zone are tested by computing the flow around a single truncated cylinder of diameter $D(D = 2a)$ and draft d with $a/d = 1.0$ undergoing forced heave motion of radiant frequency ω which satisfies $Ka = 0.1$, where $K = \omega^2/g$. ξ_0 denotes the amplitude of forced heave motion. λ denotes the wavelength of the radiated wave.

The instantaneous wave elevations along the radial direction on the free surface with different damping constant ν_0 are compared with a Kim et al. (1997) in figure 4.5. Damping constant $\nu_0 = 20$ is not sufficient to absorb the outgoing waves at the boundary of the domain. The wave elevation at domain edge is still significant. There is a significant change in the phase of the outgoing wave. The instantaneous wave elevation ζ is in good agreement with Kim et al. (1997) for the whole range of r/D when damping constant $\nu_0 = 100$. However, when the damping constant $\nu_0 = 500$, the wave elevation near the domain edge is over damped, though it gives good agreement with Kim et al. (1997) from $r/D = 25$ to $r/D = 75$. $\nu_0 = 100$ is used and proven to be valid for all the computational cases in the present work. It may need to be tuned for other computational cases with different geometries and wave frequencies.

Figure 4.6 compares the instantaneous wave elevations for different sizes of damping zones. The results from the present method converged as the size of damping zone L increased. $L/\lambda = 2$ and $L/\lambda = 3$ both give good agreement with Kim et al. (1997).

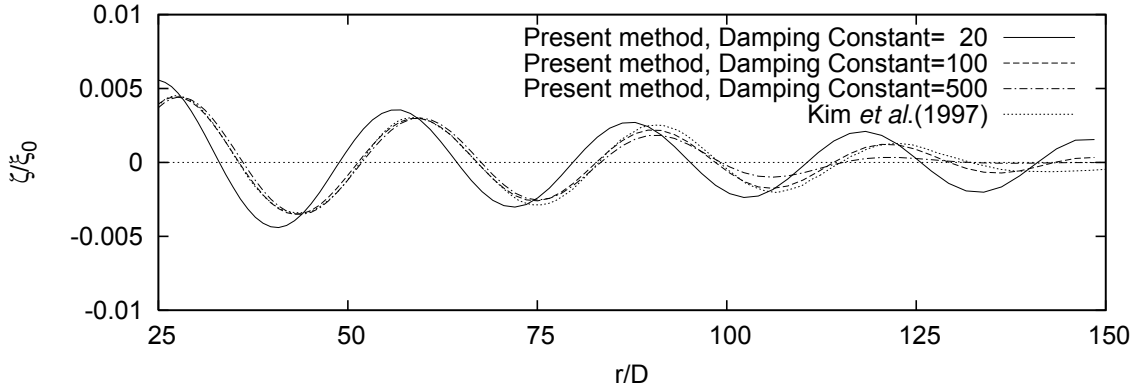

Figure 4.5: Comparison of instantaneous wave elevations for different damping constant, $L/\lambda = 3$, $Ka = 0.1$.

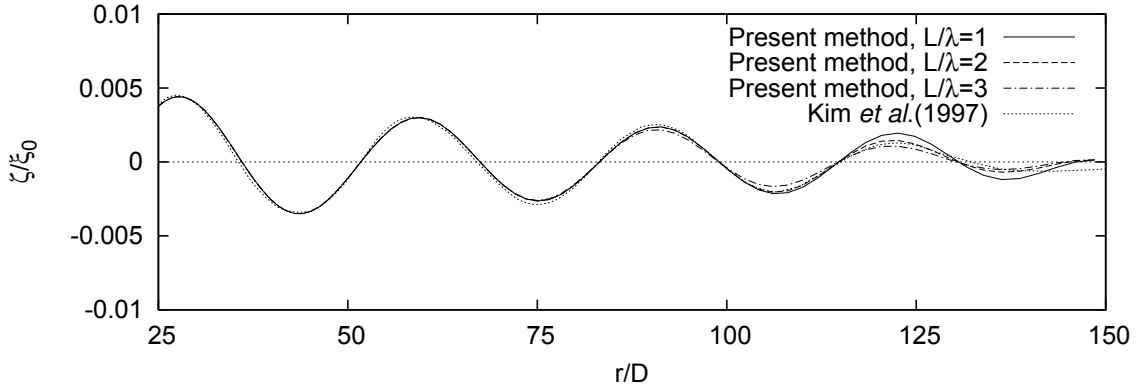

Figure 4.6: Comparison of instantaneous wave elevations for different sizes of damping zones, $\nu_0 = 100$, $Ka = 0.1$.

4.2.2 Radiation Problem

The radiation problem has been solved for a truncated cylinder, a hemisphere, the Wigley I hull, and a Series 60 ship in the time domain. For the radiation problem, The body is doing a forced simple harmonic motion about its equilibrium position ($z = 0$) without any incident wave. The radiated waves on the free surface propagate from the center to the outer rim of the computational domain and are then absorbed by the wave absorbing zone. The time series of hydrodynamic forces are calculated at each time step by the integration of the hydrodynamic pressure over the body surface. The added mass and damping coefficient associated with the radiation problem are then calculated.

The hydrodynamic forces due to the forced heave and surge motions of a hemisphere are calculated. Different domain sizes R_{max}, time step sizes Δt, filter strengths c_F, and number of panels on the free surface are used for the convergence studies which are carried out at $Ka = 0.1$ where a is the radius of the hemisphere, K is the wavenumber with $K = \omega^2/g$, and ω is the frequency of the forced harmonic motion.

Figure 4.7 shows the time series of heave force for different domain sizes R_{max}. λ is the wavelength of the radiated wave-induced by the forced harmonic motion. All time series are stable after the transient stage. The heave force converges as the domain size increases.

Figure 4.8 shows a good convergence of surge force as the number of panels on the free surface increases. Free surface panels of over 1500 is ideal for the simulations with the present method.

Figure 4.9 shows the temporal convergence of surge force. The surge force is studied at time step size Δt equals 1/100, 1/500, and 1/1000 of the period T of the forced harmonic motion. The time series of surge force is stable when the time step size is smaller than $1/500T$, which is ideal for the present method.

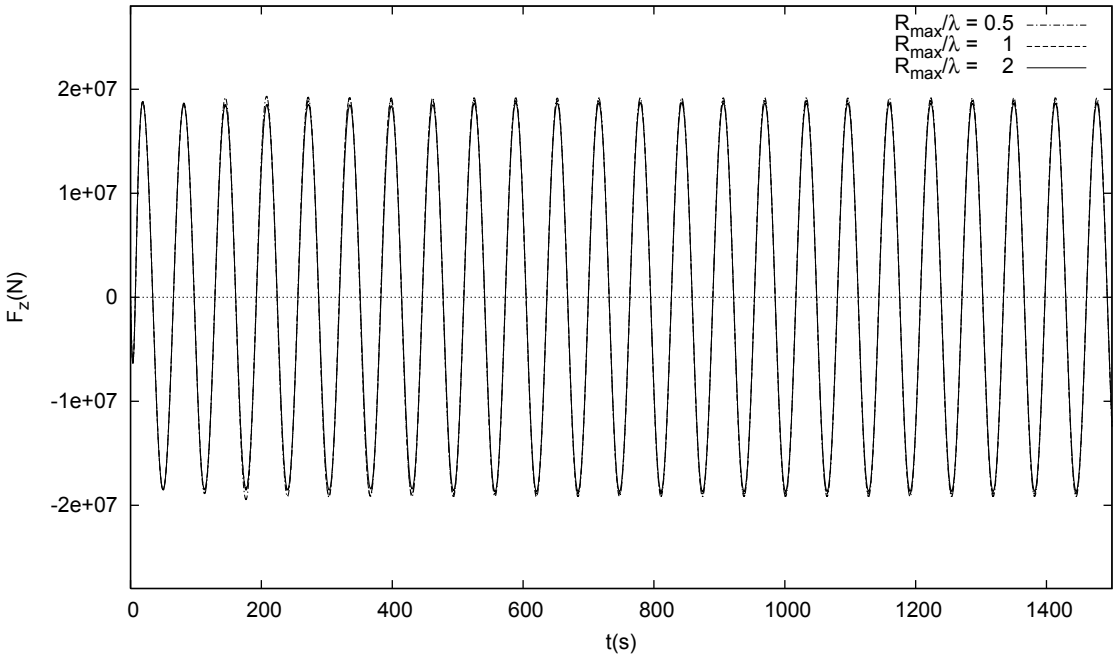

Figure 4.7: Comparison of the heave force of a hemisphere for different domain sizes, $Ka = 0.1$.

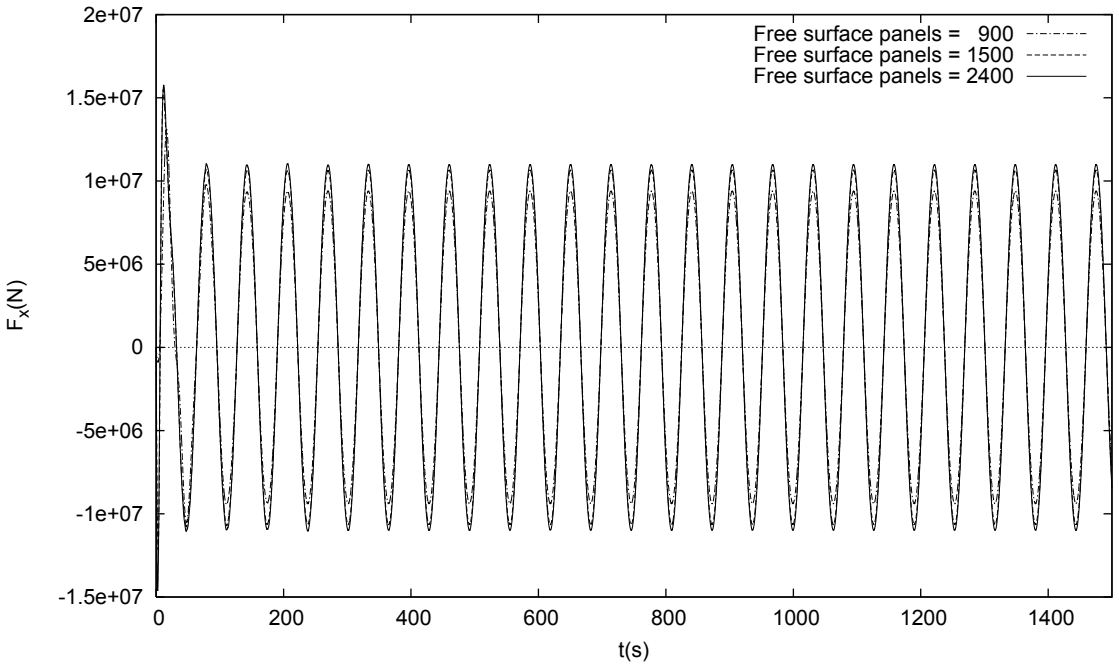

Figure 4.8: Comparison of the surge force of a hemisphere for different number of panels on the free surface, $Ka = 0.1$.

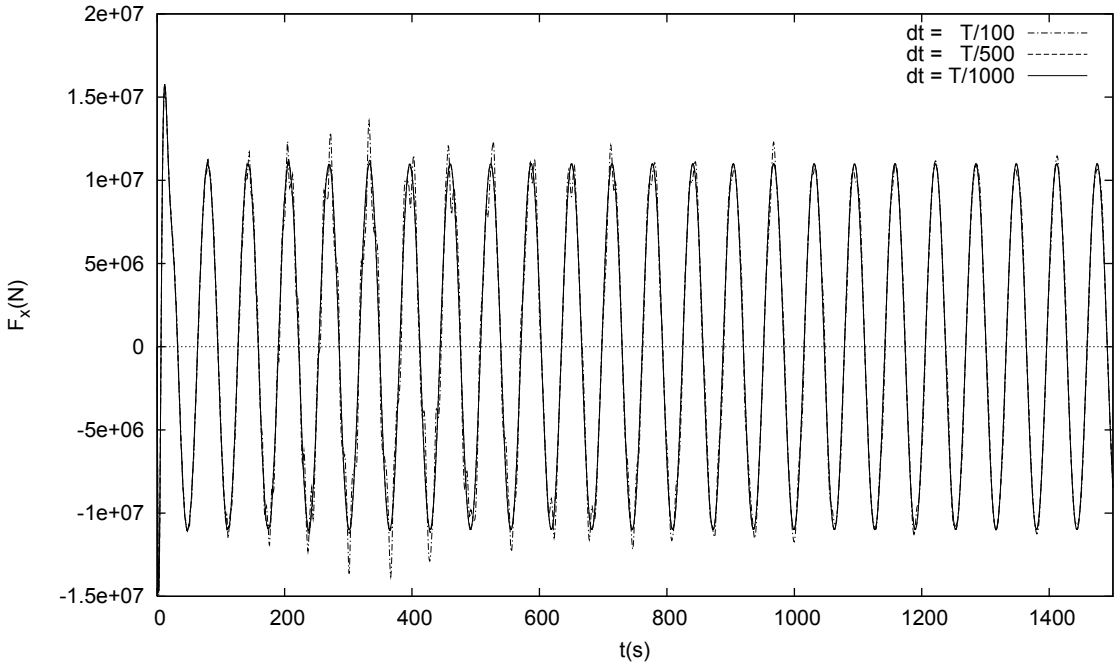

Figure 4.9: Comparison of the surge force of a hemisphere for different time step sizes, $Ka = 0.1$.

Figure 4.10 shows that the numerical filter is important for the stability of the time series of surge force. The surge force converges when the filter strength is larger than 0.001.

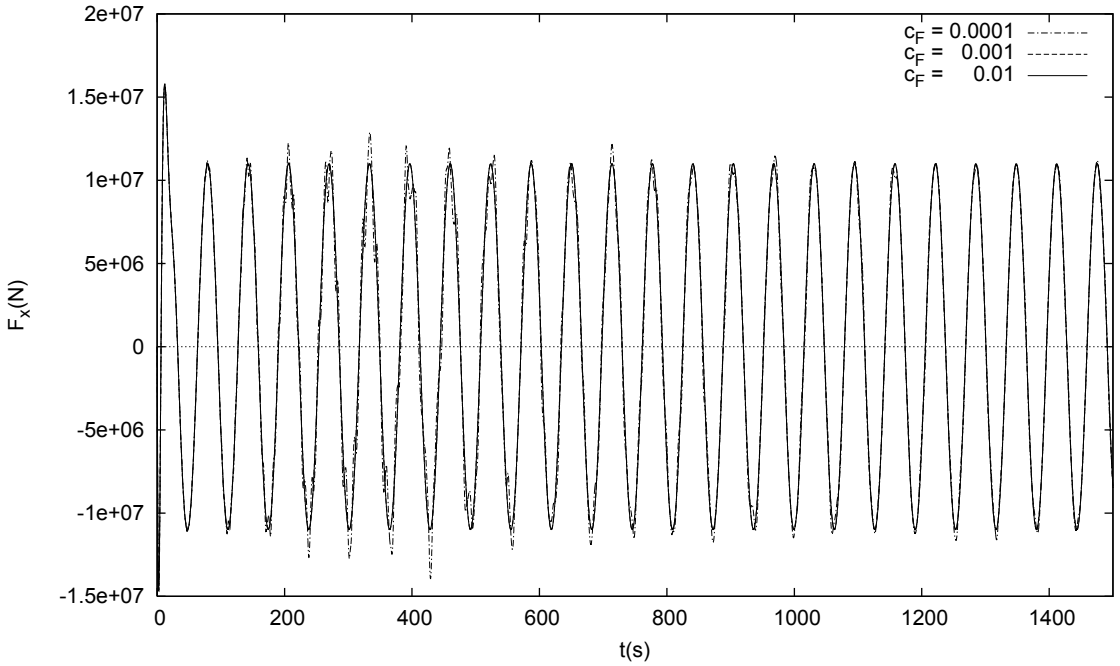

Figure 4.10: Comparison of the surge force of a hemisphere for different filter strengths, $Ka = 0.1$.

The added mass and damping coefficients of surge and heave motions of the hemisphere are extracted from the converged time series of hydrodynamic forces at different Ka. Table 4.3 and 4.4 show a comparison of the present numerical results with analytical solutions by Hulme (1982). Both non-dimensional surge added mass and damping from the present method are in good agreement with the analytical solutions by Hulme (1982). For the forced heave motion, there is some discrepancy in the non-dimensional damping parameter at higher Ka values where the absolute values of damping are small. The results listed in the tables are also plotted in Figure 4.11 and 4.12.

Table 4.3: The surge added mass and damping coefficient for a hemisphere.

Ka	$A_{11}/(\rho\nabla)$		$B_{11}/(\rho\nabla\omega)$	
	Analytical(Hulme)	Present method	Analytical(Hulme)	Present method
0.1	0.5223	0.5230	0.0011	0.0033
0.2	0.5515	0.5522	0.0082	0.0104
0.3	0.5848	0.5855	0.0255	0.0258
0.4	0.6175	0.6179	0.0557	0.0584
0.5	0.6439	0.6440	0.0987	0.1020
0.6	0.6586	0.6592	0.1516	0.1517
0.7	0.6582	0.6587	0.2092	0.2095
0.8	0.6421	0.6415	0.2653	0.2681
0.9	0.6127	0.6121	0.3145	0.3167
1.0	0.5740	0.5740	0.3535	0.3542
1.2	0.4860	0.4867	0.3978	0.3975
1.4	0.4038	0.4026	0.4061	0.4077
1.6	0.3371	0.3376	0.3929	0.3928
1.8	0.2865	0.2867	0.3695	0.3696
2.0	0.2493	0.2491	0.3424	0.3429
2.5	0.1951	0.1960	0.2769	0.2770
3.0	0.1720	0.1735	0.2237	0.2237
3.5	0.1634	0.1653	0.1826	0.1828
4.0	0.1620	0.1638	0.1511	0.1519
4.5	0.1641	0.1663	0.1266	0.1273
5.0	0.1679	0.1703	0.1073	0.1081
6.0	0.1772	0.1798	0.0794	0.0805
7.0	0.1865	0.1889	0.0608	0.0627
8.0	0.1949	0.1975	0.0479	0.0494
9.0	0.2022	0.2047	0.0386	0.0404
10.0	0.2085	0.2107	0.0317	0.0347

Table 4.4: The heave added mass and damping coefficient for a hemisphere.

Ka	$A_{33}/(\rho\nabla)$		$B_{33}/(\rho\nabla\omega)$	
	Analytical(Hulme)	Present method	Analytical(Hulme)	Present method
0.1	0.8627	0.8610	0.1816	0.1868
0.2	0.7938	0.7933	0.2793	0.2800
0.3	0.7157	0.7153	0.3254	0.3258
0.4	0.6452	0.6437	0.3410	0.3434
0.5	0.5861	0.5848	0.3391	0.3409
0.6	0.5381	0.5378	0.3271	0.3273
0.7	0.4999	0.4984	0.3098	0.3119
0.8	0.4698	0.4697	0.2899	0.2899
0.9	0.4464	0.4452	0.2691	0.2709
1.0	0.4284	0.4278	0.2484	0.2494
1.2	0.4047	0.4035	0.2096	0.2120
1.4	0.3924	0.3924	0.1756	0.1757
1.6	0.3871	0.3870	0.1469	0.1476
1.8	0.3864	0.3858	0.1229	0.1253
2.0	0.3884	0.3881	0.1031	0.1049
2.5	0.3988	0.3988	0.0674	0.0683
3.0	0.4111	0.4110	0.0452	0.0467
4.0	0.4322	0.4320	0.0219	0.0245
5.0	0.4471	0.4469	0.0116	0.0140
6.0	0.4574	0.4571	0.0066	0.0086
7.0	0.4647	0.4643	0.0040	0.0058
8.0	0.4700	0.4696	0.0026	0.0030
9.0	0.4740	0.4736	0.0017	0.0030
10.0	0.4771	0.4767	0.0012	0.0030

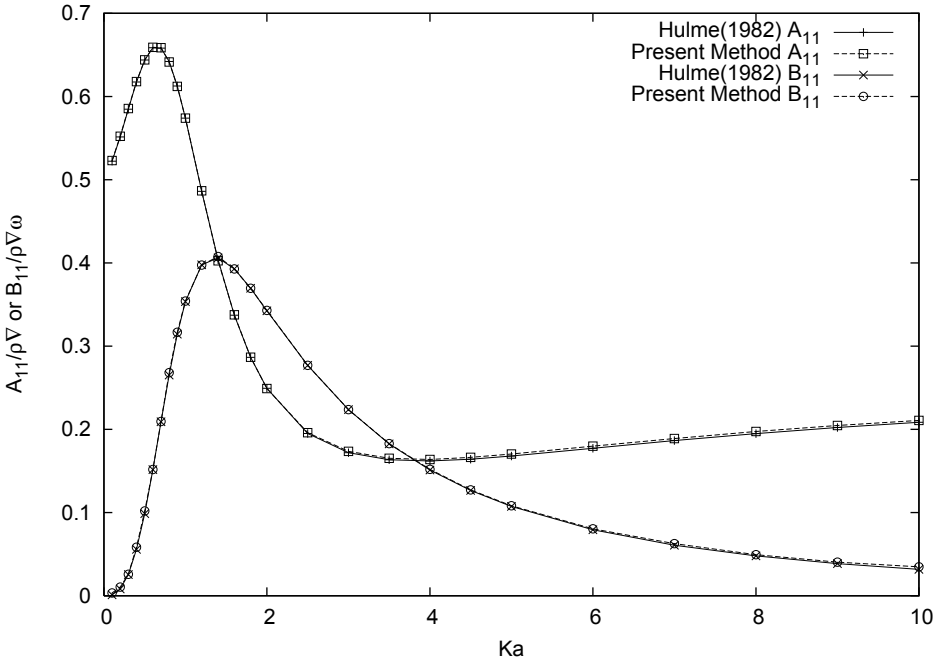

Figure 4.11: The surge added mass and damping coefficient of a hemisphere.

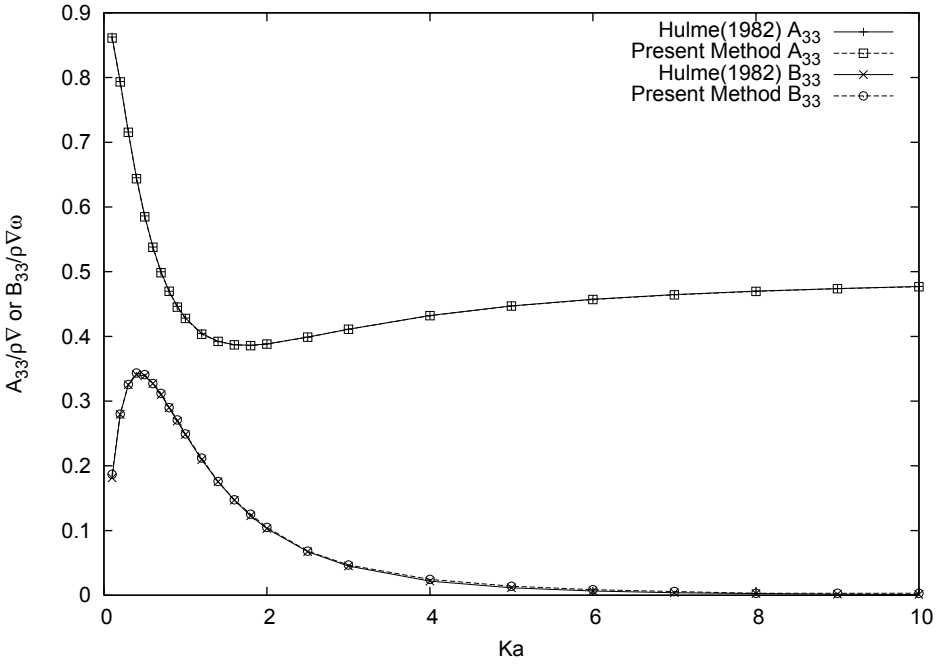

Figure 4.12: The heave added mass and damping coefficient of a hemisphere.

The radiation problem of the Wigley I hull is studied through forced heave and pitch harmonic motions at a wide range of frequencies with motion amplitudes of ξ_0. Figure 4.13 and 4.14 present the instantaneous wave contours of the radiated wave induced by the forced heave and pitch motions, respectively, where ζ denotes the free surface wave elevation. The values in the contour are non-dimensionalized as m/m for heave motion and m/rad for pitch motion. The heave and pitch added mass and damping coefficients of the Wigley I hull in deep water are calculated and compared with numerical results from the frequency-domain programs WAMIT and MAPS0. Figure 4.15 to 4.18 present the added mass and damping for both heave and pitch motions. The results from the present method are in good agreement with numerical results from WAMIT and MAPS0.

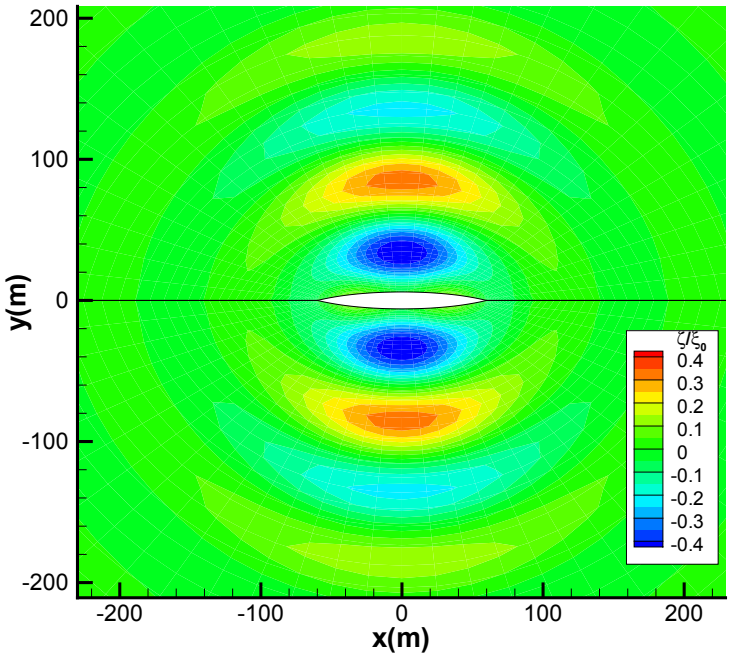

Figure 4.13: Instantaneous radiated wave contour around the Wigley I hull with forced heave motion, $\omega = 0.8$rad/s.

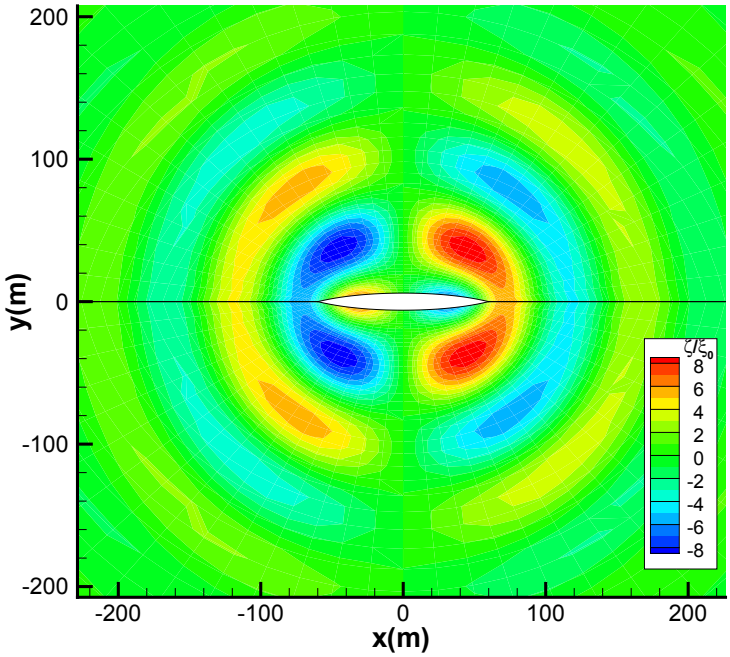

Figure 4.14: Instantaneous radiated wave contour around the Wigley I hull with forced pitch motion, $\omega = 0.8$rad/s.

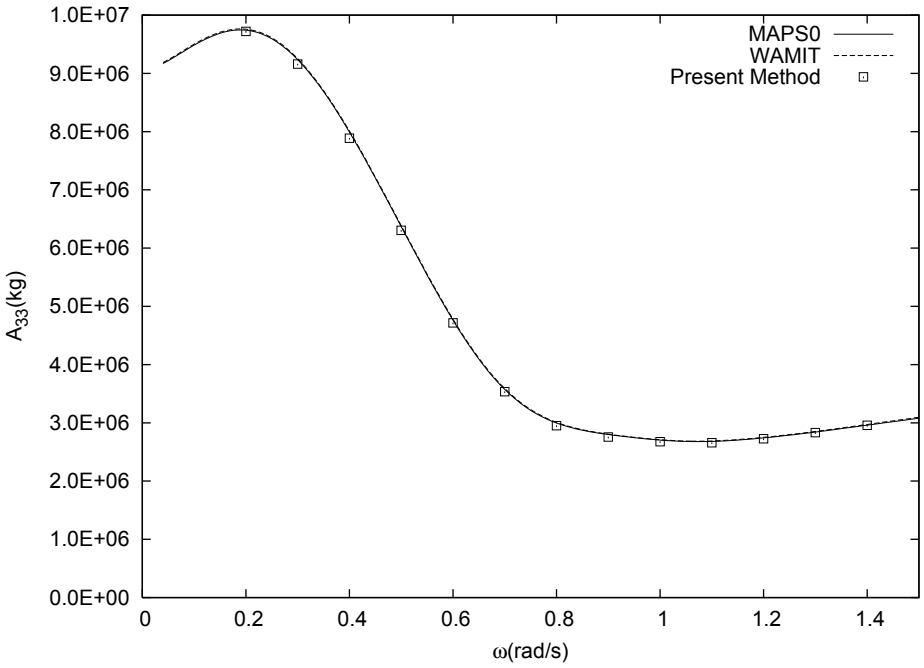

Figure 4.15: Comparison of the heave added mass of the Wigley I hull.

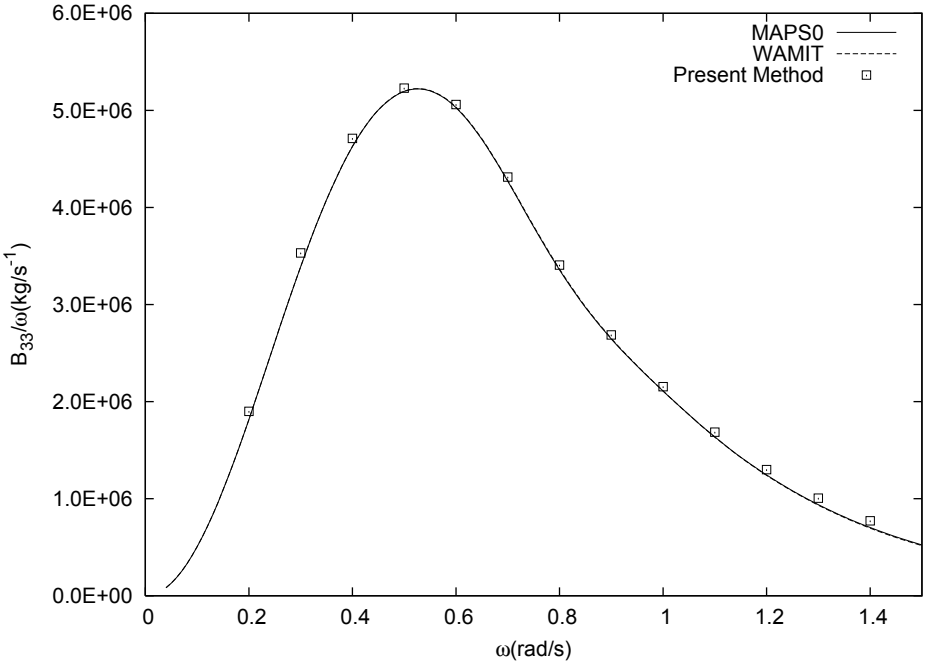

Figure 4.16: Comparison of the heave damping of the Wigley I hull.

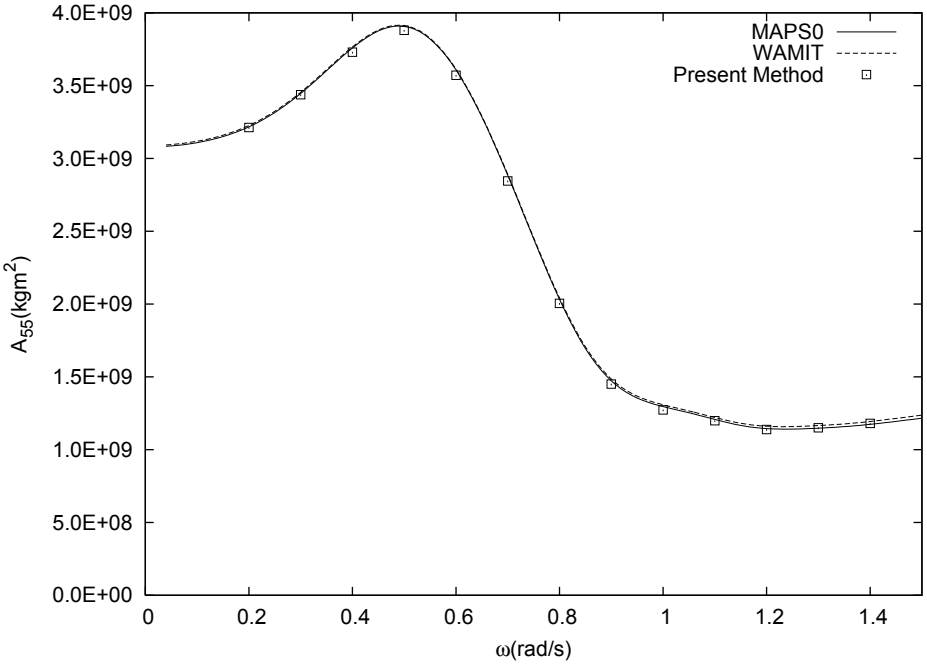

Figure 4.17: Comparison of the pitch added mass of the Wigley I hull.

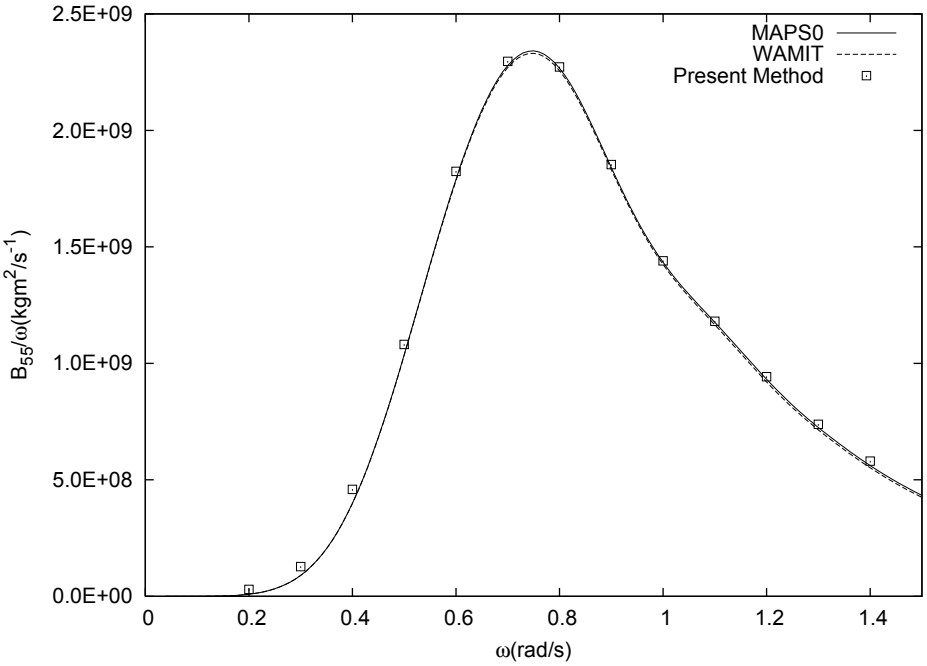

Figure 4.18: Comparison of the pitch damping of the Wigley I hull.

For vessels and floating structures in finite water depth h, the solution grid is distributed on the bottom of the computational domain with $z = -h$. The forced heave and pitch motion simulations are carried out for a Series 60, Cb=0.7 ship at a series of forced motion frequencies with a 40m water depth. Since the linear free surface boundary conditions are used for the present method, the water depth is restricted to 40m for radiated waves of $\omega = 0.4$rad/s to remain as linear waves. The time series of hydrodynamic forces are first calculated, through which the added mass and damping coefficients are obtained and compared with numerical results from MAPS0 and WAMIT.

Various numbers of panels on the bottom are used in the convergence studies. Figure 4.19 and 4.20 illustrate the convergence of the heave radiation force and pitch radiation moment for the Series 60, Cb=0.7 ship at $\omega = 0.4$rad/s. Both the heave force and pitch moment converge as the number of panels on the bottom surface increases.

Figure 4.21 to 4.24 show the comparisons of added mass and damping coefficients of

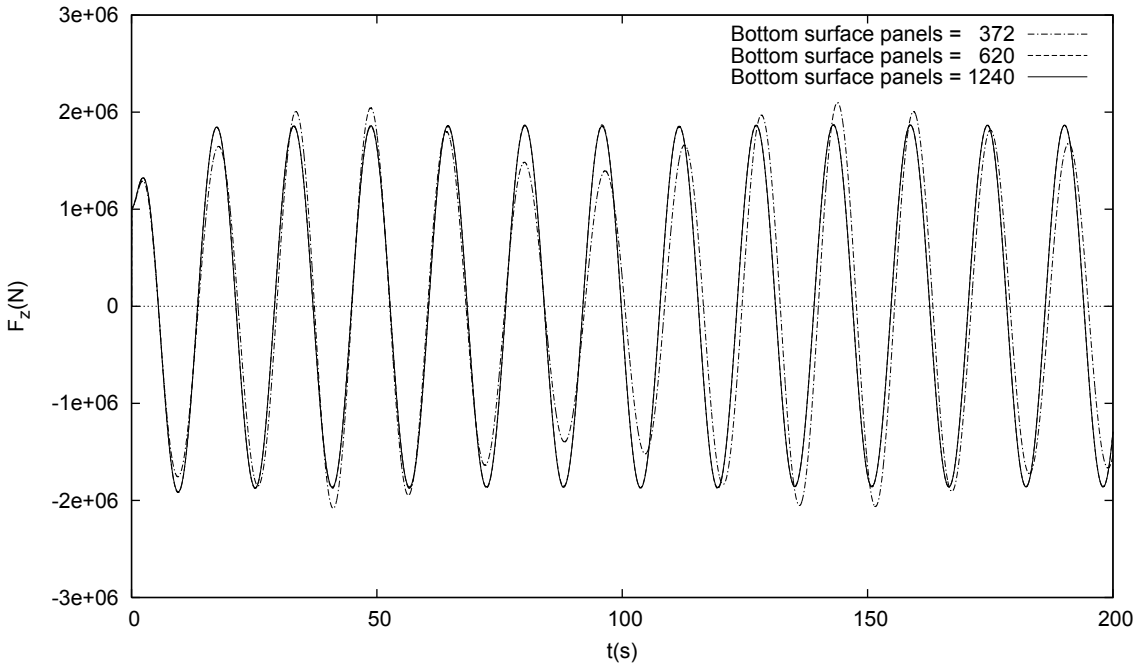

Figure 4.19: Comparison of the heave force of a Series 60, Cb=0.7 ship with a forced heave motion for different number of panels on the bottom surface, $\omega = 0.4$rad/s.

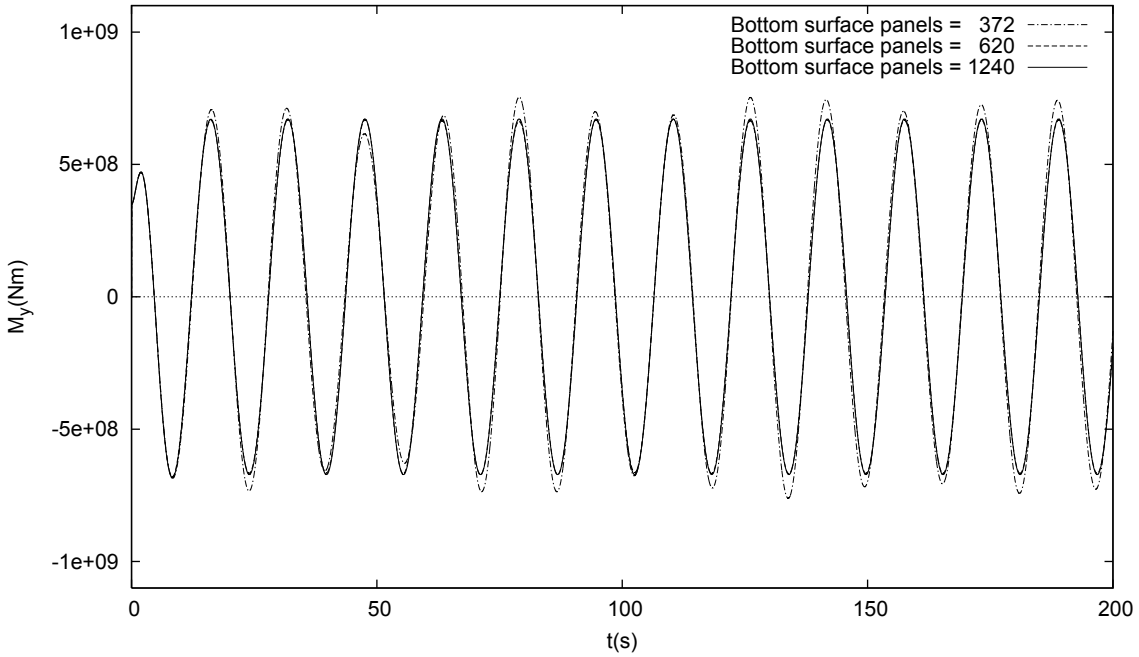

Figure 4.20: Comparison of the pitch moment of a Series 60, Cb=0.7 ship with a forced pitch motion for different number of panels on the bottom surface, $\omega = 0.4$rad/s.

Series 60, Cb=0.7 ship with the numerical results from MAPS0 and WAMIT at water depth $h = 40$m. The A_{33}, B_{33}, A_{55}, and B_{55} computed with present method are in good agreement with results from MAPS0 and WAMIT.

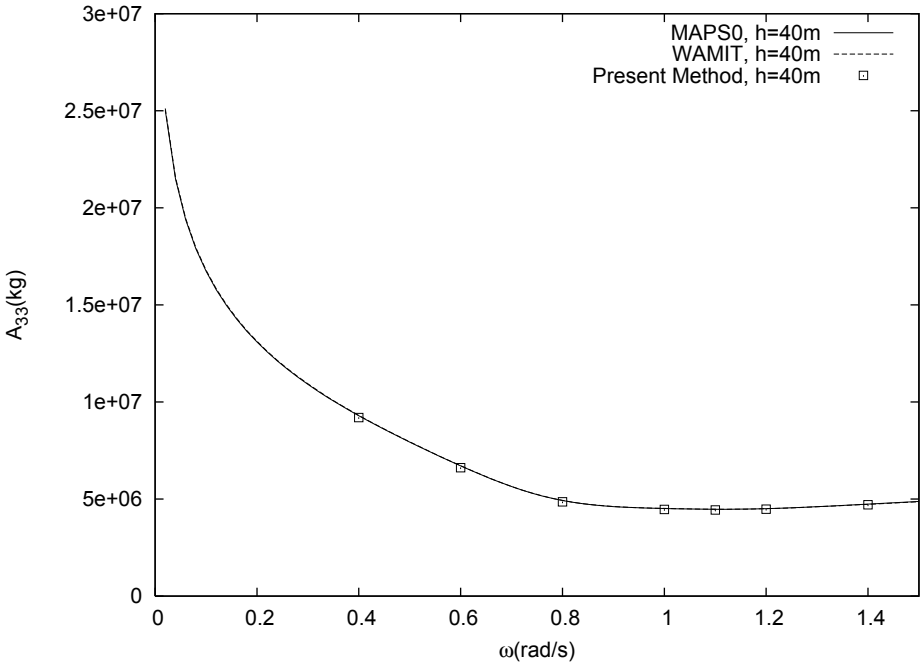

Figure 4.21: Comparison of the heave added mass of a Series 60, Cb=0.7 ship, $h = 40$m.

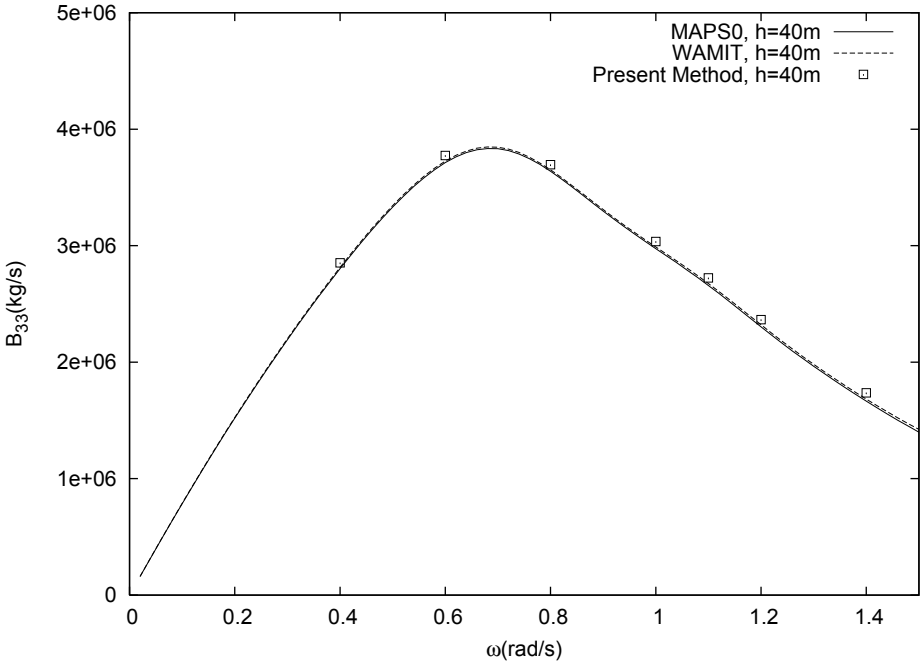

Figure 4.22: Comparison of the heave damping of a Series 60, Cb=0.7 ship, $h = 40$m.

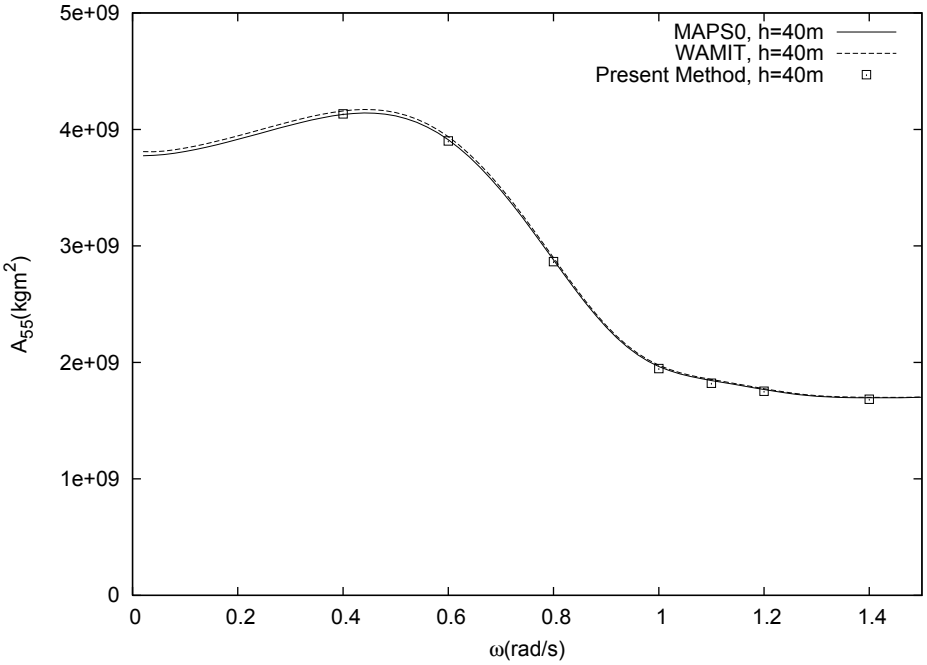

Figure 4.23: Comparison of the pitch added mass of a Series 60, Cb=0.7 ship, $h = 40$m.

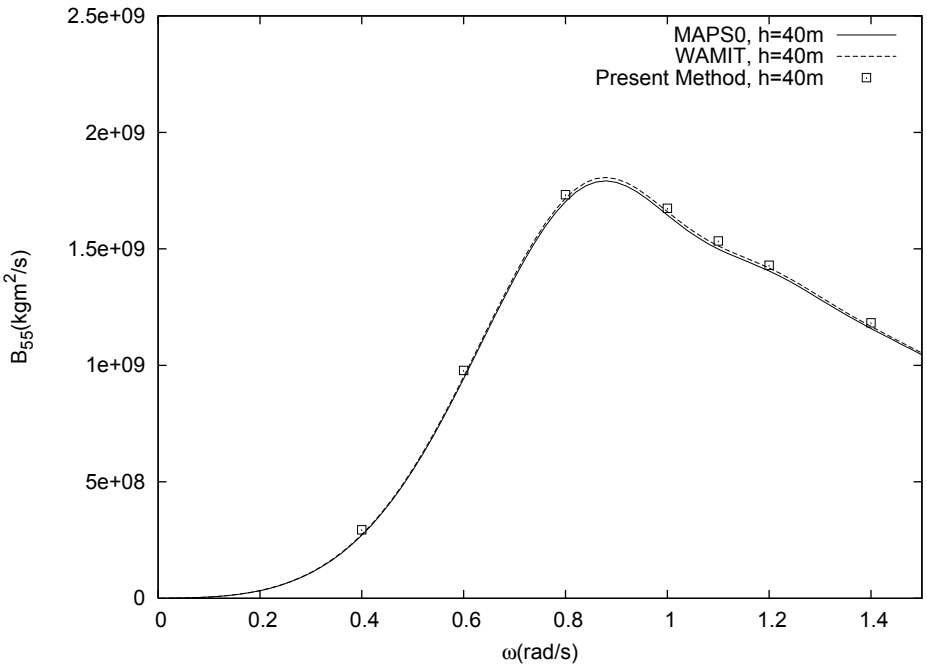

Figure 4.24: Comparison of the pitch damping of a Series 60, Cb=0.7 ship, $h = 40$m.

4.2.3 Diffraction Problem

The diffraction problem has been solved for a truncated cylinder, the Wigley I hull, the Series 60, Cb=0.7 ship, and the two-body side-by-side moored scenario in the time domain. For the diffraction problem the body is fixed in its equilibrium position undergoing incoming sinusoidal incident waves. The wave exciting force acting on the body associated with the diffraction problem includes the Froude–Krylov force, which is due to the dynamic wave pressure from the undisturbed incident wave, and the diffraction force, which is due to the change in diffracted wave potential over time. In this thesis, the incident wave potentials are calculated at each centroid of the panels on the body surface. The wave exciting forces are obtained at each time step by the direct integration of hydrodynamic pressure, which is proportional to the time derivative of incident wave and diffracted wave potentials, over the mean wetted body surface.

The wave exciting forces are calculated for a fixed truncated cylinder of diameter D and draft d with $D/d = 2/3$. The amplitude of the incident wave is A_I, which is half of the incident wave height H. Figure 4.25 shows the comparison of time history for the non-dimensional horizontal force acting on the cylinder calculated by the present method with that of Kim (1999). The calculated horizontal force is in good agreement with the result of Kim (1999). The calculation starts from $t = 0$ and after a transient period (from non-dimensional time 0.0 to 5.0) the solution is stable.

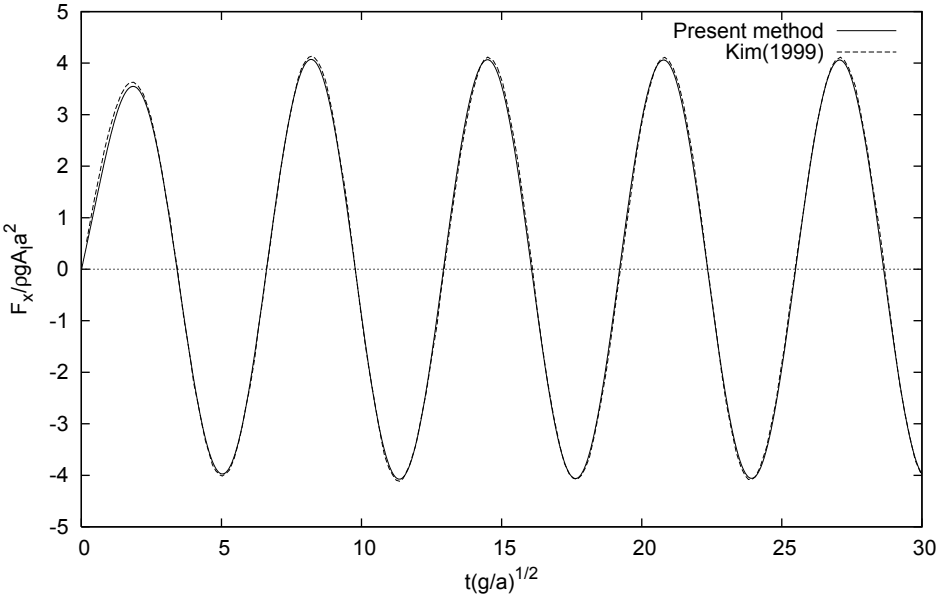

Figure 4.25: Horizontal force acting on a truncated cylinder, $Ka = 0.1$.

The wave exciting forces are calculated for the Wigley I hull at different wave frequencies in head sea condition in deep water. Different time step sizes Δt and different number of panels on the free surface are used in the convergence studies, which are carried out at incident wave frequency $\omega = 1.0$rad/s. Figure 4.26 and 4.27 illustrate the convergence of the heave exciting force and pitch exciting moment of the Wigley I hull for different number of panels on the free surface. The results are stable after the transient stage. Both the exciting force and moment converge as the number of panels on the free surface increases. Figure 4.28 and 4.29 show the temporal convergence

of the exciting force and moment. The convergence is reached very quickly for both results.

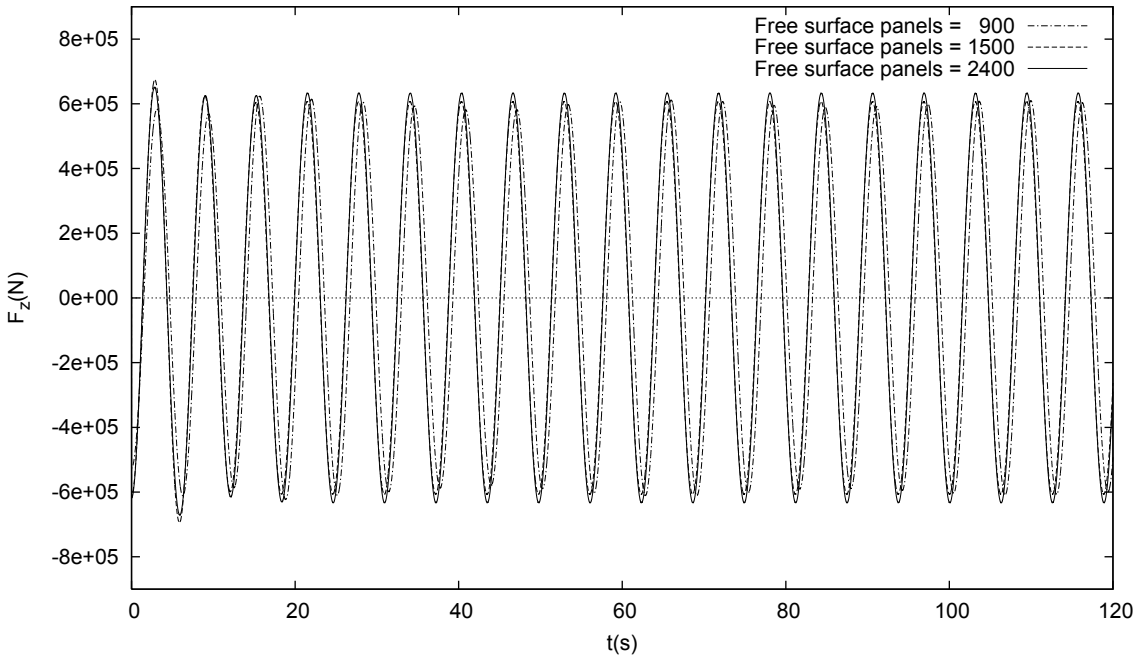

Figure 4.26: Comparison of the heave exciting force of the Wigley I hull for different number of panels on the free surface, $\omega = 1.0$rad/s.

Figure 4.30 illustrates the diffracted wave around the Wigley I hull at an incident wave frequency $\omega = 0.8$rad/s. The wave elevation in the contour is non-dimensionalized as m/m.

The wave exciting force RAOs are extracted from the converged time series of exciting forces and compared with the numerical results from MAPS0 and WAMIT. Figure 4.31 and 4.32 show that the RAOs of the heave wave exciting force and pitch wave exciting moment acting on the Wigley I hull at selected frequencies agrees very well with the numerical results from MAPS0 and WAMIT.

For the diffraction problem in a finite water depth, the convergence study is carried out for the Series 60, Cb=0.7 ship in a 40m water depth using different number of panels on the bottom surface. Figure 4.33 and 4.34 illustrate good convergence

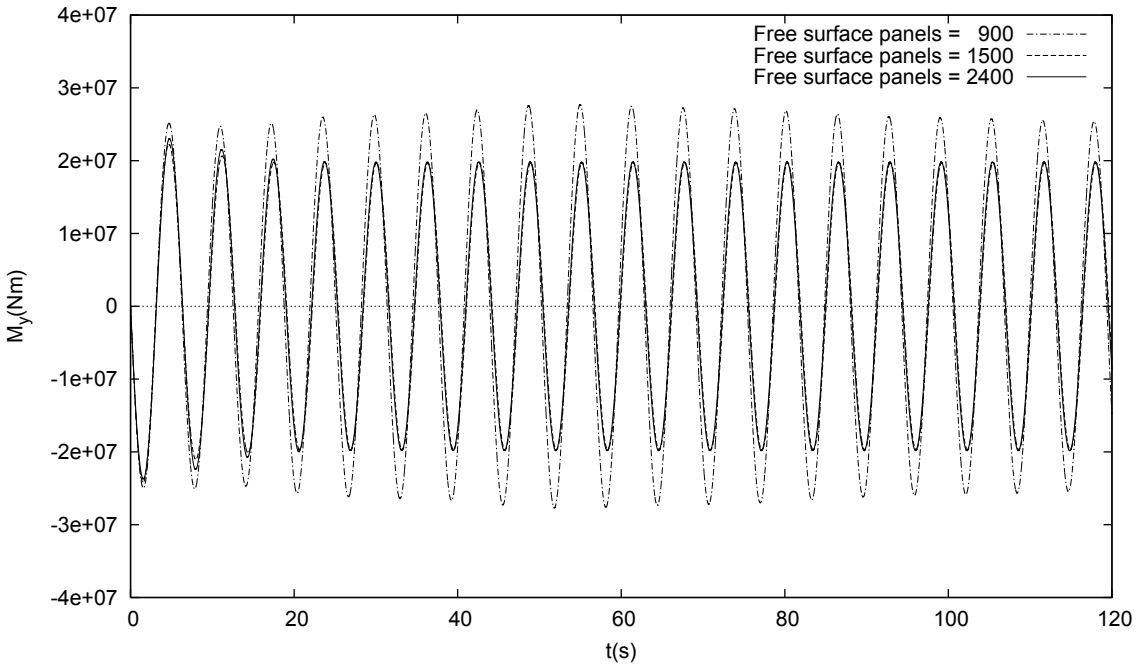

Figure 4.27: Comparison of the pitch exciting moment of the Wigley I hull for different number of panels on the free surface, $\omega = 1.0$rad/s.

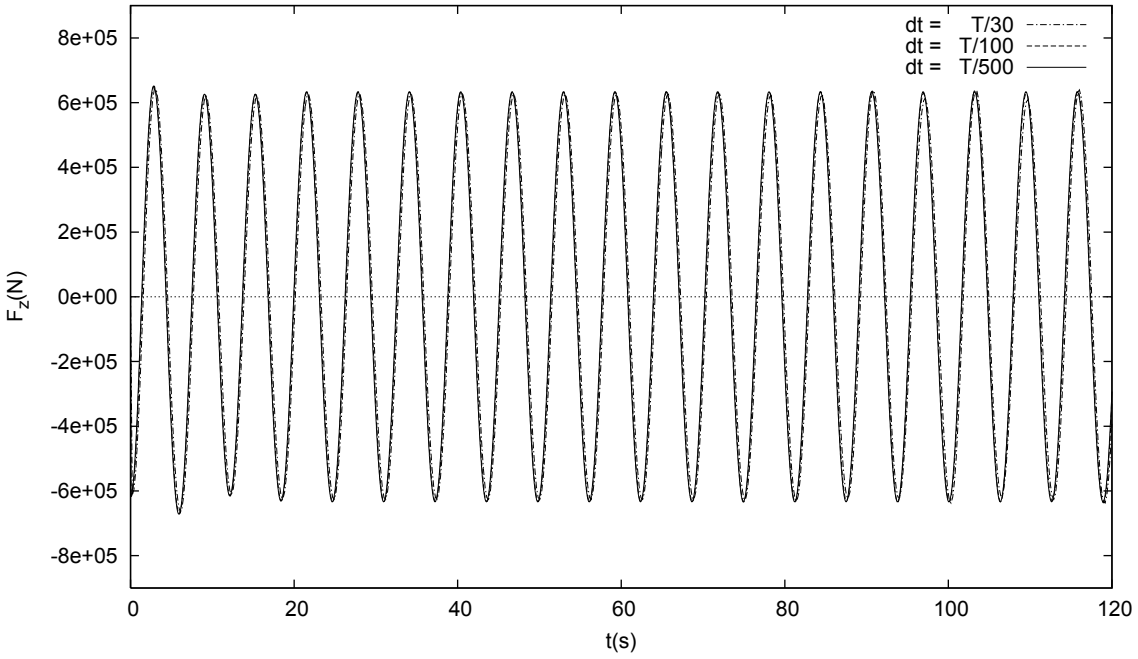

Figure 4.28: Comparison of the heave exciting force of the Wigley I hull for different time step sizes, $\omega = 1.0$rad/s.

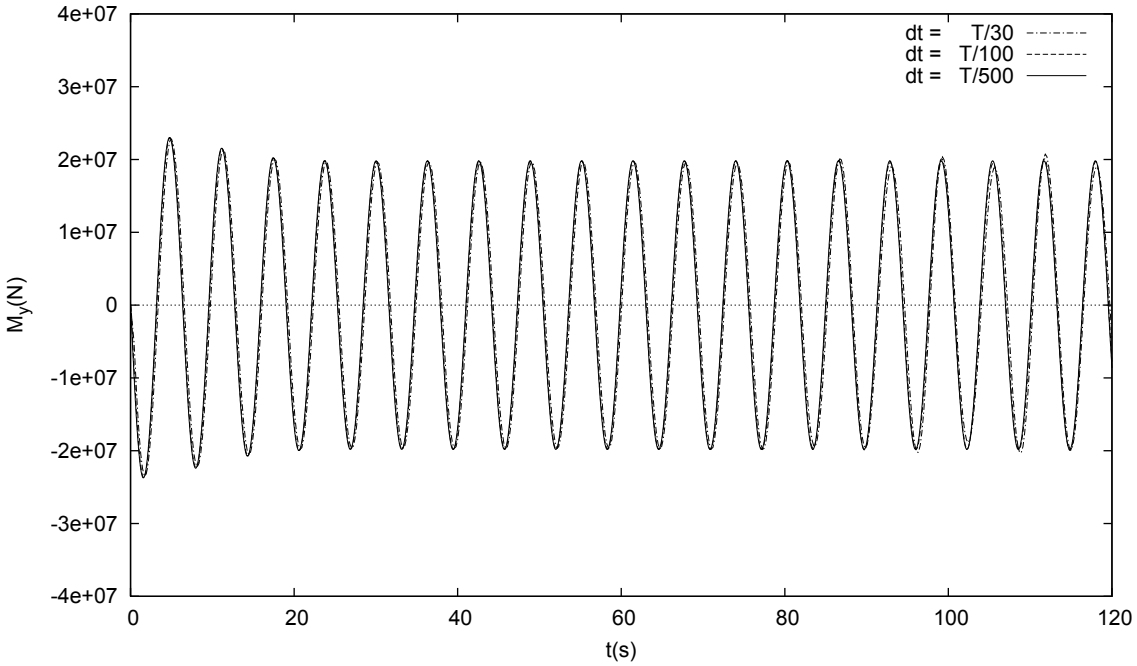

Figure 4.29: Comparison of the pitch exciting moment of the Wigley I hull for different time step sizes, $\omega = 1.0$rad/s.

of heave exciting force and pitch exciting moment for the incident wave frequency $\omega = 0.4$rad/s.

Figure 4.35 and 4.36 show the comparisons of the exciting force RAOs of a Series 60, Cb=0.7 ship from present method with the numerical results from MAPS0 and WAMIT. The RAOs of exciting forces are obtained from the converged time series of exciting forces. The present method results are in excellent agreement with the MAPS0 and WAMIT results.

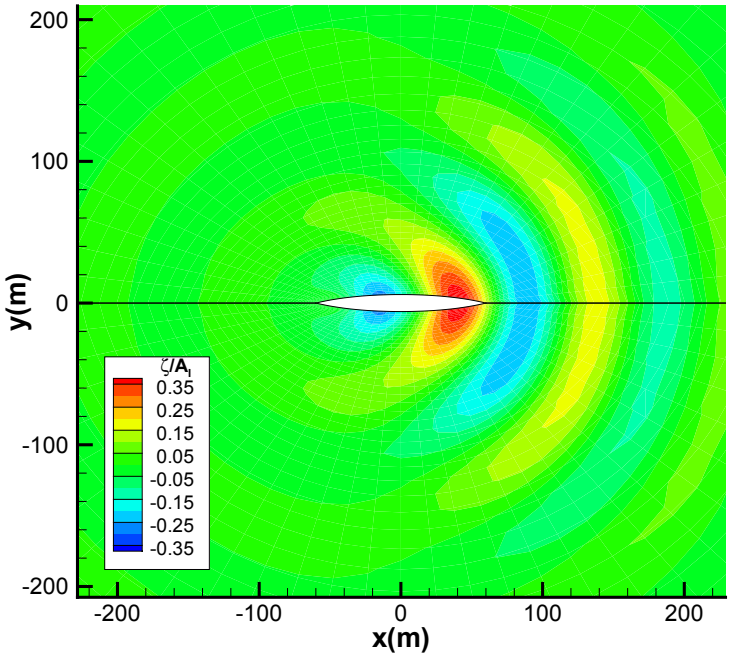

Figure 4.30: Instantaneous diffracted wave contour around the fixed Wigley I hull in an incident wave, $\omega = 0.8$rad/s.

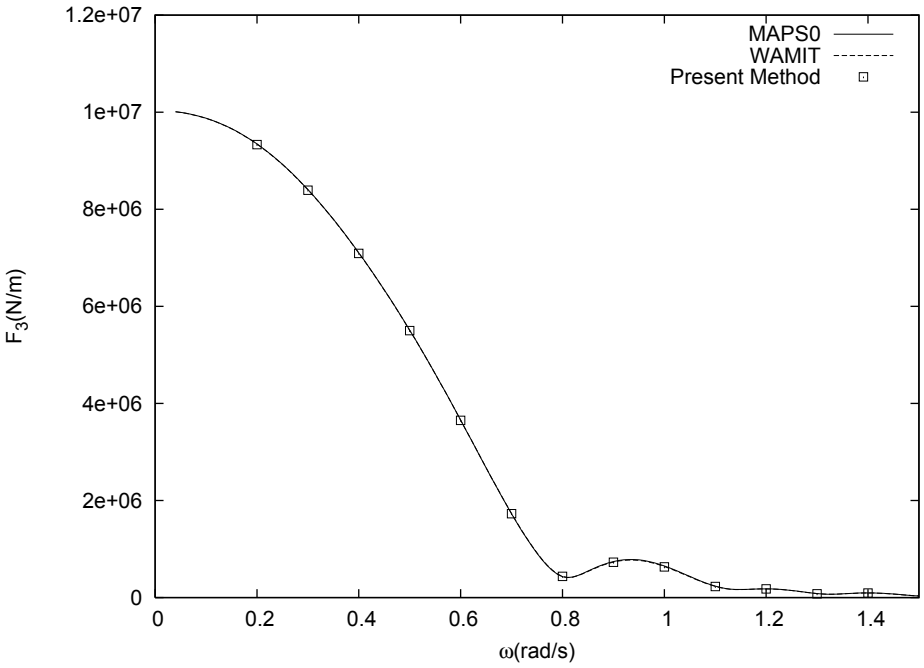

Figure 4.31: Heave exciting force RAO of the Wigley I hull.

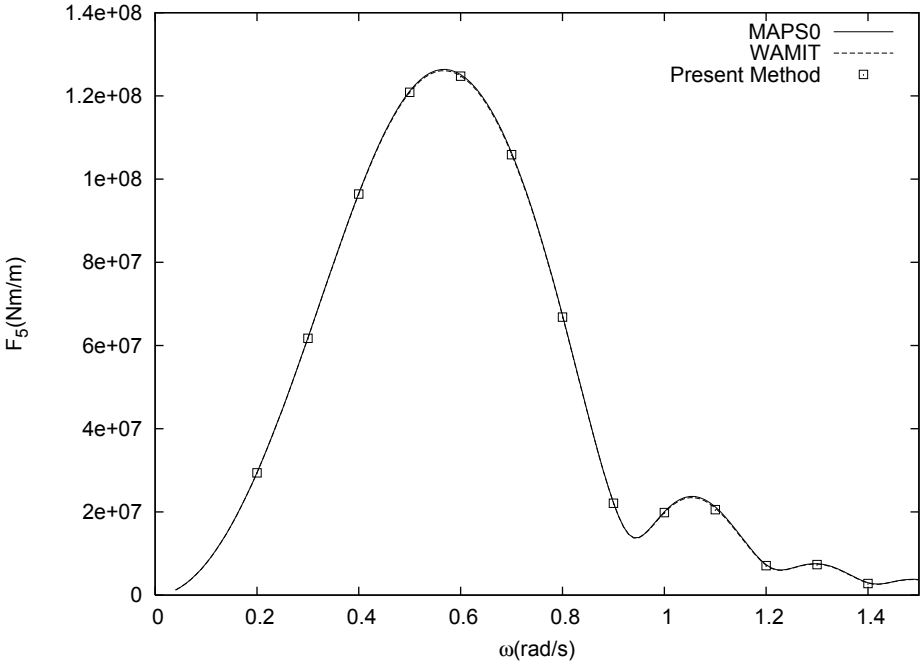

Figure 4.32: Pitch exciting moment RAO of the Wigley I hull.

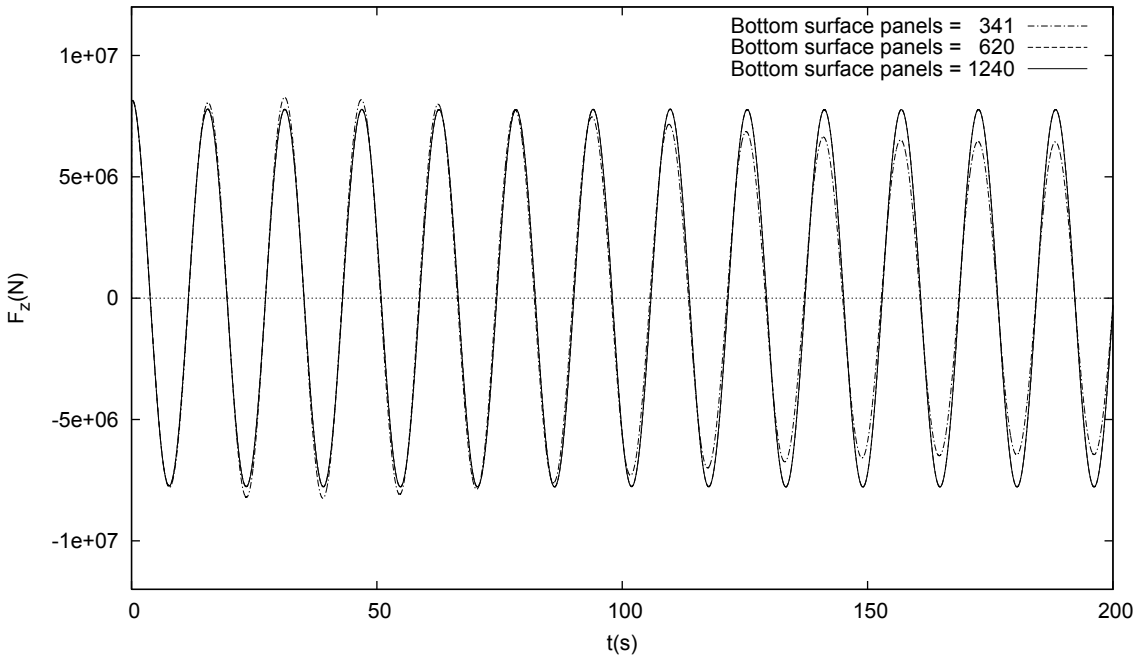

Figure 4.33: Comparison of the heave exciting force of a Series 60, Cb=0.7 ship for different number of panels on the bottom surface, $\omega = 0.4$rad/s.

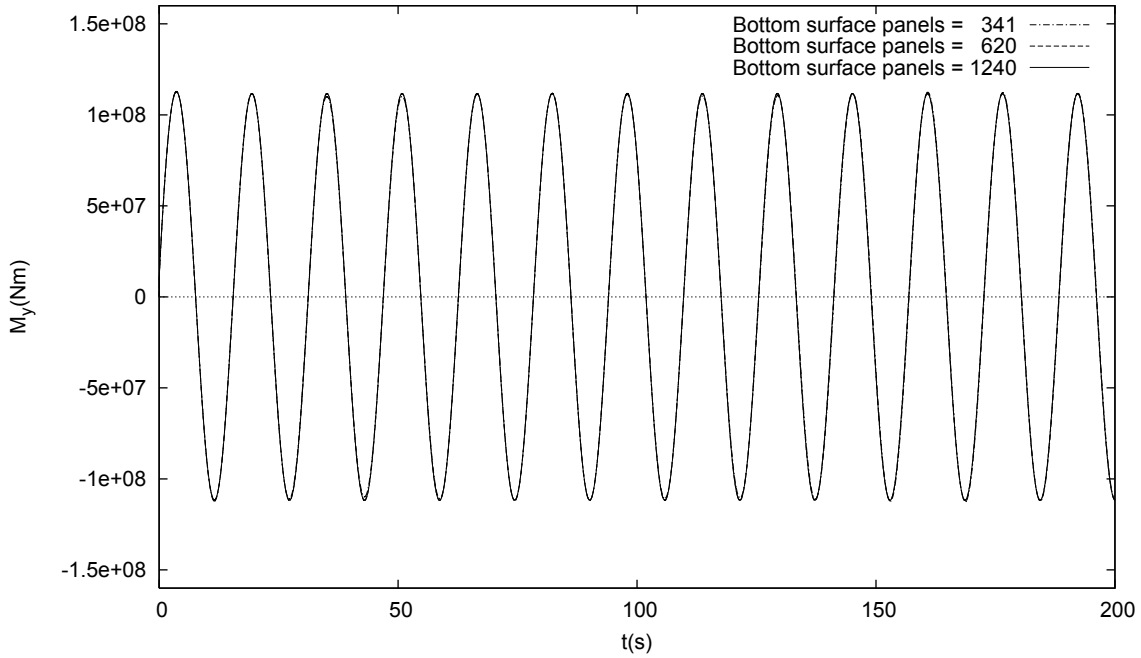

Figure 4.34: Comparison of the pitch exciting moment of a Series 60, Cb=0.7 ship for different number of panels on the bottom surface, $\omega = 0.4$rad/s.

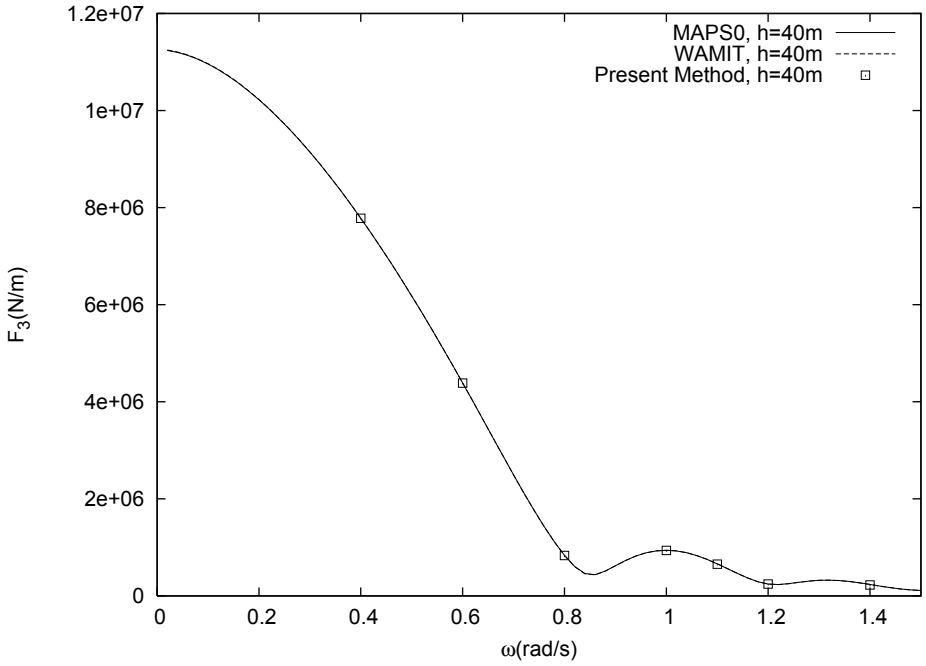

Figure 4.35: Heave exciting force RAO of a Series 60, Cb=0.7 ship.

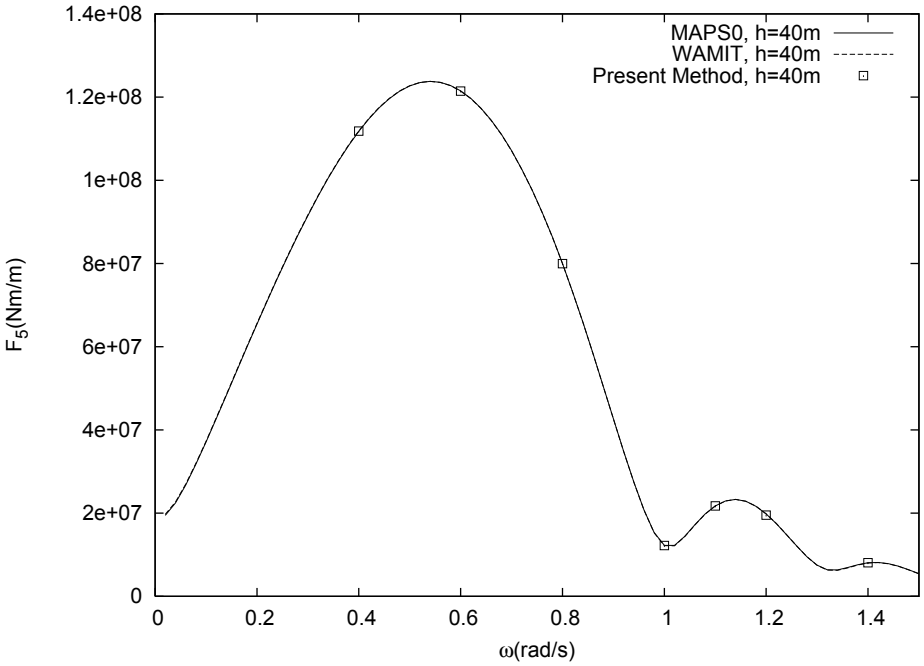

Figure 4.36: Pitch exciting moment RAO of a Series 60, Cb=0.7 ship.

For the two-body side-by-side moored scenario, the exciting forces are calculated for all 6-DOFs. Different number of panels on the gap portion of the free surface are used in the convergence studies, which are carried out at $\omega = 1.0$rad/s. Figure 4.37 and 4.38 illustrate the sway exciting force and roll exciting moment acting on the body located in the $y - axis$ positive position of the two-body side-by-side moored scenario, respectively. The time series shown are in the stable stage of the simulations. Convergence is reached very quickly for both sway force and roll moment.

Figure 4.39 illustrates the diffracted wave around the two-body side-by-side moored scenario at the incident wave frequency $\omega = 0.8$rad/s. The wave elevation in the contour is non-dimensionalized as m/m. The instantaneous wave elevation in the gap is about 1.8 times the incident wave elevation, which indicates that the wave elevation between the gap is amplified by the side-by-side configuration of the two bodies.

The RAOs of the exciting forces are extracted from the converged time series and compared with the numerical results from MAPS0 and WAMIT. Figures 4.61 to 4.44

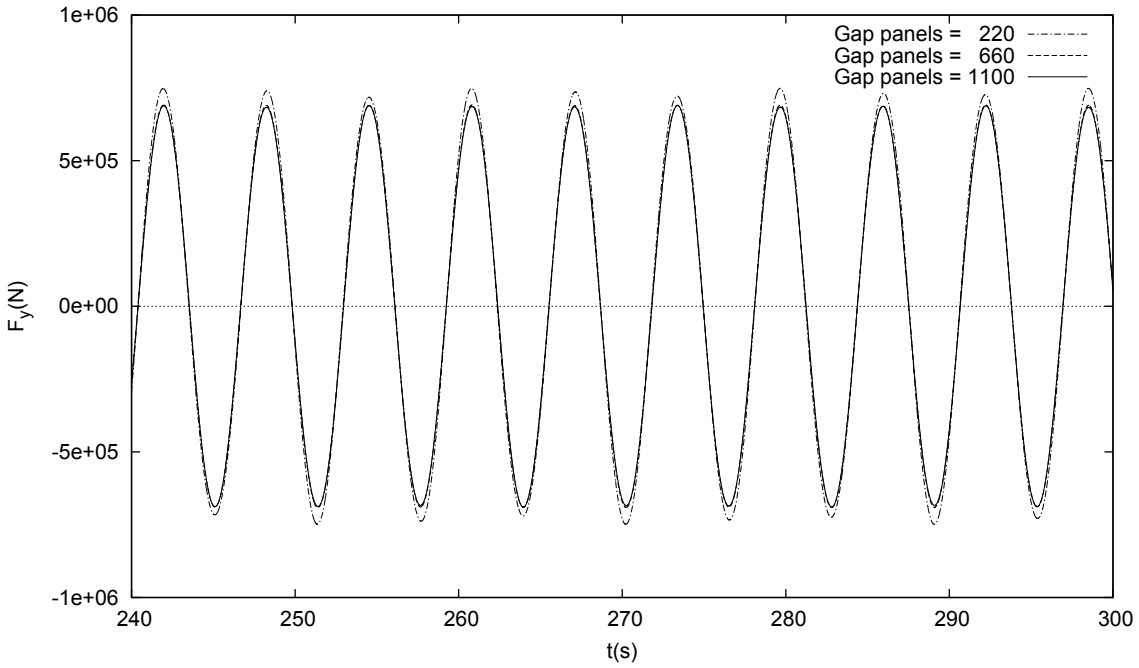

Figure 4.37: Comparison of the sway exciting force of the two-body side-by-side moored scenario for different number of panels on the gap, $\omega = 1.0$rad/s.

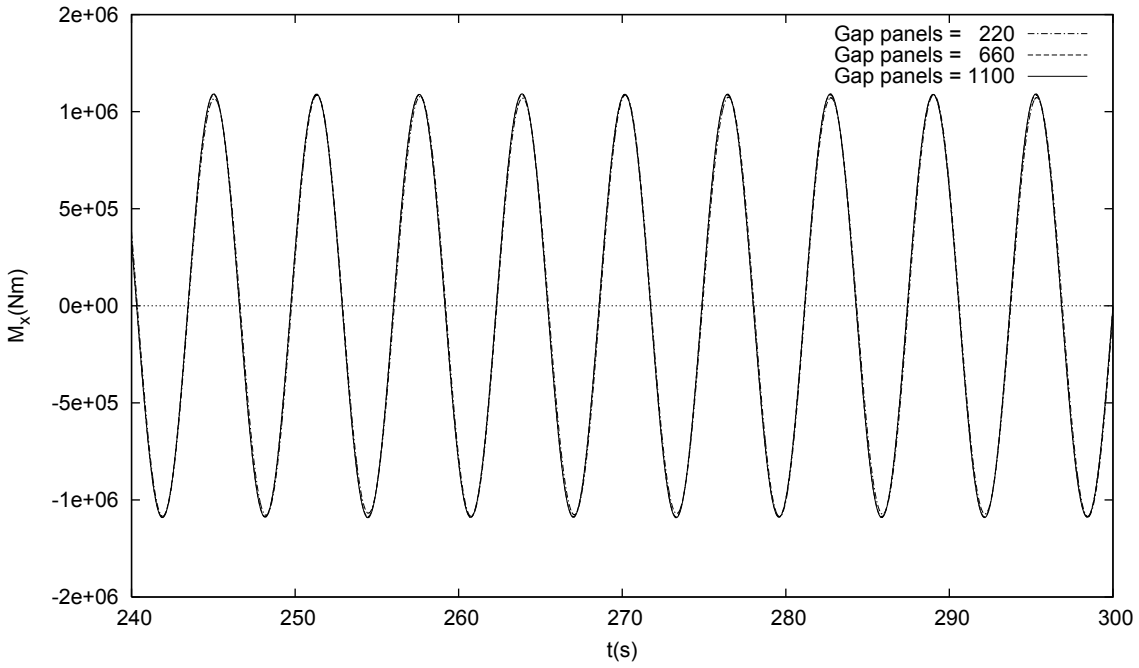

Figure 4.38: Comparison of the roll exciting moment of the two-body side-by-side moored scenario for different number of panels on the gap, $\omega = 1.0$rad/s.

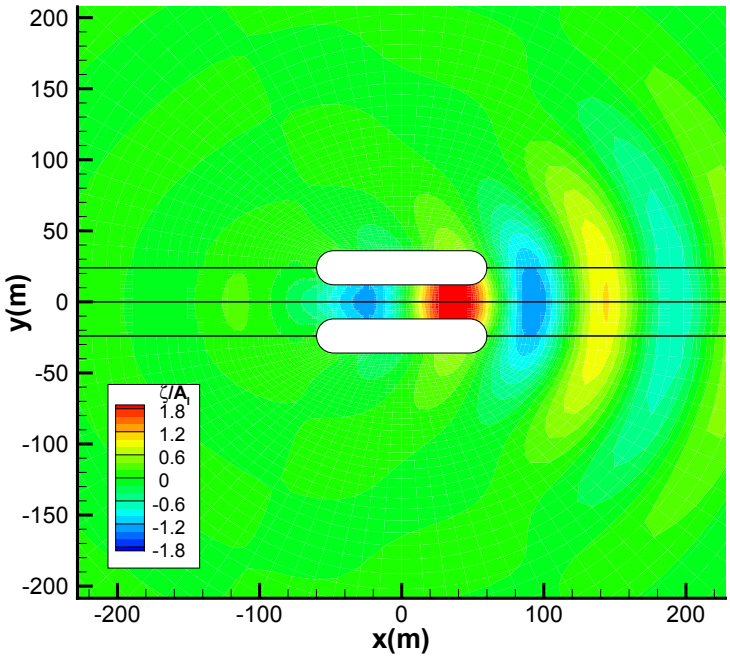

Figure 4.39: Instantaneous diffracted wave contour around the fixed two-body side-by-side moored scenario in incident wave, $\omega = 0.8$rad/s.

illustrate the good agreement of sway and heave exciting forces as well as roll, pitch, and yaw exciting moments from the present method with the MAPS0 and WAMIT results. The peak values of exciting forces/moments are predicted accurately.

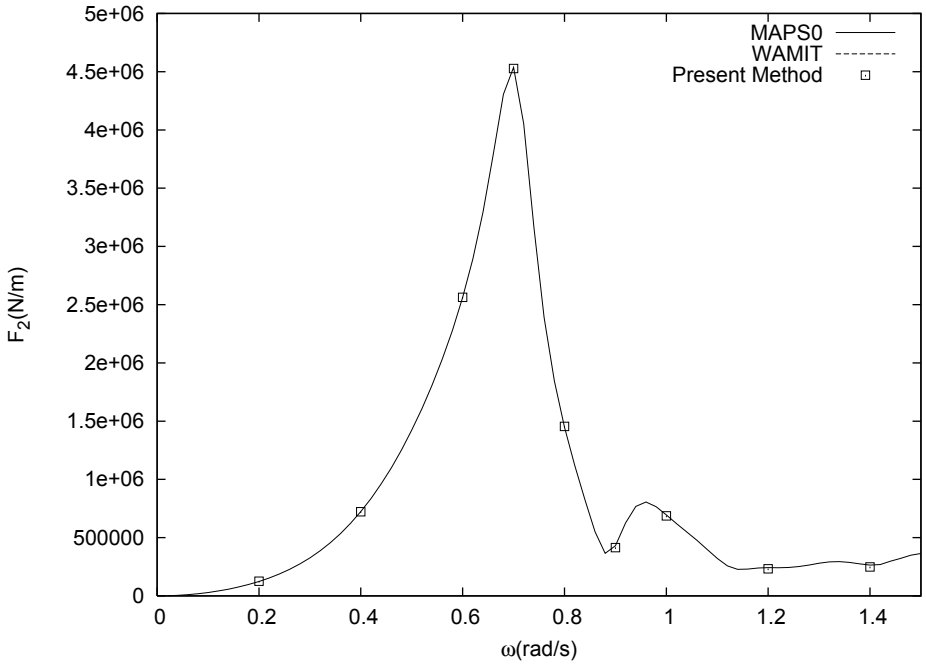

Figure 4.40: Sway exciting force RAO of the two-body side-by-side moored scenario.

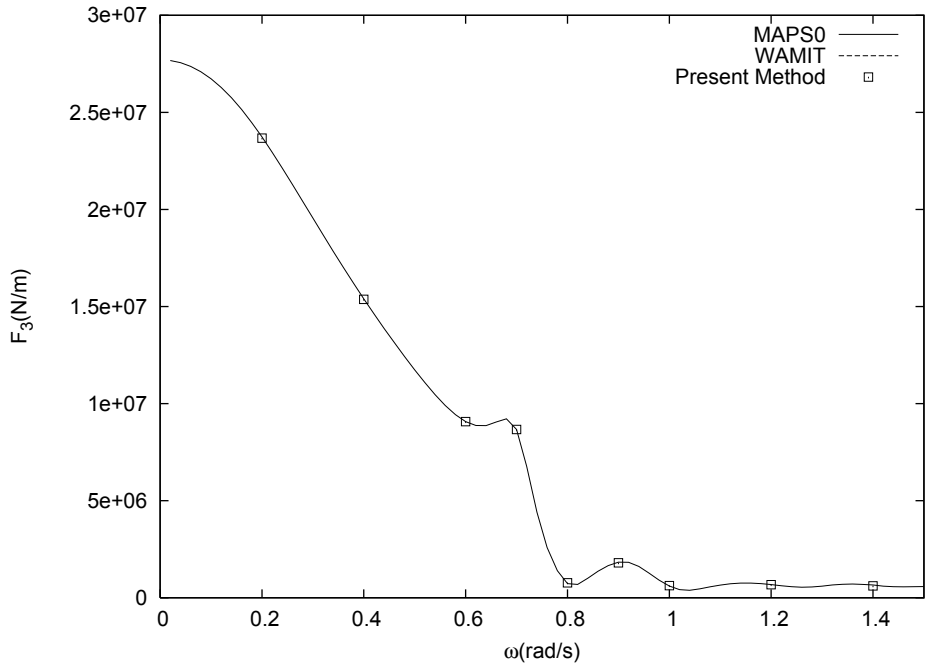

Figure 4.41: Heave exciting force RAO of the two-body side-by-side moored scenario.

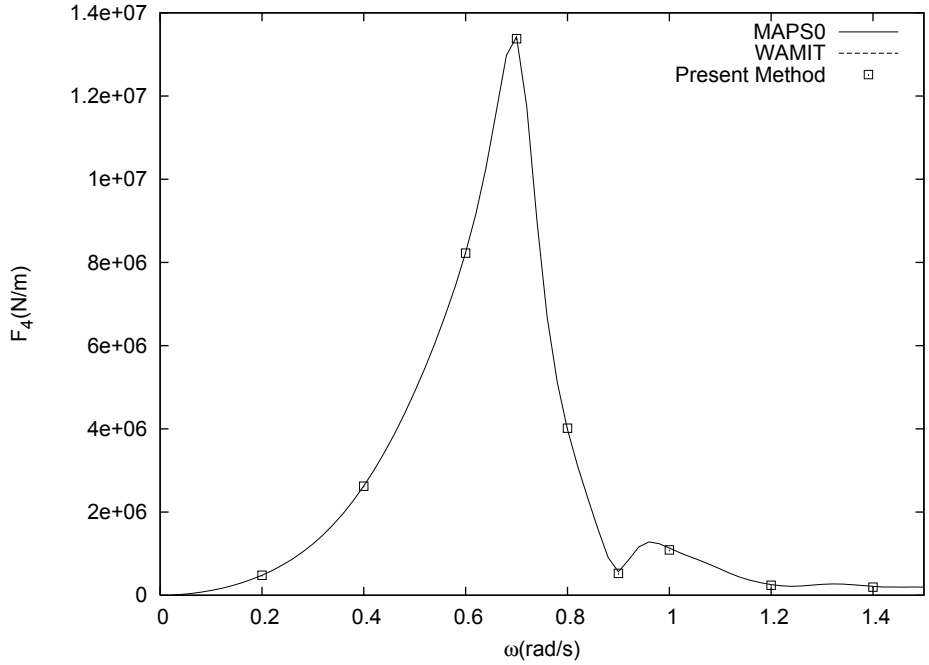

Figure 4.42: Roll exciting moment RAO of the two-body side-by-side moored scenario.

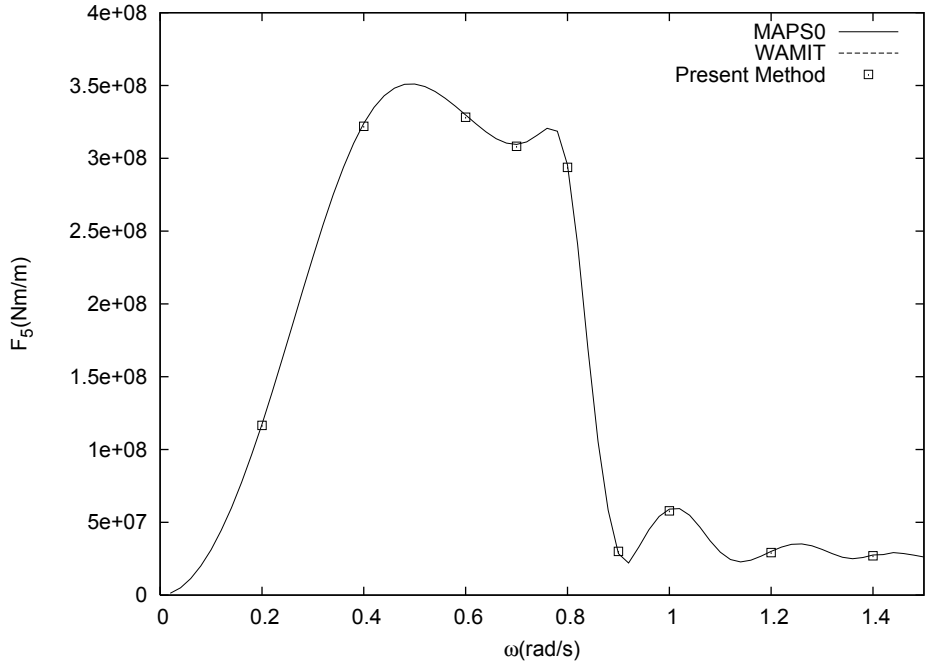

Figure 4.43: Pitch exciting moment RAO of the two-body side-by-side moored scenario.

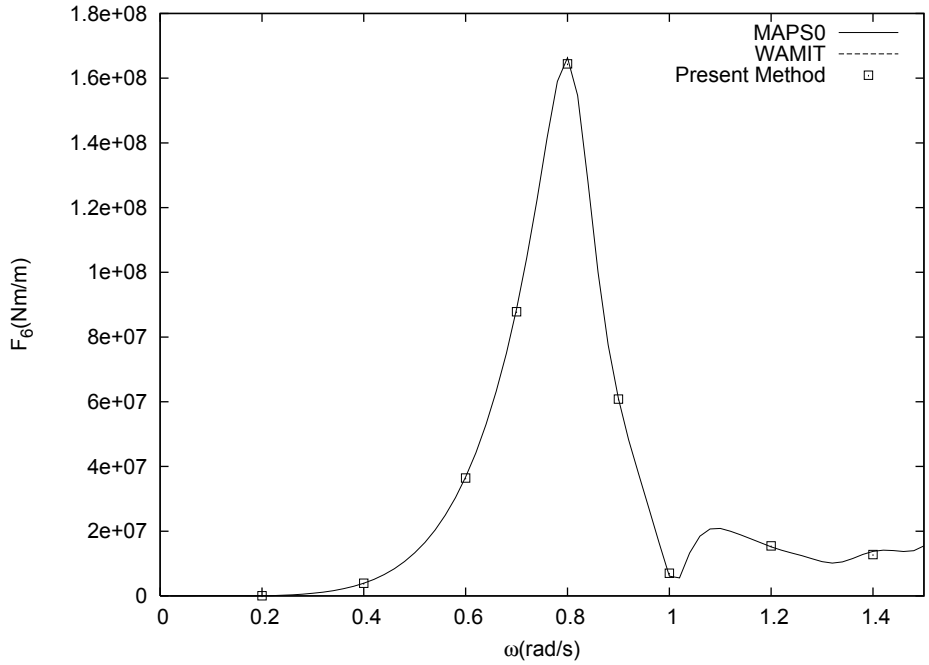

Figure 4.44: Yaw exciting moment RAO of two-body side-by-side moored scenario.

4.3 Free Motion Simulations

The free motion simulation solves the boundary value problem for the computational domain and the equations of ship motion simultaneously at each time step. In this thesis, the total velocity potential, including the radiation and diffraction potentials, is obtained by solving the boundary value problem for the free motion simulations, through which the total hydrodynamic pressures are computed and the total hydrodynamic forces are calculated by the direct integration of hydrodynamic pressures over the body surface. Then, the ship motions are obtained by solving equations of motion.

The free motion simulations are solved for the free decay tests of the ship, which refer to the transition of the ship from a prescribed state to its equilibrium position, followed by the free motion of the ship with the presence of an incident sinusoidal wave.

4.3.1 Free Decay Tests

The free decay tests are conducted for the Wigley I hull from the prescribed heave displacement ξ_3^0 and pitch displacement ξ_5^0, respectively. There is no incident wave for the free decay tests. Convergence studies have been carried out for the heave and pitch decay tests using different number of panels on the free surface and different time step sizes. Figure 4.45 and 4.46 show the convergence of the heave motion for the Wigley I hull in the heave decay test. The heave motion ξ_3 decays quickly from ξ_3^0 to zero in about eight natural periods of heave motion. The heave motion converges as the number of panels on the free surface increase and the time step size decreases. Figure 4.47 and 4.48 illustrate the convergence of the pitch motion for the Wigley I hull in the pitch decay test. The pitch motion ξ_5 also decays quickly in about seven

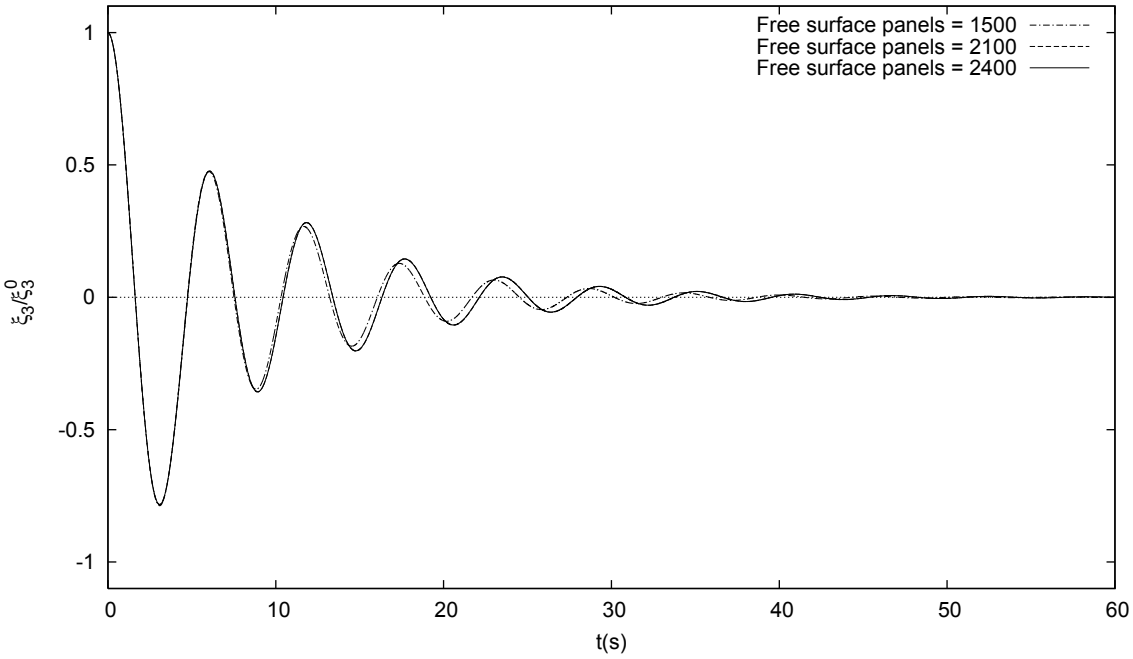

Figure 4.45: Comparison of the heave decay of the Wigley I hull for different number of panels on the free surface.

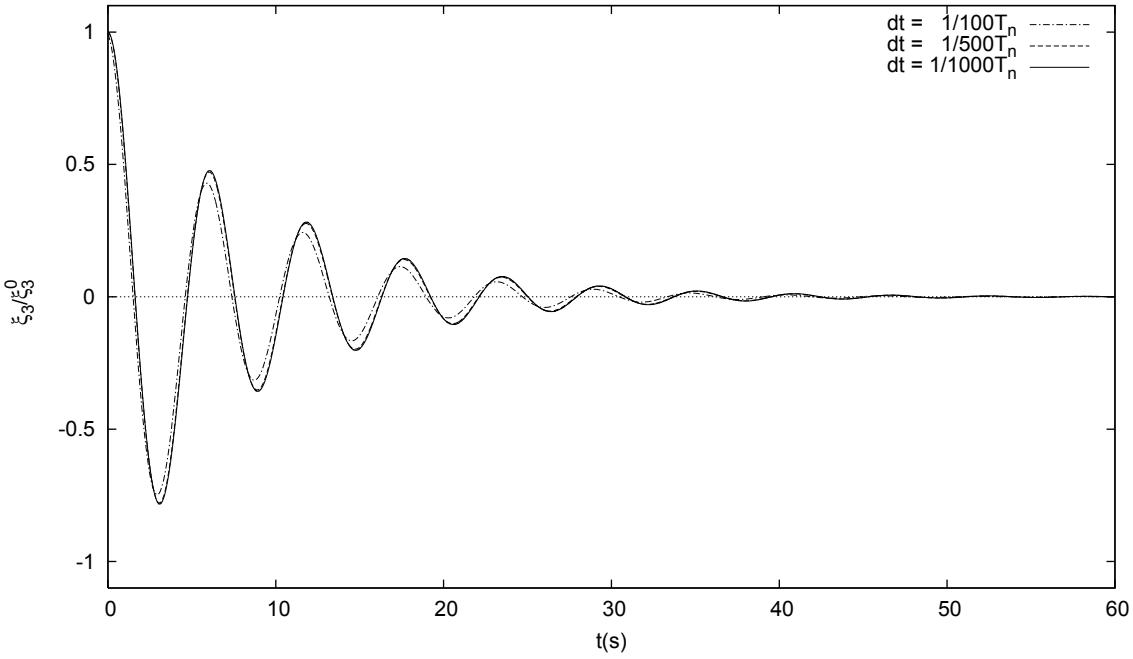

Figure 4.46: Comparison of the heave decay of the Wigley I hull for different time step sizes.

natural pitch periods. Good convergence of the pitch motion with the number of panels on the free surface and the time step size is also demonstrated in the figures.

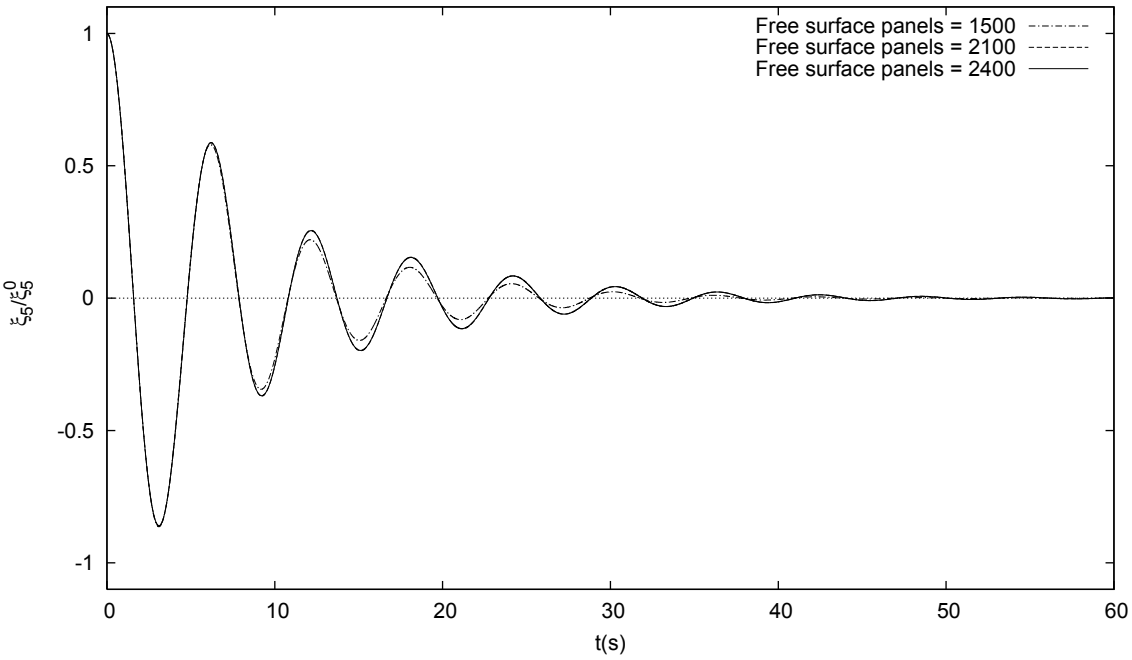

Figure 4.47: Comparison of the pitch decay of the Wigley I hull for different number of panels on the free surface.

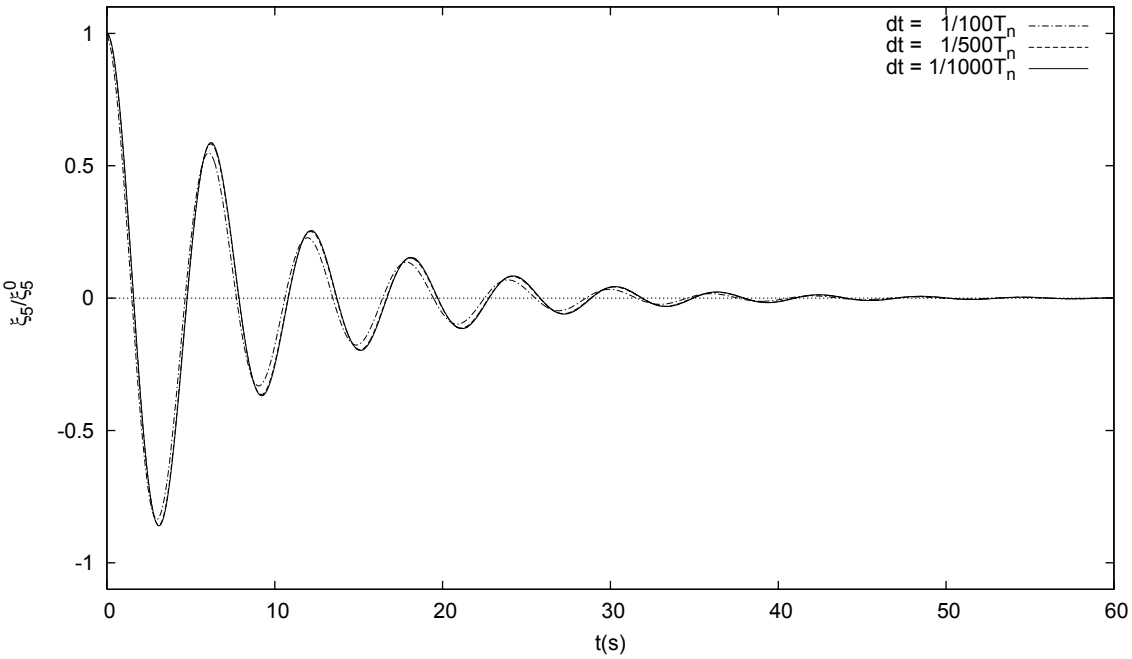

Figure 4.48: Comparison of the pitch decay of the Wigley I hull for different time step sizes.

4.3.2 Free Motion in Monochromatic Waves

The free motion simulations in monochromatic waves are solved for the Wigley I hull in deep water, a Series 60, Cb=0.7 ship in a finite water depth, and the two-body side-by-side moored scenario. Convergence studies of ship motions have been carried out with different time step sizes and number of panels on the free surface and bottom surface.

Figure 4.49 and 4.52 illustrate the heave and pitch motions of the freely floating Wigley I hull with an incident wave in head sea condition. The time series of heave and pitch motions are stable after the transient stage. Both the heave and pitch motion converge as the number of panels on the free surface increases and the time step size decreases.

Figure 4.53 shows the instantaneous disturbed wave contour around the Wigley I hull during free motion. The disturbed wave includes the radiated wave and the diffracted

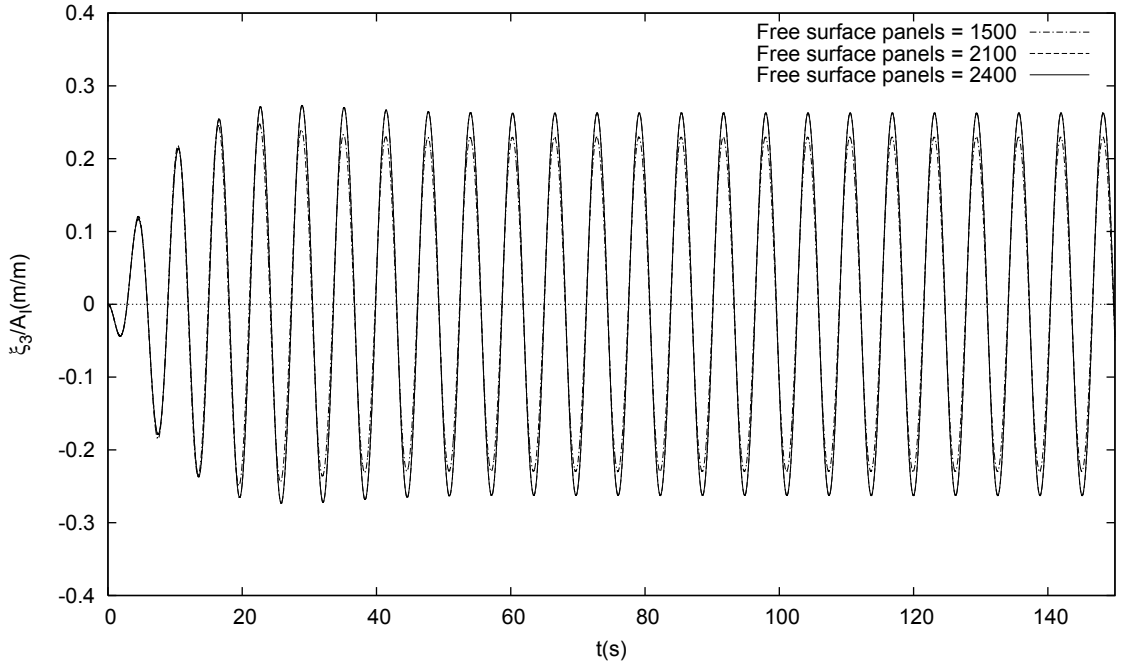

Figure 4.49: Comparison of the heave motion of the Wigley I hull for different number of panels on the free surface, $\omega = 1.0$rad/s.

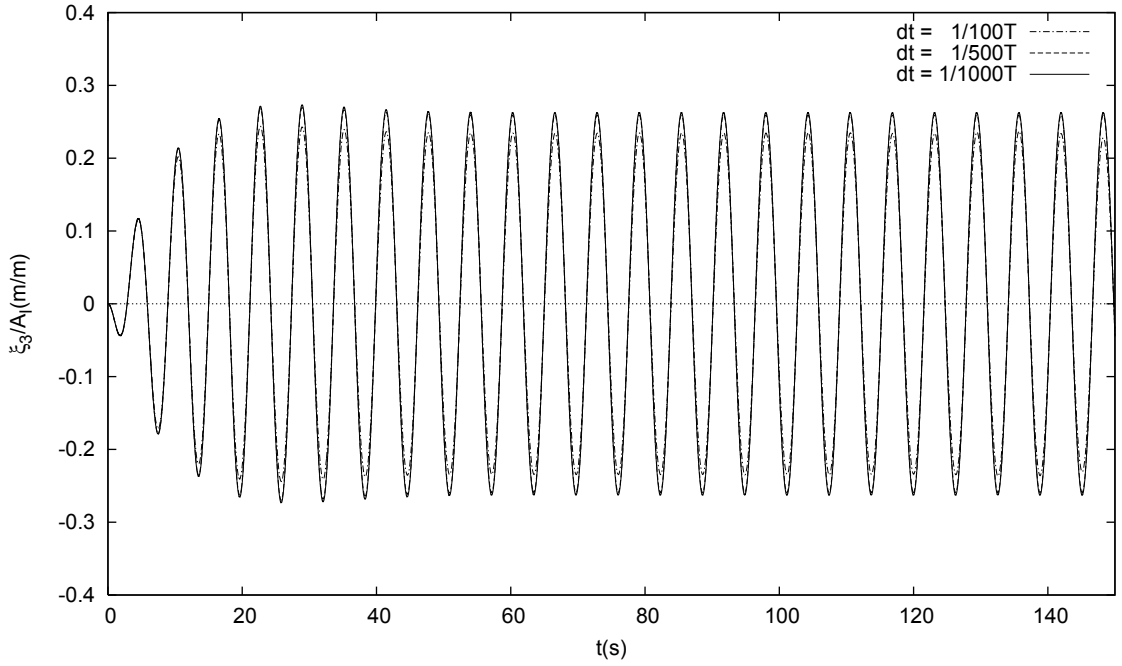

Figure 4.50: Comparison of the heave motion of the Wigley I hull for different time step sizes, $\omega = 1.0$rad/s.

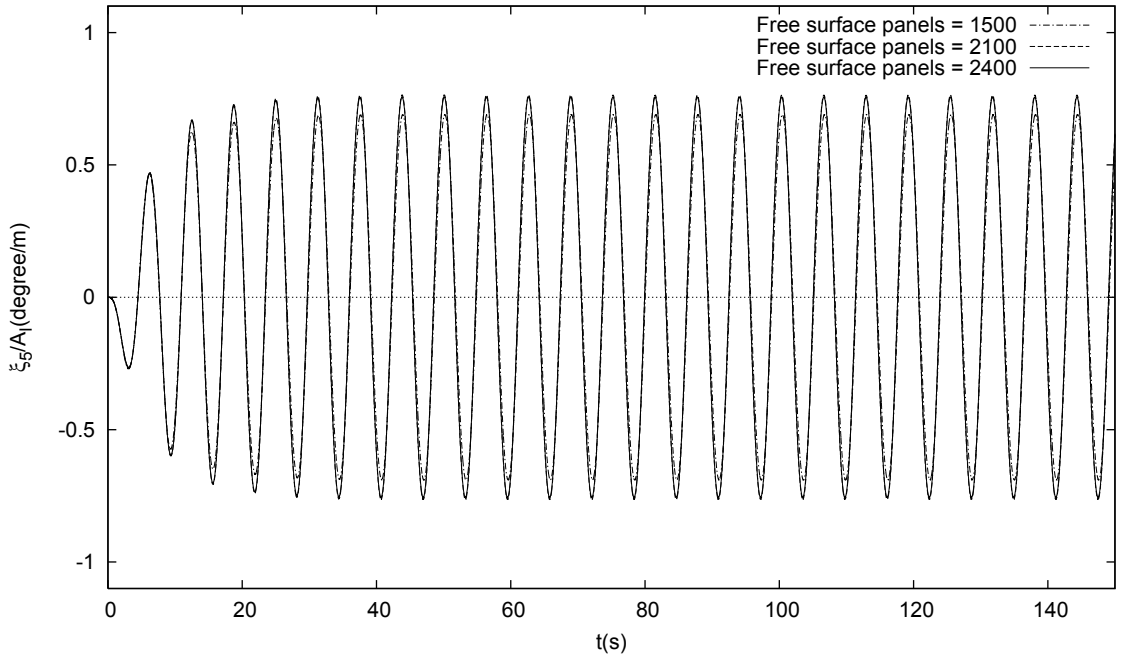

Figure 4.51: Comparison of the pitch motion of the Wigley I hull for different number of panels on the free surface, $\omega = 1.0$rad/s.

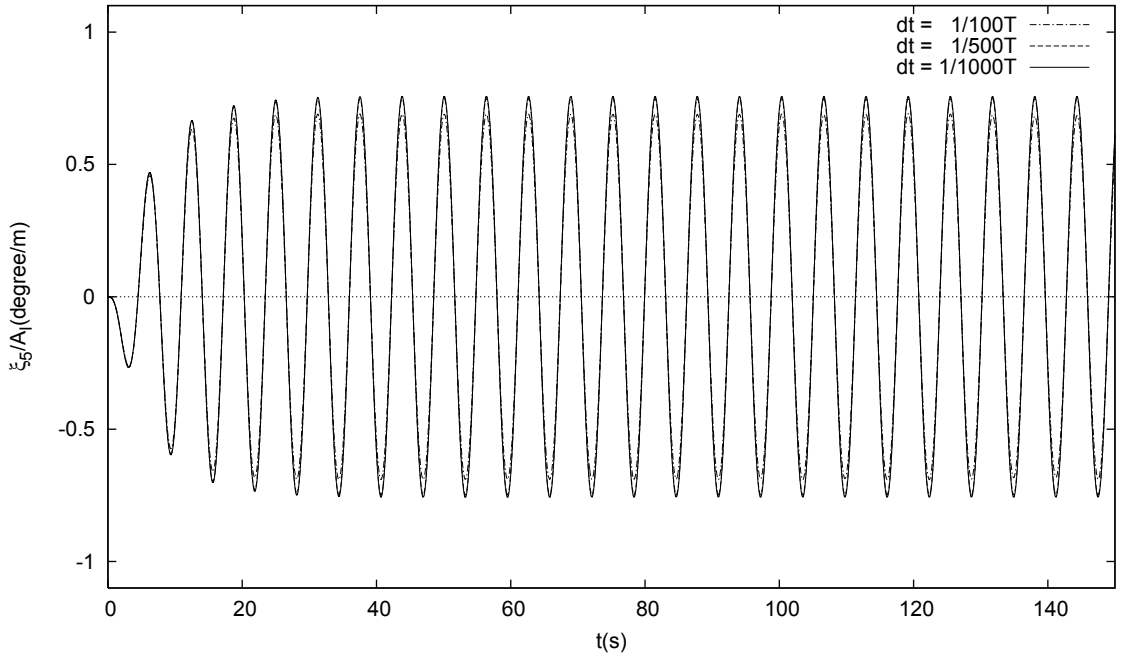

Figure 4.52: Comparison of the pitch motion of the Wigley I hull for different time step sizes, $\omega = 1.0$rad/s.

wave which are induced by the motion of the ship and the presence of the ship in the incident wave, respectively. The wave elevation in the contour is non-dimensionalized as m/m.

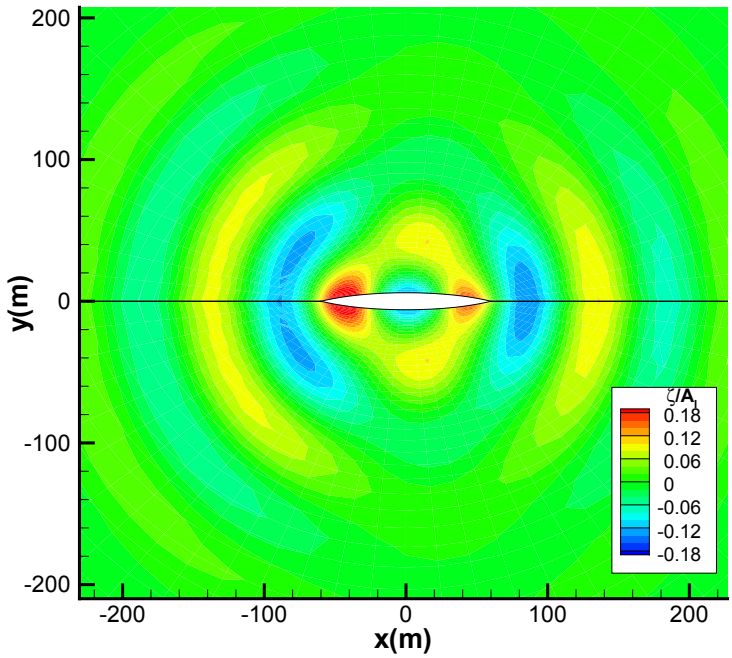

Figure 4.53: Instantaneous disturbed wave contour around the free floating Wigley I hull with free motion, $\omega = 0.8$rad/s.

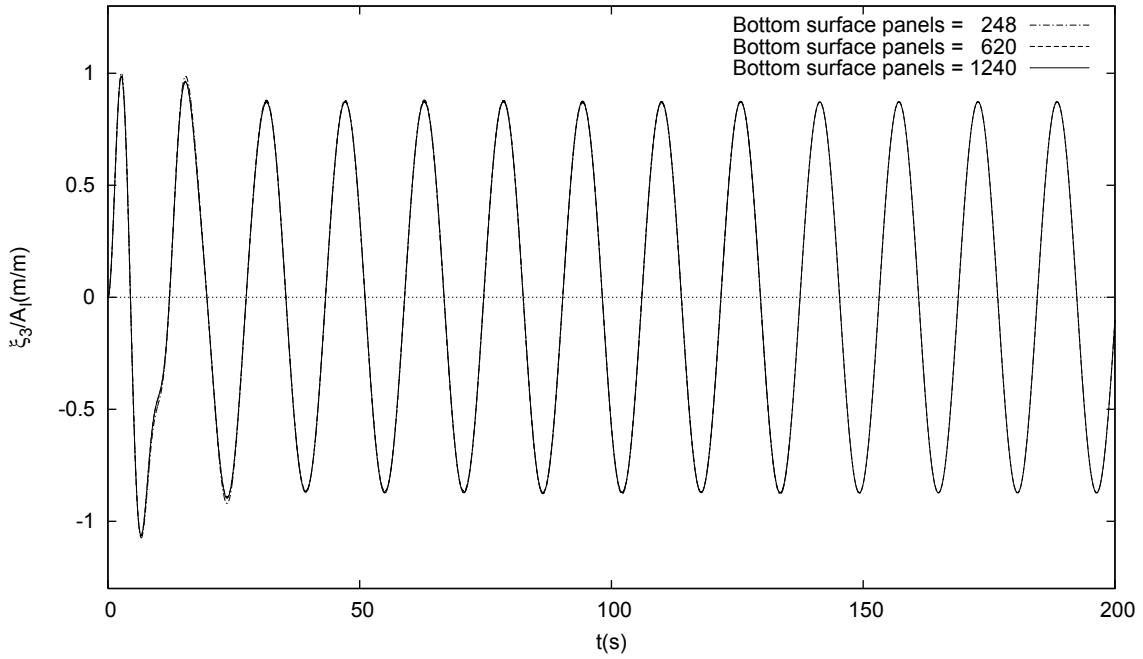

Figure 4.54: Comparison of the heave motion of a Series 60, Cb=0.7 ship for different number of panels on the bottom surface, $\omega = 0.4$rad/s.

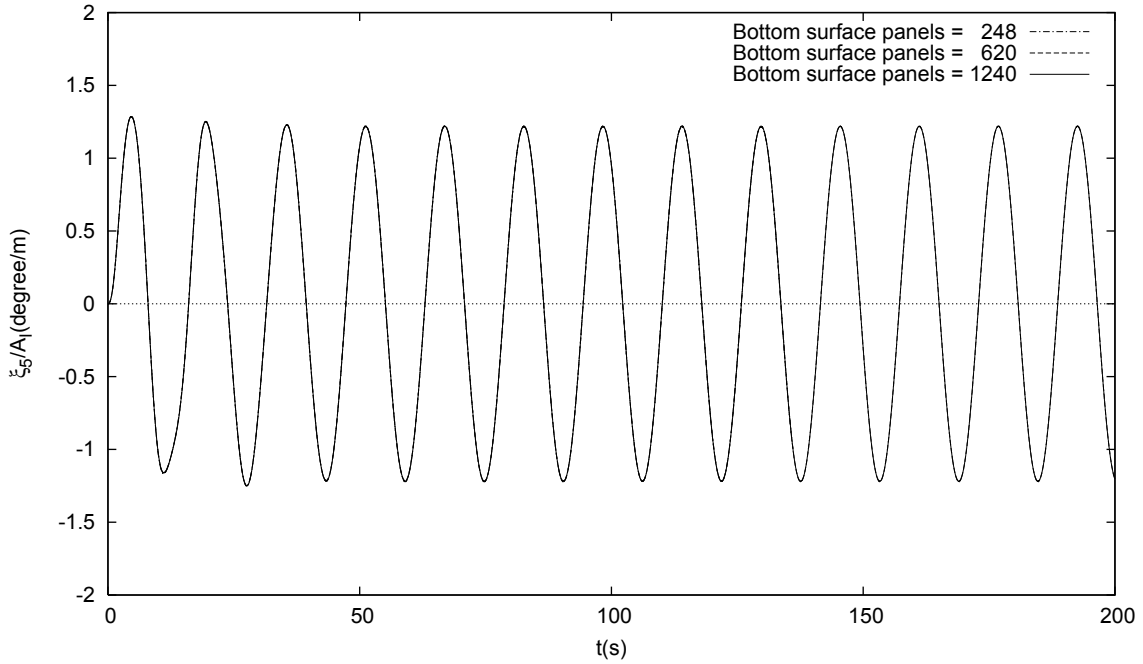

Figure 4.55: Comparison of the pitch motion of a Series 60, Cb=0.7 ship for different number of panels on the bottom surface, $\omega = 0.4$rad/s.

4.3.3 Motion Response Amplitude Operators

The heave and pitch motion RAOs of the Wigley I hull in deep water and a Series 60, Cb=0.7 ship in finite water depth are extracted from the converged time series of ship motions and compared with the numerical results from MAPS0 and WAMIT. Figure 4.56 and Figure 4.57 show that the RAOs of wave-induced heave and pitch motions at selected frequencies are in good agreement with the numerical results from frequency-domain programs MAPS0 and WAMIT.

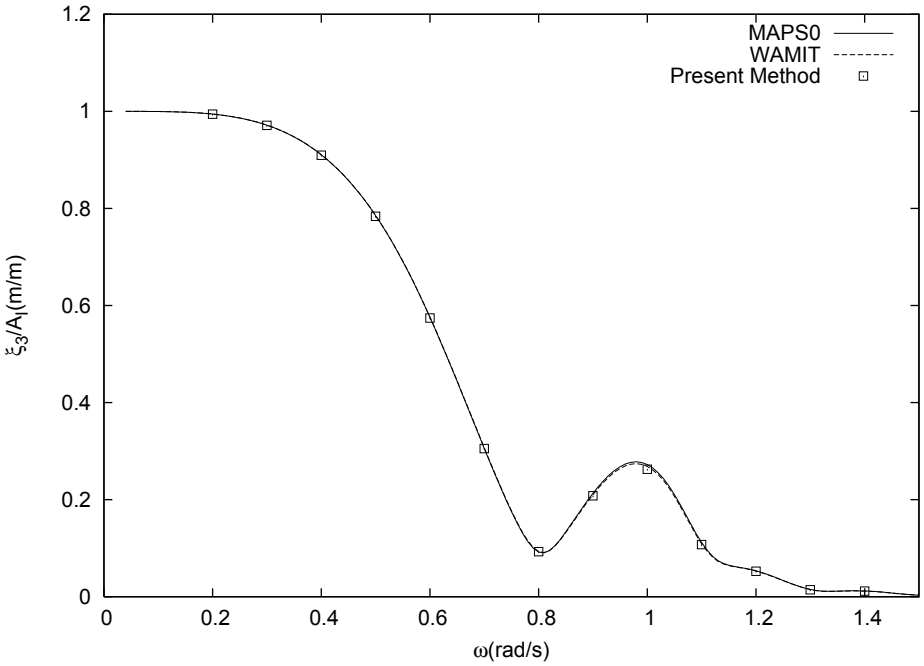

Figure 4.56: Heave motion RAO of the Wigley I hull.

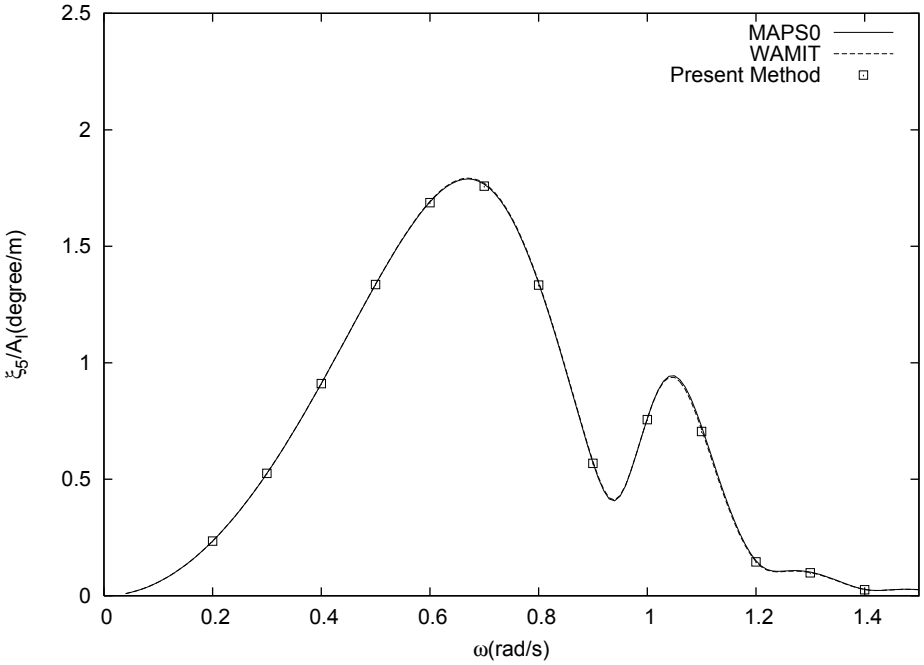

Figure 4.57: Pitch motion RAO of the Wigley I hull.

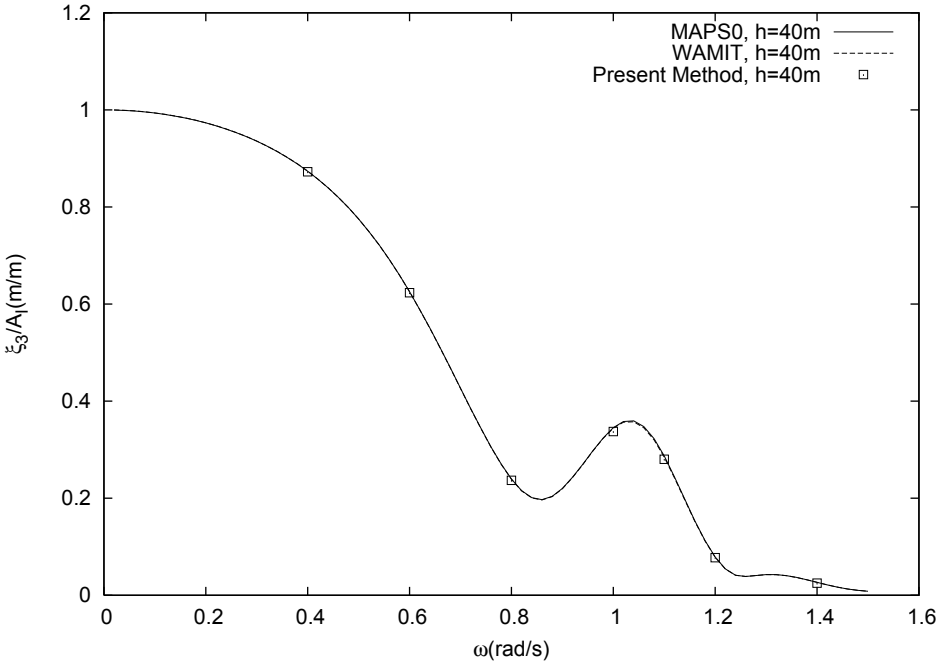

Figure 4.58: Heave motion RAO of a Series 60, Cb=0.7 ship.

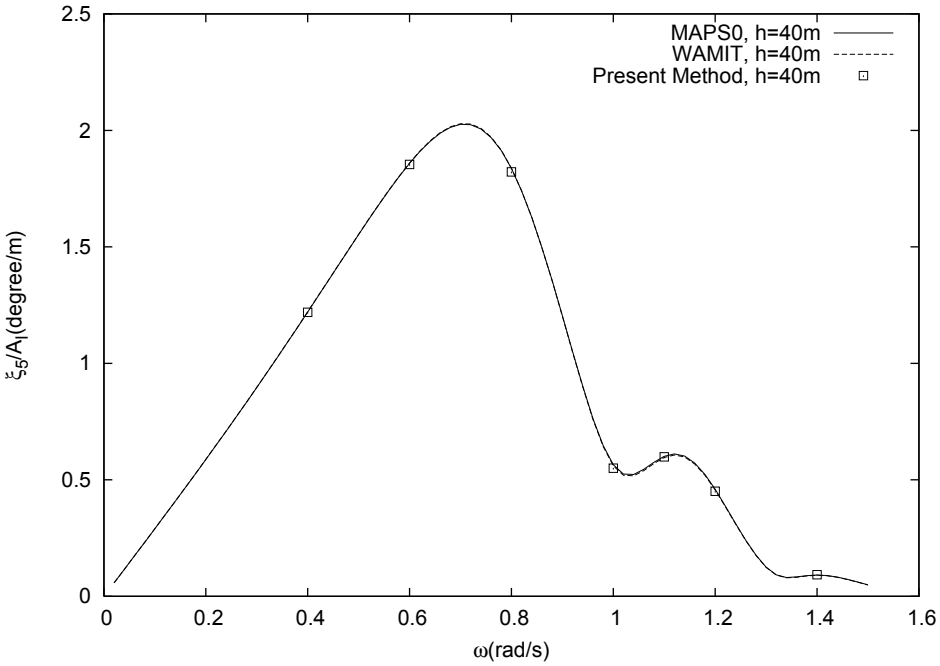

Figure 4.59: Pitch motion RAO of a Series 60, Cb=0.7 ship.

The sway, heave, roll, and pitch RAOs are calculated for the two-body side-by-side moored scenario in head sea condition and compared with the numerical results from the frequency-domain programs MAPS0 and WAMIT and the experimental data. No artificial roll damping is applied for both the time-domain and frequency-domain solutions. Figure 4.61 illustrates the sway motion RAO of the two-body scenario. The sway motion is significant between incident wave frequency $\omega = 0.8$rad/s and $\omega = 1.0$rad/s. The predicted sway motion is in good agreement with the frequency-domain solutions at a wide frequency range. The peak value at $\omega = 0.92$rad/s is well predicted. The discrepancy between the present method result and the frequency-domain result at the peak value may be caused by the numerical damping introduced by the discretization of the free surface. There is a small peak for sway motion at the natural frequency of roll motion $\omega = 0.6$rad/s, which is also well captured. The trend and value of sway motion from the present method and other frequency-domain programs are in fair agreement with the experimental data.

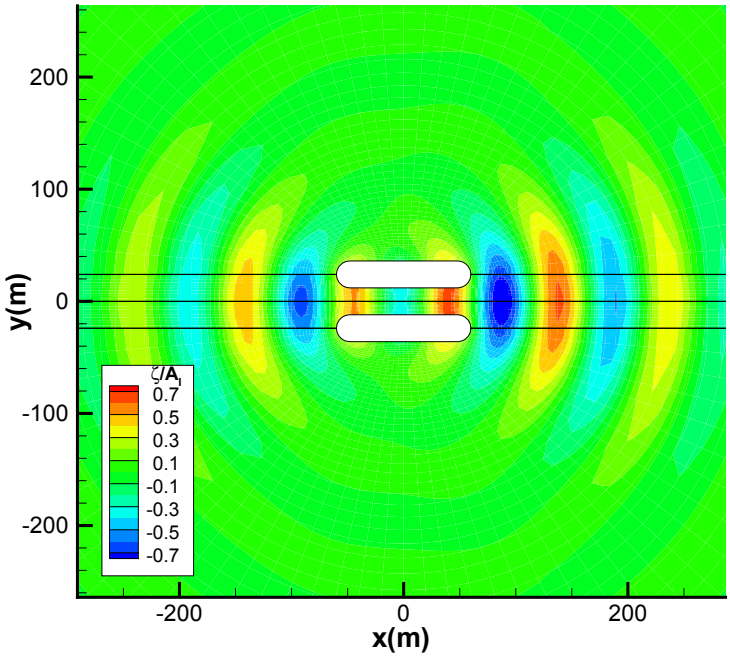

Figure 4.60: Instantaneous disturbed wave contour around the free floating two-body side-by-side moored scenario in incident wave, $\omega = 0.8$rad/s.

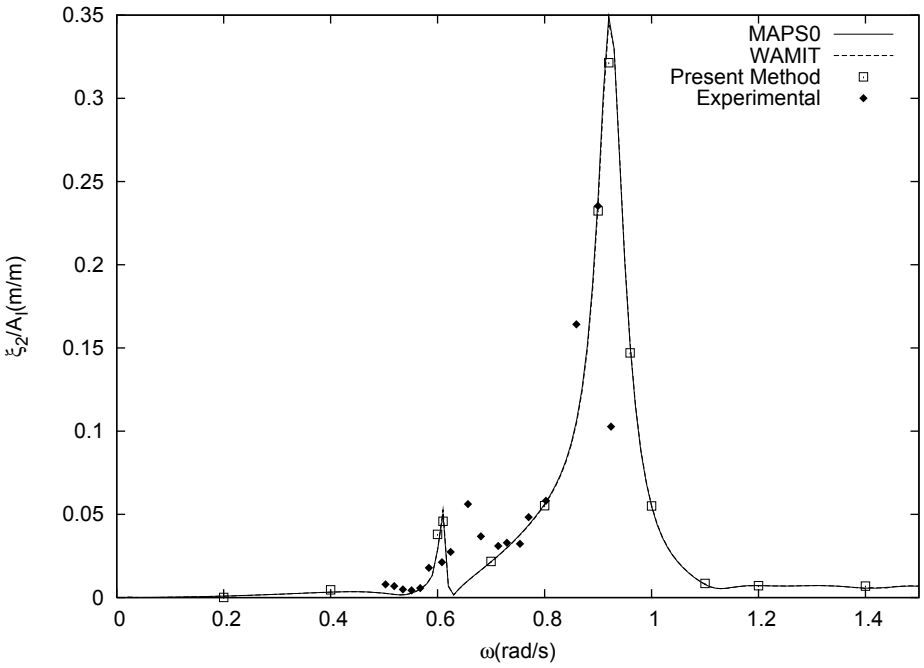

Figure 4.61: Sway motion RAO of the two-body side-by-side moored scenario.

Figure 4.62 illustrates the heave motion RAO of the two-body scenario. The peak of the heave motion is located between frequency $\omega = 0.8$rad/s and $\omega = 1.0$rad/s where the interaction between the two bodies is significant. The peak value at $\omega = 0.92$rad/s is well predicted. The predicted heave motion is in good agreement with the experimental data at a wide range of frequencies. The value at the peak agrees well with the experimental measurement.

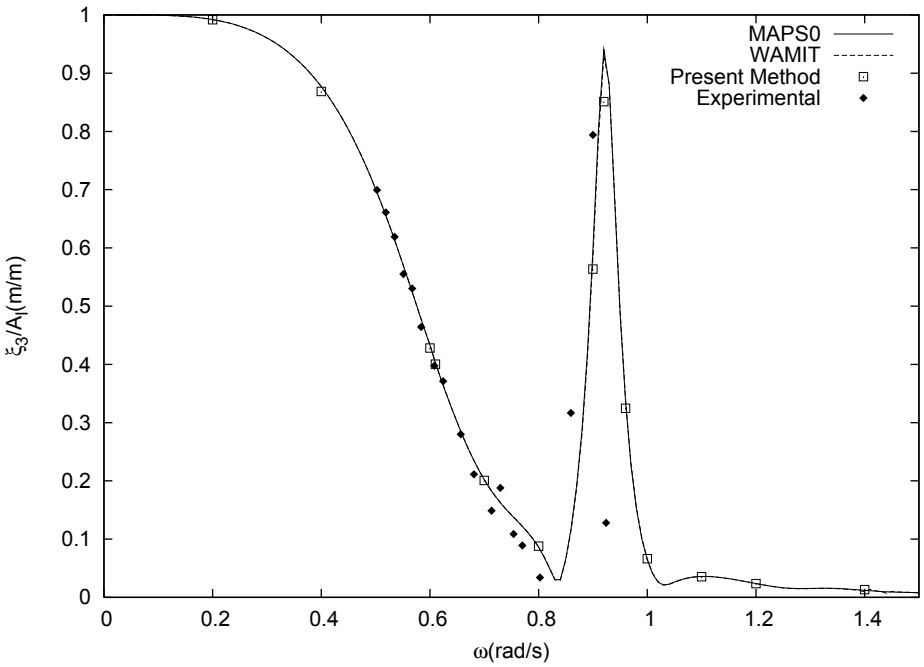

Figure 4.62: Heave motion RAO of the two-body side-by-side moored scenario.

The roll decay test is conducted for a single hull of the two-body side-by-side scenario. Figure 4.63 illustrates the time history of the roll angle in the roll decay test and the peak values of each swing. The estimation of the ratio of roll damping β from the the roll decay test follows the approach of constructing the extinction curve of the roll decay test data. The amplitude of the roll angle at the n-th swing is defined as ξ_4^n. The mean value of the amplitude of the n-th swing is defined as ξ_{mean}^n and the n-th

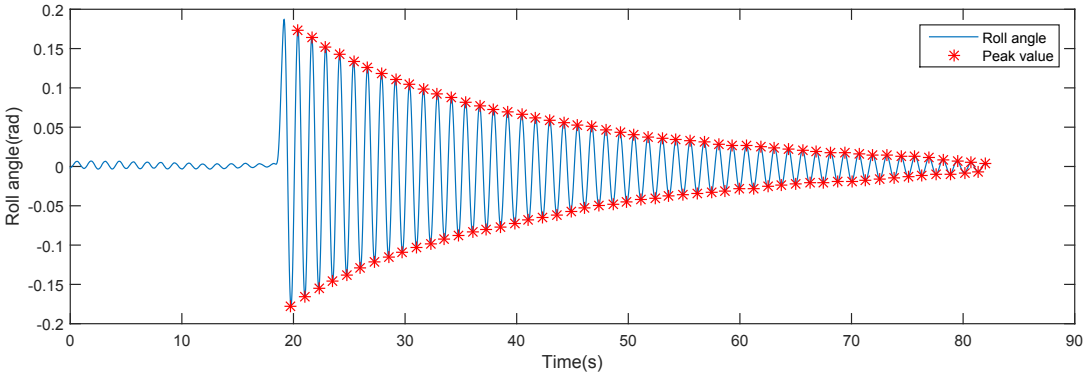

Figure 4.63: Time history of the roll decay test of a single hull.

decrement of amplitude between each swing is defined as $\delta\xi^n$ with

$$\begin{aligned} \delta\xi^n &= (\xi_4^n - \xi_4^{n-1}), \\ \xi_{mean}^n &= \frac{1}{2}(\xi_4^n + \xi_4^{n-1}). \end{aligned} \tag{4.1}$$

Figure 4.64 illustrates the extinction curve of $\delta\xi$ versus ξ_{mean} and its linear fitted curve $\delta\xi = a_0\,\xi_{mean}$, where a_0 is the slope of the fitted curve. The ratio of roll damping β is defined by $\beta = a_0/\pi = 0.0095$.

Figure 4.65 illustrates the roll motion RAO of the two-body scenario. The resonance frequency of the roll motion happens at the natural frequency of roll motion $\omega =$ 0.61rad/s. The predicted roll motion RAO without viscous roll damping is in good agreement with the corresponding results from MAPS0 and WAMIT. The ratio of viscous roll damping $\beta = 0.0095$ used for the roll motion simulation is obtained from the roll decay test. There are significant decreases of the peak values of the roll motion at the resonance frequency $\omega = 0.61$rad/s and its vicinity $\omega = 0.60$rad/s. No change is observed at other frequencies. The trend and value of the predicted roll motion are in fair agreement with the experimental data. The peak value near frequency $\omega = 0.9$rad/s is near 1.6 degree/m. There is no such value from present method or other frequency-domain programs.

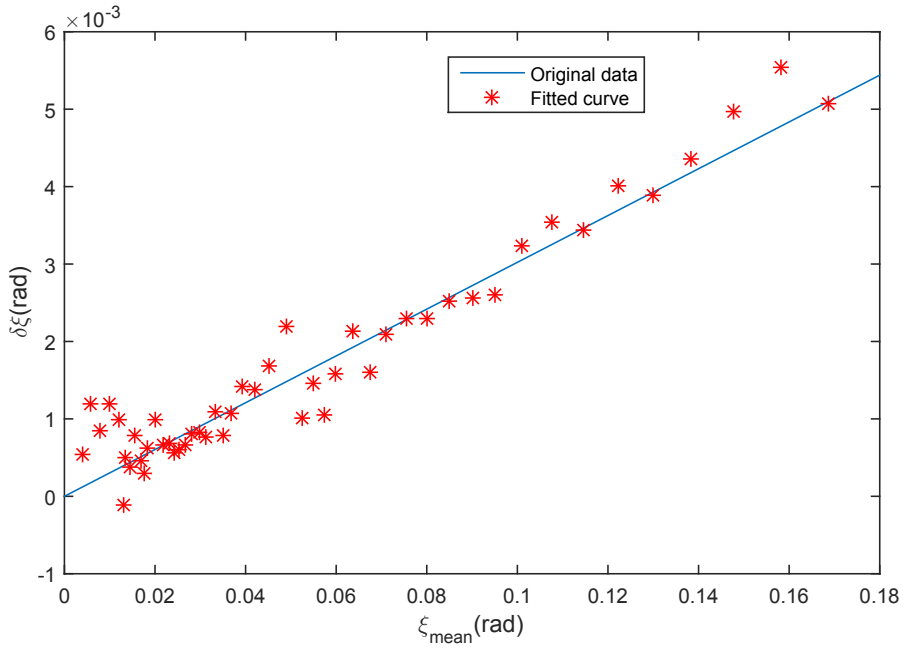

Figure 4.64: Extinction curve of the roll decay test data.

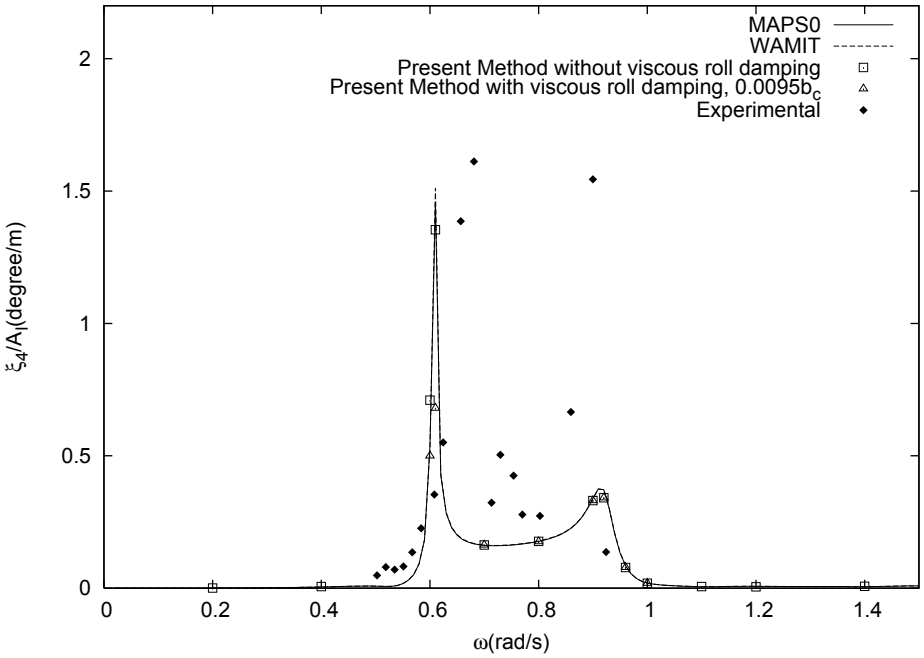

Figure 4.65: Roll motion RAO of the two-body side-by-side moored scenario.

Figure 4.43 illustrates the pitch motion RAO of the two-body scenario. The predicted pitch motion is in good agreement with the frequency domain solutions. The peak value of the pitch motion is well predicted at frequency $\omega = 0.96$rad/s. The pitch motion from the present method and other frequency-domain programs are in good agreement with the experimental data at all frequencies.

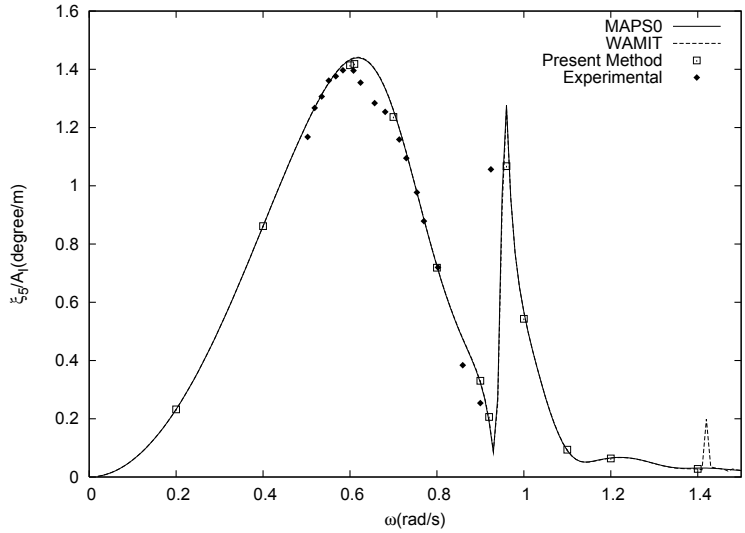

Figure 4.66: Pitch motion RAO of the two-body side-by-side moored scenario.

Chapter 5

Conclusions and Future Work

In this thesis, a numerical program was developed to simulate the wave-induced motions of floating bodies in the time domain. It was validated through a wide range of frequencies for various ship and floating body geometries in both the deep water and finite water depth. It was also demonstrated to be valid for the simulation of the two-body interaction condition. The program in this work solves the linear seakeeping problem at zero forward speed with the constant Rankine panel method. It provides a foundation that can be extended to solve nonlinear problems with advance speed.

A detailed literature review focused on the time-domain simulation of ship motion and the development of the Rankine panel method has been provided. It is found that the Rankine panel method has been widely used in the time-domain simulation of ship motion and it has great potential to solve nonlinear seakeeping problems and problems with arbitrary bathymetry in the time domain.

The mathematical formulation for the boundary value problem was derived. The linear formulation used in this thesis was degraded from the Weak-Scatterer formulation, which was originally linearized from the fully nonlinear formulation. The boundary integral equation was derived by applying Green's theorem. The equations of ship

motion were linearized by assuming the ship motions are small.

The original formulation of the B-spline Rankine panel method was described in detail. The numerical method used in the present work is the constant Rankine panel method which was degraded from the B-spline Rankine panel method. The numerical damping zone was adopted to satisfy the radiation condition on the truncated free surface. The numerical filter was used to retain the growth of the saw-tooth waves on the free surface. Both the numerical damping zone and the numerical filter were demonstrated to be important for the stability of the simulation.

The program has been validated against extensive numerical simulations. Convergence studies have been carried out to examine the effect of the damping zone size, damping strength, domain size, time step size, filter strength, and the number of panels on the free surface and bottom surface on the solutions. Ideal values for the variables have been found. A stepwise study of the wave-induced hydrodynamic forces and motions has been carried for a truncated cylinder, a hemisphere, the Wigley I hull, a Series 60, Cb=0.7 ship, and the two-body side-by-side moored scenario through forced motion and free motion simulations. The time series of hydrodynamic forces and ship motions were stable. The added mass and damping coefficients, as well as RAOs of wave exciting forces and body motions, were extracted from the corresponding time series and compared with the numerical results from the frequency-domain programs MAPS0 and WAMIT. The results from the present method were demonstrated to be accurate and robust.

The present method can be extended to many topics in marine hydrodynamics.

Oblique sea: An easy extension is the simulation in an oblique sea. The computations in an oblique sea require the whole computational domain because the wave flow is no longer symmetric along the $y = 0$ plane.

Global wave load: The calculation of global wave load can be easily achieved by

calculating the shear force and bending moment at ship sections.

Second-order forces: The second-order forces can be calculated in the future with the second-order force terms derived from the boundary value problem formulation.

Arbitrary bathymetry: The seakeeping analysis can be extended to arbitrary bathymetry by the flexible distribution of panels on the bottom surface.

Forward-speed computations: The Neumann-Kelvin flow or the Double-body flow can be incorporated for the simulations with advance speed.

Body nonlinearity: Different levels of nonlinearity can be incorporated into the present method. For the first step, the body nonlinearity can be added by considering the instantaneous wetted surface of the ship hull.

Free surface nonlinearity: The free surface nonlinearity can be included. The instantaneous incident wave profile can be included through the Weak-Scatterer formulation. The fully nonlinear free surface can be solved by applying the MEL method. In conclusion, the present program is stable and accurate in the simulation of wave-induced ship motions. It is also a foundation with great potential that can be further developed to solve seakeeping problems with high complexity.

Bibliography

Bai, W. and Taylor, R. E. (2006). Higher-order boundary element simulation of fully nonlinear wave radiation by oscillating vertical cylinders. *Applied Ocean Research*, 28(4):247–265.

Bandyk, P. J. (2009). *A body-exact strip theory approach to ship motion computations*. PhD thesis, The University of Michigan.

Beck, R. and Liapis, S. (1987). Transient motions of floating bodies at zero forward speed. *Journal of Ship Research*, 31(3).

Beck, R. F. (1994). Time-domain computations for floating bodies. *Applied Ocean Research*, 16(5):267–282.

Beck, R. F. and King, B. (1989). Time-domain analysis of wave exciting forces on floating bodies at zero forward speed. *Applied Ocean Research*, 11(1):19–25.

Beck, R. F. and Magee, A. R. (1990). Time-domain analysis for predicting ship motions. In *Proceedings of the 2nd International Symposium on the Dynamics of Marine Vehicles and Structures in Waves, Uxbridge, U.K.*

Beck, R. F., Reed, A. M., Sclavounos, P. D., and Hutchison, B. L. (2001). Modern computational methods for ships in a seaway. discussion. author's closure. *Transactions-Society of Naval Architects and Marine Engineers*, 109:1–51.

Bingham, H. B. (1994). *Simulating ship motions in the time domain*. PhD thesis, Massachusetts Institute of Technology.

Cao, Y., Schultz, W. W., and Beck, R. F. (1991). Three-dimensional desingularized boundary integral methods for potential problems. *International Journal for Numerical Methods in Fluids*, 12(8):785–803.

Chang, M.-S. (1977). Computations of three-dimensional ship motions with forward speed. In *Proceedings of the 2nd International Conference on Numerical Ship Hydrodynamics, University of California, Berkeley*, pages 124–135.

Chen, X., Diebold, L., and Doutreleau, Y. (2001). New green-function method to predict wave-induced ship motions and loads. In *Proceedings of the 23th Symposium on Naval Hydrodynamics, Val de Reuil, France*.

Chen, X. and Noblesse, F. (1998). Super green functions. In *Proceedings of the 22th Symposium on Naval Hydrodynamics, Washington, DC*, pages 860–874.

Cong, L., Huang, Z., Ando, S., and Hsiung, C. (1998). Time-domain analysis of ship motions and hydrodynamic pressures on a ship hull in waves. In *2nd International Conference on Hydroelasticity in Marine Technology*, pages 485–495.

Cummins, W. (1962). The impulse response function and ship motions. Technical report, DTIC Document.

Danmeier, D. (1999). *A higher-order panel method for large-amplitude simulation of bodies in waves*. PhD thesis, Massachusetts Institute of Technology.

Dawson, C. (1977). A practical computer method for solving ship-wave problems. In *Proceedings of the 2nd International Conference on Numerical Ship Hydrodynamics, University of California, Berkeley*, pages 30–38.

Faltinsen, O. M. (1977). Numerical solution of transient nonlinear free-surface motion outside or inside moving bodies. In *Proceedings of the 2nd International Conference on Numerical Ship Hydrodynamics, University of California, Berkeley*, pages 257–266.

Feng, A., Chen, Z.-M., and Price, W. (2015). A continuous desingularized source distribution method describing wave–body interactions of a large amplitude oscillatory body. *Journal of Offshore Mechanics and Arctic Engineering*, 137(2):021302.

Finkelstein, A. B. (1957). The initial value problem for transient water waves. *Communications on Pure and Applied Mathematics*, 10(4):511–522.

Finn, P. J. (2003). *Large amplitude nonlinear seakeeping using a desingularized method*. PhD thesis, University of Michigan.

Froude, W. (1861). *On the rolling of ships*. Institution of Naval Architects.

Gadd, G. (1976). *A method of computing the flow and surface wave pattern around full forms*. National Maritime Institute.

Guevel, P. and Bougis, J. (1982). Ship-motions with forward speed in infinite depth. *International Shipbuilding Progress*, 29(332):103–117.

He, G. and Kashiwagi, M. (2014). Time-domain analysis of steady ship-wave problem using higher-order bem. *International Journal of Offshore and Polar Engineering*, 24(01):1–10.

Hess, J. L. and Smith, A. (1967). Calculation of potential flow about arbitrary bodies. *Progress in Aerospace Sciences*, 8:1–138.

Hoff, J. R. (1990). Three-dimensional green function of a vessel with forward speed in waves. Technical report, Norwegian Institute of Technology.

Huang, Y. (1997). *Nonlinear ship motions by a Rankine panel method*. PhD thesis, Massachusetts Institute of Technology.

Hulme, A. (1982). The wave forces acting on a floating hemisphere undergoing forced periodic oscillations. *Journal of Fluid Mechanics*, 121:443–463.

Inglis, R. and Price, W. (1981). A three-dimensional ship motion theory: comparison between theoretical predictions and experimental data of the hydrodynamic coefficients with forward speed. *Trans. RINA*, 124:141–157.

Israeli, M. and Orszag, S. A. (1981). Approximation of radiation boundary conditions. *Journal of Computational Physics*, 41(1):115–135.

Iwashita, H. and Ohkusu, M. (1992). The green function method for ship motions at forward speed. *Ship Technology Research*, 38(2):3–22.

Kara, F., Tang, C. Q., and Vassalos, D. (2007). Time domain three-dimensional fully nonlinear computations of steady body–wave interaction problem. *Ocean Engineering*, 34(5):776–789.

Kim, D. and Kim, M. (1997). Wave-current-body interaction by a time-domain high-order boundary element method. In *Proceedings of the 7th International Offshore and Polar Engineering Conference*, volume 3, pages 107–115.

Kim, K.-H. and Kim, Y. (2011). Numerical study on added resistance of ships by using a time-domain rankine panel method. *Ocean Engineering*, 38(13):1357–1367.

Kim, T. and Kim, Y. (2013). Numerical analysis on floating-body motion responses in arbitrary bathymetry. *Ocean Engineering*, 62:123–139.

Kim, Y. (1999). *Computation of higher-order hydrodynamic forces on ships and offshore structures in waves*. PhD thesis, Massachusetts Institute of Technology.

Kim, Y., Kim, K.-H., Kim, J.-H., Kim, T., Seo, M.-G., and Kim, Y. (2011). Time-domain analysis of nonlinear motion responses and structural loads on ships and offshore structures: development of wish programs. *International Journal of Naval Architecture and Ocean Engineering*, 3(1):37–52.

Kim, Y., Kring, D. C., and Sclavounos, P. D. (1997). Linear and nonlinear interactions of surface waves with bodies by a three-dimensional rankine panel method. *Applied Ocean Research*, 19(5):235–249.

King, B. (1987). Time domain analysis of wave exciting forces on ships and bodies. Technical report, University of Michigan.

King, B., Beck, R., and Magee, A. (1988). Seakeeping calculations with forward speed using time-domain analysis. In *Proceedings of the 17th Symposium on Naval Hydrodynamics, The Hague, Netherlands*, pages 577–596.

Korsmeyer, F. (1991). The time domain diffraction problem. In *Proceedings of the 6th International Workshop on Water Waves and Floating Bodies, Woods Hole, Massachusetts, USA*.

Korsmeyer, F., Lee, C., Newman, J., and Sclavounos, P. (1988). The analysis of wave effects on tension-leg platforms. In *Proceedings of the 7th Internation Conference on Offshore Mechanics and Arctic Engineering, Houston, Texas*.

Korvin-Kroukovsky, B. V. and Jacobs, W. R. (1957). Pitching and heaving motions of a ship in regular waves. Technical report, DTIC Document.

Kring, D. C. (1994). *Time domain ship motions by a three-dimensional Rankine panel method*. PhD thesis, Massachusetts Institute of Technology.

Krylov, A. (1896). A new theory of the pitching motions of a ship on waves and the stresses produced by this motion. *INA Transactions*, 37:326–368.

Lewis, F. M. (1929). The inertia of the water surrounding a vibrating ship. *Trans. SNAME*, 37:1–20.

Liapis, S. J. (1986). *Time-domain analysis of ship motions*. PhD thesis, University of Michigan.

Lin, W. and Yue, D. (1990). Numerical simulations for large amplitude ship motions in the time domain. In *Proceedings of the 18th Symposium on Naval Hydrodynamics, Ann Arbor, Michigan*.

Longuet-Higgins, M. and Cokelet, E. (1976). The deformation of steep surface waves on water. i. a numerical method of computation. *Proceedings of the Royal Society of London. Series A, Mathematical and Physical Sciences*, pages 1–26.

Maruo, H. (1970). An improvement of the slender body theory for oscillating ships with zero forward speed. *Bulletin of the Faculty of Engineering, Yokohama National University*, 19:45–56.

Michell, J. H. (1898). Xi. the wave-resistance of a ship. *The London, Edinburgh, and Dublin Philosophical Magazine and Journal of Science*, 45(272):106–123.

Nakos, D., Kring, D., and Sclavounos, P. (1993). Rankine panel methods for transient free surface flows. In *Proceedings of the 6th International Conference on Numerical Ship Hydrodynamics, Iowa City, Iowa*.

Nakos, D. and Sclavounos, P. (1990a). On steady and unsteady ship wave patterns. *Journal of Fluid Mechanics*, 215:263–288.

Nakos, D. and Sclavounos, P. (1990b). Ship motions by a three-dimensional rankine panel method. In *Proceedings of the 18th Symposium on Naval Hydrodynamics, Ann Arbor, Michigan*.

Nakos, D. E. (1990). *Ship wave patterns and motions by a three dimensional Rankine panel method*. PhD thesis, Massachusetts Institute of Technology.

Newman, J. (1986). Distributions of sources and normal dipoles over a quadrilateral panel. *Journal of Engineering Mathematics*, 20(2):113–126.

Newman, J. (1994). Wave effects on deformable bodies. *Applied Ocean Research*, 16(1):47–59.

Newman, J. and Sclavounos, P. (1988). The computation of wave loads on large offshore structures. In *Proceedings of the 4th International Conference on Behaviour of Offshore Structures*, pages 605–622.

Newman, J. and Tuck, E. (1964). Current progress in the slender body theory for ship motions. In *Proceedings of the 5th Symposium on Naval Hydrodynamics, Bergen, Norway*, pages 129–165.

Newman, J. N. (1960). *A linearized theory for the motion of a thin ship in regular waves*. PhD thesis, Massachusetts Institute of Technology.

Newman, J. N. (1978). Wave radiation from slender bodies. Technical report, DTIC Document.

Ogilvie, T. F. (1964). Recent progress toward the understanding and prediction of ship motions. In *Proceedings of the 5th Symposium on Naval Hydrodynamics, Bergen, Norway*, pages 3–128.

Ogilvie, T. F. and Tuck, E. O. (1969). A rational strip theory of ship motions: part i. Technical report, University of Michigan.

Pawlowski, J. (1992). A nonlinear theory of ship motion in waves. In *Proceedings of the 19th Symposium on Naval Hydrodynamics, Seoul, Korea*.

Peng, H. H. and Qiu, W. (2014). Computation of motion and added wave resistance with the panel-free method. *Journal of Offshore Mechanics and Arctic Engineering*, 136(3):031103.

Peters, A. and Stoker, J. (1957). The motion of a ship, as a floating rigid body, in a seaway. *Communications on Pure and Applied Mathematics*, 10(3):399–490.

Qiu, W., Peng, H., and Hsiung, C. (2001). Validation of time-domain prediction of motion, sea load, and hull pressure of a frigate in regular waves. In *Proceedings of the 23th Symposium on Naval Hydrodynamics, Val de Reuil, France*.

Qiu, W. and Peng, H. H. (2013). Numerical solution of body-exact problem in the time domain. *Journal of Ship Research*, 57(1):13–23.

Raven, H. (1996). *A solution method for the nonlinear ship wave resistance problem*. PhD thesis, Delft University of Technology.

Sclavounos, P. and Nakos, D. (1988). Stability analysis of panel methods for free-surface flows with forward speed. In *Proceedings of the 17th Symposium on Naval Hydrodynamics, The Hague, Netherlands*.

Sclavounos, P., Nakos, D., and Huang, Y. (1994). Seakeeping and wave induced loads on ships with flare by a rankine panel method. In *Proceedings of the 6th International Conference on Numerical Ship Hydrodynamics, Iowa City, Iowa*.

Sclavounos, P. D. (1985). The unified slender-body theory: Ship motion in waves. In *Proceedings of the 15th Symposium on Naval Hydrodynamics, Hamburg, Germany*, pages 177–192.

Scorpio, S. M. (1997). *Fully nonlinear ship-wave computations using a multipole accelerated, desingularized method*. PhD thesis, University of Michigan.

Scullen, D. C. (1998). *Accurate computation of steady nonlinear free-surface flows*. PhD thesis, The University of Adelaide.

Shao, Y.-L. and Faltinsen, O. M. (2012). Linear seakeeping and added resistance analysis by means of body-fixed coordinate system. *Journal of marine science and technology*, 17(4):493–510.

Stoker, J. J. (1957). *Water Waves*. Interscience Publishers, New York.

Subramani, A. K. (2000). *Computations of Highly Nonlinear Free-Surface Flows, with Applications to Arbitrary and Complex Hull Forms*. PhD thesis, University of Michigan.

Taylor, R. E. and Jefferys, E. (1986). Variability of hydrodynamic load predictions for a tension leg platform. *Ocean Engineering*, 13(5):449–490.

Ursell, F. (1962). Slender oscillating ships at zero forward speed. *Journal of Fluid Mechanics*, 14(04):496–516.

Wehausen, J. V. (1967). Initial-value problem for the motion in an undulating sea of a body with fixed equilibrium position. *Journal of Engineering Mathematics*, 1(1):1–17.

Wehausen, J. V. and Laitone, E. V. (1960). *Surface waves*. Springer.

Yan, H. (2010). *Computations of fully nonlinear three-dimensional wave-body interactions*. PhD thesis, Massachusetts Institute of Technology.

Zhang, X., Bandyk, P., and Beck, R. F. (2007). Large amplitude body motion computations in the time-domain. Technical report, DTIC Document.

Zhang, X., Bandyk, P., and Beck, R. F. (2010). Seakeeping computations using double-body basis flows. *Applied Ocean Research*, 32(4):471–482.

Zhang, X. and Beck, R. F. (2008). Three-dimensional large amplitude body motions in waves. *Journal of Offshore Mechanics and Arctic Engineering*, 130(4):041603.